

QUANTITATIVE STUDIES OF TERRESTRIAL PLASMASPHERIC DYNAMICS
ENABLED BY THE IMAGE SPACECRAFT

by

Brian Arthur Larsen

A dissertation submitted in partial fulfillment
of the requirements for the degree

of

Doctor of Philosophy

in

Physics

MONTANA STATE UNIVERSITY
Bozeman, Montana

April 2007

©COPYRIGHT by

Brian Arthur Larsen

2007

All Rights Reserved

APPROVAL

of a dissertation submitted by

Brian Arthur Larsen

This dissertation has been read by each member of the dissertation committee and has been found to be satisfactory regarding content, English usage, format, citations, bibliographic style, and consistency, and is ready for submission to the Division of Graduate Education.

Dr. David M. Klumpar

Dr. Dana W. Longcope

Approved for the Department of Physics

Dr. William Hiscock

Approved for the Division of Graduate Education

Dr. Carl A. Fox

STATEMENT OF PERMISSION TO USE

In presenting this dissertation in partial fulfillment of the requirements for a doctoral degree at Montana State University, I agree that the Library shall make it available to borrowers under rules of the Library. I further agree that copying of this dissertation is allowable only for scholarly purpose, consistent with "fair use" as prescribed in the U.S. Copyright Law. Requests for extensive copying or reproduction of this dissertation should be referred to Bell & Howell Information and Learning, 300 North Zeeb Road, Ann Arbor, Michigan 48106, to whom I have granted "the exclusive right to reproduce and distribute my dissertation in and from microform along with the non-exclusive right to reproduce and distribute my abstract in any format in whole or in part."

Brian Arthur Larsen

April 2007

To Karla,
Thanks for all the support,
everything is better with you

ACKNOWLEDGMENTS

The combination of my hardware experiences in the Space Science and Engineering Laboratory (SSEL) along with plasmaspheric science work have really crafted my education and experience into something truly exciting, with that, it is on to new and exciting things. For this David Klumpar deserves all the credit that can be given, thanks Dave.

Chris Gurgiolo's acting as a second mentor really getting my scientific career moving, tireless answering of software questions, and started me with IMAGE-EUV data has been highly rewarding and much appreciated. Thanks to the IMAGE-EUV team for taking me in and offering the support necessary to get me up and moving, thanks Bill Sandel, Jerry Goldstein, Jim Burch, Dennis Gallagher, and everyone else.

My graduate career was made all the more enjoyable through interactions with the other graduate students, faculty, staff, and everyone. Special thanks to Margaret, Trae, Jonathan, Mike, George, Steve, Sean, TJ, and the whole SSEL crew.

The Montana Space Grant Consortium (MSGC) deserves a hearty thanks as the organization that made my entire graduate career what it has been. From sponsorship of the MEROPE cubesat mission, the BOREALIS balloon program, travel support, and three gracious years of fellowship support MSGC has been a truly fantastic asset to me and Montana State University as a whole, thanks Bill Hiscock.

Karla, what's left to say? A very special thanks to you for helping keep me sane during launch failures, late nights, a personally rough 2006, and all the day to day things.

TABLE OF CONTENTS

1. INTRODUCTION	1
Geospace Environment	1
Magnetosphere	2
McIlwain L Value	3
Plasmaspheric Physics	3
Plasmasphere Description	3
Ring Current	4
Radiation Belts	5
Plasmasphere Overlap	7
Early Plasmasphere Dynamics	7
Inner Magnetosphere Streamline Derivation	9
Plasmasphere: IMAGE Mission	13
IMAGE Description	14
The Extreme Ultraviolet Imager	14
Plasmaspheric Optical Depth	17
Description	17
The IMAGE contribution	18
2. CORRELATION BETWEEN PLASMAPAUSE POSITION AND SOLAR WIND PARAMETERS	21
Introduction	21
Data	24
EUV Data Inversion	24
Inversion Method	27
Plasmapause Determination	31
Analysis	32
Other Tested Parameters	36
Discussion	39
Conclusion	41
3. CROSS-TAIL ELECTRIC FIELD MAGNITUDE DERIVED FROM PLASMA- SPHERIC ALFVÉN LAYER MOTIONS	43
Introduction	43
EUV Derived Convection Field for 8 April 2001	45
Data	45
UT-MLT Stackplot	46
Stackplots	46
Interplanetary Data	50
Convection Field Strength	53
Comparison With <i>in-situ</i> Data	55

<i>in-situ</i> Polar Cap Potential	56
Comparison To Polar Cap Potential Model	60
Results	60
EUV Derived Convection Field for 17 April 2001	62
Data	63
Results	68
Event Comparison	68
Discussion	71
4. PLASMASPHERE DERIVED ELECTRIC FIELDS: CURRENT LIMITATIONS AND FUTURE POSSIBILITIES	73
Introduction	73
EUV Derived Convection Field Limitations and Possibilities	73
EUV Derived Convection Field Requirements	74
60 kV Polar Cap Potential	74
Large Plasmasphere	77
High Quality EUV Data	77
Feature To Track	79
Discussion	81
Future Imaging Concept Mission	81
5. PLASMASPHERIC COROTATION - IONOSPHERIC SIGNATURE	82
Introduction	82
Ionospheric Disturbance Dynamo	83
Sub-corotating Plasmaspheric Event (8Apr2001)	83
Ionospheric DMSP signature	86
Event Conclusions	91
Corotating Plasmaspheric Event (18Jun2001)	92
Ionospheric DMSP signature	94
Event Conclusions	94
Discussion	97
6. SUMMARY OF RESULTS	99
Plasmapause Statistics	99
Convection Electric Field Derived From Global Imaging	100
Observational Verification of the Plasmaspheric Alfvén Layer	100
EUV Derived Convection Electric Field Magnitude	100
Plasmaspheric Signature in the Ionosphere	101
REFERENCES	102
APPENDICES	109
APPENDIX A: MAGNETOSPHERIC COORDINATES	110

LIST OF TABLES

Table	Page
1.1 EUV instrument design parameters. From <i>Sandel et al.</i> (2000).	15
2.1 Equations relating plasmasphere position to the three solar wind parameters studied in the paper. Parameters studied are IMF B_z , IMF clock angle, θ , and polar cap potential drop, ϕ , as defined in equation 2.3. The uncertainties are 1σ confidence found using bootstrap resampling with replacement. Note that NC^{-1} is a Newton per Coulomb.	36
2.2 Tested correlation parameters	38
3.1 Stackplot derived Alfvén layer position for 8Apr2001.	50
3.2 Derived Convection electric field for 8Apr2001. The min and max are calculated from the inside and outside of the L region.	56
4.1 Requirements of a future plasmaspheric EUV imaging mission.	81

LIST OF FIGURES

Figure	Page
1.1 Early schematic view of the magnetosphere. Notice the “X” point reconnection points at the subsolar magnetopause (far left) and deep into the geomagnetic tail (far right). Image from from <i>Dungey</i> (1963).	2
1.2 Magnetosphere cartoon showing the plasmasphere region of the magnetosphere. Image from <i>Rasinkangas et al.</i> (1998).	5
1.3 Energetic neutral atom (ENA) emissions from the Earth’s ring current, as seen with the High Energy Neutral Atom (HENA) on NASA’s IMAGE spacecraft from 9Jun2000 21:18 during the recovery stage of a geomagnetic storm that began on 8Jun2000 in the 16 – 27 keV energy range. The view is toward Earth’s north pole from an altitude of 5 Earth radii. The relative size and position of the Earth are indicated by the white circle. Pairs of representative field lines (extending to 4 and 8 Earth radii respectively) are shown at (clockwise from top) local midnight, dusk, noon, and dawn. Image and caption courtesy the IMAGE-HENA team.	6
1.4 Cartoon showing the locations where various inner magnetospheric plasma waves are possible. Figure and from <i>Summers et al.</i> (1998).	8
1.5 The plasmopause H^+ concentration, based on groups of observations from the OGO-5 satellite in the range 0000-0400 LT at different levels of magnetic activity. Figure from <i>Chappell et al.</i> (1970b).	8
1.6 Equipotential contours for the magnetospheric electric field in the equatorial plane. Upper left: First-order approximation for the convection electric field as uniform. Upper right: The co-rotation electric field. Lower: Sum of convection and co-rotation electric fields. Figure from <i>Nishida</i> (1966).	9
1.7 Streamlines of the solar wind-induced convection on the equatorial plane for open and closed magnetospheric models. Figure from <i>Axford and Hines</i> (1961); <i>Nishida</i> (1966).	10

1.8	(Left) Left-front view of the EUV, with a portion of the main light baffle cut away to show the location of the sensor heads. The high-voltage power supply is mounted on the far side, hidden in this view. (Right) Cutaway drawing of a sensor head. Detector signal and bias cables are not shown here. Figure and caption from <i>Sandel et al. (2000)</i>	16
1.9	IMAGE/EUV data from 18-Jun-2001. In the images the Sun is to the lower right as seen by the day-glow contamination and the shadow to the upper left. Each image is 10 min apart.	17
1.10	Equatorial plots showing EUV electric field tangential to the plasmopause at 5:25 UT and 7:07 UT on 10 July 2000 shown in red and blue respectively. (a) Tangential electric field vectors, scaled as $1 R_E = 0.8 \text{ mV m}^{-1}$. (b) Scaled flow-directions at the plasmopause. Figure and caption from <i>Goldstein et al. (2004c)</i>	19
2.1	Measured EUV image (left) and the noise and background subtracted image (right). Figure from <i>Gurgiolo et al. (2005)</i>	25
2.2	(right) EUV images between 2001-169 14:00 and 2001-169 15:15 (18Apr2001), in each the Sun is to the lower right as demonstrated by the airglow. There is a large plasmaspheric plume in the upper right of each image. (left) Inversions of the EUV images for comparison. In the inversions the Sun is to the right and the units are now He^+/cm^3 and all look effects are removed.	28
2.3	Example inverted EUV image with the semi-automated extracted plasmopause overplotted. The Sun is to the right and the “bulge” at about 1300 MLT is an anomaly in the data (light contamination) and therefore does not have plasmopause points for that region.	32
2.4	Rank order correlation coefficients as a function of solar wind delay (reaction time). The error bars denote 1σ confidence found using bootstrap resampling with replacement. The dashed vertical line denotes the strongest correlation and the dashed lines show a Gaussian fit to the curve used to find the peak.	34
2.5	Contour plot showing the plasmopause reaction to different observed combinations of IMF B_z and the merging proxy, ϕ	37

2.6	Plots of the correlation as a function of delay for IMF magnitude, $ B $ and solar wind proton velocity, V_{sw}	39
3.1	(Top) Inverted EUV image from 8Apr2001 15:40:29 highlighting the $2.5 - 3R_E$ annulus used to create the stackplot, the sun is to the right. (Bottom) UT-MLT stackplot for the annulus from $2.5 - 3R_E$ for each image in the orbit. Time of the image is plotted on the abscissa and MLT along the ordinate with He^+ density shown linear with color. The over plotted diagonal lines are corotation while the horizontal lines show the 10 minute duration of one image in the plot. The color bar ranges in each plot have been set equal, washing out the inverted image Earthward of the desired annulus.	47
3.2	Stackplots from 8Apr2001 for the annuli from $2 - 2.5$, $2.5 - 3$, and $3 - 3.5R_E$. Overlaid on each plot is the shape of the depression feature that will be used to determine the Alfvén layer offset to the left of the feature. Plot format in each is the same as in Figure 3.1.	49
3.3	Alfvén layer position during the event, the red blocks show the position of the Alfvén layer during the time period.	51
3.4	Interplanetary data from ACE for 8Apr2001. (top) IMF x, y, z components (bottom) IMF clock angle, Proton velocity (V_p), and number density (N_p). The first red vertical dashed line at 10:32 UT marks the time of the interplanetary shock at ACE located $233.6R_E$ upstream of the Earth. The second vertical line at 13:15 UT marks the seconds Alfvén layer motion at 13:56 UT from Figure 3.3 propagated back to ACE. Note the ACE data is not time-delayed to Earth, the delay is about 30 minutes at these solar wind speeds.	52
3.5	Dst and Kp indices for the time during and before 8Apr2001. The thin black vertical line on the plot is the sudden commencement. The red dashed lines are the minimum Alfvén layer positions from Figure 3.3.	53
3.6	Standard two-cell polar cap potential overlaid with schematic DMSP passes for two satellites F13 (red) and F15 (blue). (Image courtesy Center for Space Sciences, University of Texas, Dallas)	57

3.7 DMSP F13 polar cap plots showing the southern hemisphere polar cap pass beginning 8Apr2001 7:52. Shown are the measured cross path ion drifts and the derived potential from these measurements given in the GSM coordinate system. (Plot courtesy Center for Space Sciences, University of Texas, Dallas) 58

3.8 Derived convection electric field from the six DMSP-F13 high confidence passes on 8Apr2001. 59

3.9 Derived convection electric field (right ordinate) and polar cap potential (left ordinate) using the *Weimer* (2001) polar cap potential model for 8Apr2001 plotted in solid. The dashed line is the EUV derived convection electric field. 61

3.10 Running plots of the *Weimer* (2001) derived polar cap potential from 15Apr2001 through 19Apr2001. The vertical lines in the plots separate days, the large numbers indicate the day of year for each day. The right hand ordinate is the convection electric field derived by mapping the polar cap potential out to a magnetotail of diameter $40R_E$ 63

3.11 Dst and Kp indices for the 17Apr2001 period. The vertical line at 18Apr2001 00:45 UT corresponds to the occurrence of a sudden commencement. . . . 64

3.12 Interplanetary data from ACE for 17Apr2001-18Apr2001. (top) IMF x, y, z components (bottom) IMF clock angle, Proton velocity (V_p), and number density (N_p). The vertical line at 18Apr2001 00:00 UT corresponds to the interplanetary shock passing the ACE spacecraft. Note the ACE data is not time delayed to Earth, the delay is about 40 minutes at these solar wind speeds. 66

3.13 Time series of EUV images during the Alfvén layer motion centered at 17Apr2001 22:47:29 UT. The sun is almost straight down and each image is 10minutes apart. 67

3.14 (Left) UT-MLT stackplots from 17Apr2001 showing the 2 – 2.5, 2.5 – 3, 3 – 3.5 R_E annuli from top to bottom. (Right) Identical stackplot with the extracted stagnation transition points marked with red crosses. Note in all plots the colorbar is *linear*. 69

3.15 *Weimer* (2001) derived polar cap potential (PCP) for 17Apr2001 with the EUV derived electric field (E_{sw}) calculated from the stagnation points in Figure 3.14. The error bar shows the maximum and minimum values from the $0.5 R_E$ radial range of each annulus. 70

4.1 Running plot of the *Weimer* (2001) derived polar cap potential from 11 April 2001 through 5 May 2001. The vertical lines separate days, the large numbers indicate the day of year for each day. The right hand ordinate is the convection electric field derived by mapping the polar cap potential out to a magnetotail of diameter $40 R_E$. The mapping method from *Lyons and Williams* (1984). 75

4.2 Relationship between L -value of observed Alfvén layer crossings and the required polar cap potential for different values of MLT. In this model the Alfvén layer is symmetric yielding the dual MLT valued curves in the plot. . 76

4.3 Plasmopause location histogram of the plasmopause points used in the statistical study of *Larsen et al.* (2007). 78

4.4 IMAGE-EUV data coverage for 15Apr2001 to 20Apr2001. The grey regions denote regions of high EUV data quality. 79

4.5 (left) UT-MLT stackplot for 10Jul2000 (day 192) 02:05-10:00UT for the annulus $2 - 2.5 R_E$. (right) UT-MLT stackplot for 19Jun2001 (day 170) 01:14-12:00UT for the annulus $2.5 - 3 R_E$ 80

5.1 IMAGE-EUV time series from 8Apr2001 10:03UT to 8Apr2001 11:29UT showing the rotation of a large plasmaspheric shoulder. (right side of each image) Each EUV image is 10 minutes apart. 84

5.2 Dst and Kp indices for 7Apr2001 12:00UT (day 97) to 8Apr2001 24:00UT (day 98). The vertical lines at 8Apr2001 06:59UT and 8Apr2001 17:40UT denote the time covered in Figure 5.5. 85

5.3 Selection of IMAGE-EUV images from 6-8Apr2001. The overplotted red beginning in the first image displays the position of the notch if it were corotating. In each subsequent image the yellow arrow marks the center of the notch. Figure from *Burch et al.* (2004). 85

5.4	Position of the plasmaspheric notch in MLT as a function of UT during its observation 6Apr2001 03:05UT to 8Apr2001 12:03UT shown by the black line. The green diamonds represent the notch location as predicted by the DMSP measured eastward drift. The solid red line shows the position as predicted by perfect corotation. Figure adapted from <i>Burch et al. (2004)</i>	87
5.5	UT-MLT stackplots for 8Apr2001, shown are the 2 – 2.5, 2.5 – 3, 3 – 3.5, and 3.5 – 4 R_E annuli. MLT is seen to run from 00 to 48 as the stackplot is reproduced one image ahead to avoid having to wrap around the plot while following features.	88
5.6	DMSP measured eastward drift as a function of magnetic latitude for 8Apr2001 in four MLT sectors centered at 12, 00, 06, 18 MLT.	90
5.7	DMSP measured average Eastward drift for 8Apr2001 as a function of UT for different magnetic latitude ranges, 30° – 35°, 35° – 40°, 40° – 45°, 45° – 50°. The dark line overplotted is a moving average meant to bring out trends in the data.	91
5.8	Selection of IMAGE-EUV images from 18Jun2001 demonstrating the wrapping of a large plasmaspheric plume.	92
5.9	Dst and Kp indices for 17Jun2001 12:00UT (day 168) to 19Jun2001 06:00UT (day 170). The vertical lines at 18Jun2001 11:57UT and 19Jun2001 02:40UT denote the time covered in Figure 5.10.	93
5.10	UT-MLT stackplots for 18Jun2001, shown are the 2 – 2.5, 2.5 – 3, 3 – 3.5, and 3.5 – 4 R_E annuli.	95
5.11	DMSP measured eastward drift as a function of magnetic latitude for 18Jun2001 in four MLT sectors centered at 12, 00, 06, 18 MLT.	96
5.12	DMSP measured average Eastward drift for 18Jun2001 as a function of UT for different magnetic latitude ranges, 30° – 35°, 35° – 40°, 40° – 45°, 45° – 50°.	96

ABSTRACT

Terrestrial plasmaspheric dynamics have been observed using single satellite passes and long term statistical studies for many years all with *in-situ* measurements. The EUV instrument aboard the IMAGE spacecraft provided global plasmaspheric data by imaging He-II at 30.4nm. The global imaging revealed significant dynamics modifying current theory and observing many new features. Global imaging removes any space/time ambiguity and provides a regular high-quality data set ideal for correlative studies and region comparisons. This work presents several studies enabled by this global imaging: an empirical model of plasmopause position as a function of solar wind parameters, a derivation of the global magnetospheric convection electric field based on plasmaspheric feature tracking, and a study of plasmaspheric rotation and its associated ionospheric ion drift signature. Using plasmopause position data extracted from inverted EUV images, the plasmopause position is found to be strongly correlated with the interplanetary magnetic field (IMF) z -component and a magnetospheric merging proxy. Delay in the plasmopause response to the arrival of solar wind conditions at Earth is found to be 180 minutes for the IMF z -component while the delay from the arrival of the merging proxy is found to be 240 minutes. This result allows an upstream solar wind monitor such as ACE to enable a simple prediction of the plasmopause location three hours in advance. Using inverted IMAGE-EUV data it is demonstrated that Alfvén layer boundary positions are sufficient to derive the magnetospheric convection electric field strength. This result provides a global imaging method to derive a parameter responsible for significant inner magnetospheric dynamics. No ionospheric drift differences are found between corotating and sub-corotating plasmaspheric conditions; this is believed to be caused by an under-sampling in the drift measurement locations, highlighting the need for further exploration of magnetosphere-ionosphere (M-I) coupling.

CHAPTER 1

INTRODUCTION

This dissertation explores new quantitative studies of the inner magnetosphere opened by recent advances in global magnetosphere imaging. The imaging of the plasmasphere by resonantly scattered He^+ 30.4 nm extreme ultraviolet light reveals significantly more structure and more complex dynamics than previously suspected. Global imaging offers significant improvements in the approaches available to a large number of studies. Correlative studies using global and *in-situ* measurements greatly increase conjunctions and therefore both statistic and event availability. Global imaging also opens up studies of the morphology and motion of large scale features. Global imaging also alleviates the problems of space/time aliasing of data, there is no ambiguity in the data about temporal and spatial changes.

The focus of this dissertation will be on the configuration and dynamics of the inner magnetospheric system as a whole; in particular the role of the plasmasphere. The Earth's magnetosphere has a standard and unchanging overall configuration that will be defined and discussed, together with the changes that occur within that system. This chapter is meant to give the scientific reader an introduction to the region of space studied and its dynamics. A detailed description of the the entire system is beyond the scope of this work. For a more exhaustive overview of the geospace system I suggest the introductory text *Kivelson and Russell* (1995). For a more exhaustive look at the plasma physics involved, *Parks* (2004) is excellent. For a reference about the electromagnetism and single charged particle motion involved, *Northrup* (1963) is the seminal work. For a reference about electromagnetism, *Jackson* (1998) is exhaustive.

Geospace Environment

Magnetosphere

The magnetosphere is the region of space dominated by the Earth's magnetic field. The magnetic field forms a cavity in the heliosphere separating and to a large extent shielding the Earth from the interplanetary plasma. The interplanetary plasma has its source at the sun. Expansion of the solar corona gives rise to the solar wind which at Earth is supersonic. The interaction of the solar wind and the Earth's magnetosphere set up a collisionless bow shock which diverts most of the solar wind around and down the flanks of the magnetosphere. Figure 1.1 is an early, yet correct, schematic view of the magnetosphere from *Dungey* (1963). The solar wind carries the solar magnetic field with it. This field is known as the Interplanetary Magnetic Field (IMF). The IMF orientation and strength have a significant impact on the dynamics of the magnetosphere.

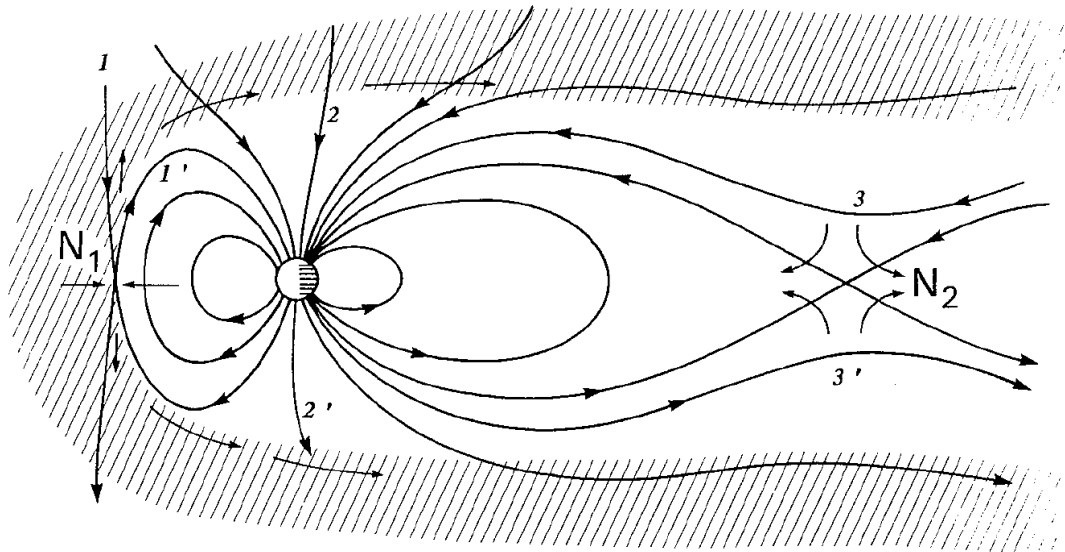


Figure 1.1: Early schematic view of the magnetosphere. Notice the “X” point reconnection points at the subsolar magnetopause (far left) and deep into the geomagnetic tail (far right). Image from from *Dungey* (1963).

The magnetosphere is typically broken into two distinct regions, the inner and outer (or tail) magnetosphere. The inner magnetosphere is characterized as the region where the magnetic field can be considered dipolar, and the outer magnetosphere is characterized by magnetic field lines that are significantly stretched through interactions with the solar wind. A simple operational definition used throughout this work is that field lines that lie equatorward of the auroral zone are considered inner magnetosphere, auroral zone field lines map to both the near and far tail, and polar cap field lines connect with the IMF and are swept deep into the tail before reconnecting.

McIlwain L Value

The McIlwain L value, often referred to simply as L or L -shell, is a way to enumerate flux tubes in the magnetosphere. For a dipole field, the L value is the number of Earth radii where a flux tube crosses the equatorial plane. An L -shell is the set of all field lines that cross the equatorial plane at that distance for every local time. This is a slight misuse of the original parameter, but 30+ years have made this definition commonplace (*McIlwain*, 1961; *Heynderickx et al.*, 1996). Appendix A contains the mathematical definition and relations pertaining to the McIlwain L value.

Plasmaspheric Physics

Plasmasphere Description

The plasmasphere is a region within the magnetosphere characterized by cold (~ 1 eV), dense ($\sim 10^3$ cm $^{-3}$) non-collisional co-rotating plasma. It extends from its source, the ionosphere, out to several Earth radii (R_E). This region was discovered independently by *Gringauz* (1963) using satellite data, and by *Carpenter* (1966) using ground based whistler

observations. Carpenter observed a sharp density gradient at $3 - 5 R_E$ which he coined the “plasmopause.”

The plasmasphere is the innermost magnetospheric plasma population (Figure 1.2). Typically the plasmasphere extends to $2 R_E$ or less during active times and upward of $6 R_E$ during geomagnetically quiet times. The plasmasphere is an outward extension of the ionosphere. There is no clear boundary between the two regions however plasmaspheric altitudes tend to be measured in R_E while ionospheric altitudes are measured in km making the difference largely one of scale and position. Empty or partially filled flux tubes are slowly filled ($\tau \sim \text{days}$) from the ionosphere by pressure driven diffusion along the local field lines. The process is both complex and ill understood in its entirety (*Song et al.*, 1988; *Horwitz and Singh*, 1992; *Rasmussen et al.*, 1993). In contrast to the slow refilling rate the plasmasphere can be depleted in a matter of minutes, making this a highly dynamic plasma population (*Carpenter and Anderson*, 1992; *Goldstein et al.*, 2002b). Particle populations that overlap the plasmasphere are affected by its dynamic nature making the plasmasphere an important region to study, in order to understand the dynamics of other more energetic populations. Two of the more important overlapping populations are the ring current and the radiation belts, described below.

Ring Current The ring current is a population of particles between $1 - 200 \text{ keV}$. These constitute a westward current around the Earth in the equatorial range ~ 2 to $7 R_E$. Electrons and protons convected earthward from the magnetotail during magnetically active periods drift in different directions around the Earth in response to the magnetic gradient curvature force. Much of the energization of the particles comes from impulsive magnetic reconnection in the deep magnetotail. Figure 1.3 shows a representative image of the ring current from the IMAGE-HENA instrument (*Mitchell et al.*, 2000). The Energetic Neutral Atoms (ENA) used to image the ring current are created through charge exchange between

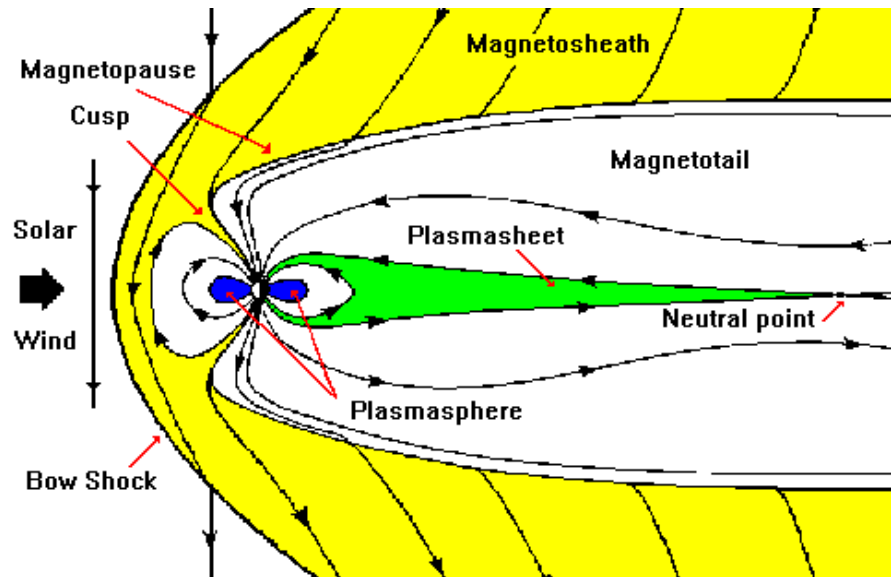


Figure 1.2: Magnetosphere cartoon showing the plasmasphere region of the magnetosphere. Image from *Rasinkangas et al. (1998)*.

the trapped energetic ions and the neutral hydrogen geocorona yielding an energetic proton and an ENA. The ENA, being neutral, exit the ring current on ballistic trajectories and are used to image ring current ion densities. This requires a non-trivial inversion of the raw ENA image. The ring current plays an important role in the dynamics and energetics of magnetospheric substorms making it an important process to study.

Radiation Belts The radiation belts, or the Van Allen radiation belts after their discoverer Dr. James Van Allen (*van Allen et al., 1959*), are highly energized, trapped particles, organized into two distinct regions separated by a slot. The inner belt has a typical equatorial extent of $0.1 - 1.5R_E$ with the most energetic component being a large population of energetic protons ($\sim 1 - 100\text{MeV}$). It is often referred to as the proton belt. The outer belt ($2 - 10R_E$) has energetic electrons ($0.1 - 10\text{MeV}$) as its primary energetic component. The radiation belts are an important region to study for two reasons: to understand the basic particle acceleration processes involved and as a major source of problems in

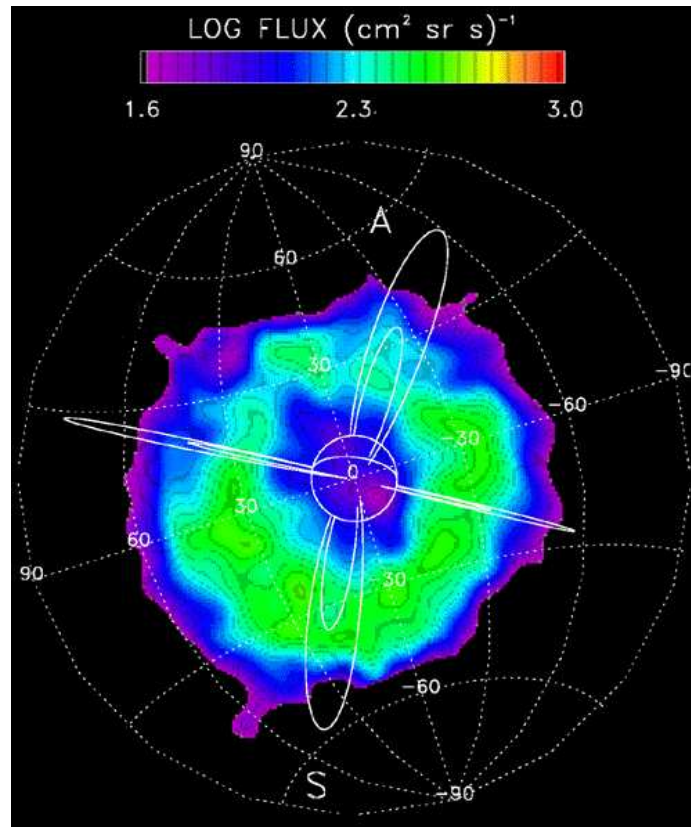


Figure 1.3: Energetic neutral atom (ENA) emissions from the Earth's ring current, as seen with the High Energy Neutral Atom (HENA) on NASA's IMAGE spacecraft from 9Jun2000 21:18 during the recovery stage of a geomagnetic storm that began on 8Jun2000 in the 16 – 27 keV energy range. The view is toward Earth's north pole from an altitude of 5 Earth radii. The relative size and position of the Earth are indicated by the white circle. Pairs of representative field lines (extending to 4 and 8 Earth radii respectively) are shown at (clockwise from top) local midnight, dusk, noon, and dawn. Image and caption courtesy the IMAGE-HENA team.

spacefaring applications of all kinds. More than one spacecraft has been lost due to high doses of radiation from radiation belt flythroughs.

Plasmasphere Overlap Study of the plasmasphere is easily split into two categories, one being the study of the plasmasphere itself and the other its influence on both the ring current and radiation belts that overlap it. The latter forms an important aspect in magnetosphere-ionosphere (M-I) coupling. The phrase often used to describe plasmaspheric studies is “the coldest particles determine the dynamics of the hottest particles.” Figure 1.4 shows the relationship between possible wave modes and the plasmasphere which varies along a particle's drift trajectory. The different plasma waves and their effect on the radiation belt and ring current particles is well beyond the scope of this work, except to say that each of the waves shown in Figure 1.4 scatter energetic particles. They have important implications for the creation of the slot region between the electron and proton belts as well as overall acceleration and loss rates within these regions. They also provide a mechanism to transfer energy from the ring current to the topside ionosphere. It can be said that the study of the plasmasphere is the study of the whole inner magnetosphere.

Early Plasmasphere Dynamics

From *in-situ* and ground based observations during the late 1960's and 1970's the plasmasphere was thought to be roughly circular (in the equatorial plane) with a “duskside bulge.” The plasmasphere was known to increase in size with low magnetospheric activity, and decrease in size with increased activity. Figure 1.5 shows an early plot of plasmasphere profiles for different levels of geomagnetic activity, demonstrating its dependence on the Kp index, which is a measure of global magnetospheric convection. As global convection increases (increasing values of Kp) the plasmapause is closer to Earth than during quiet (low Kp) times.

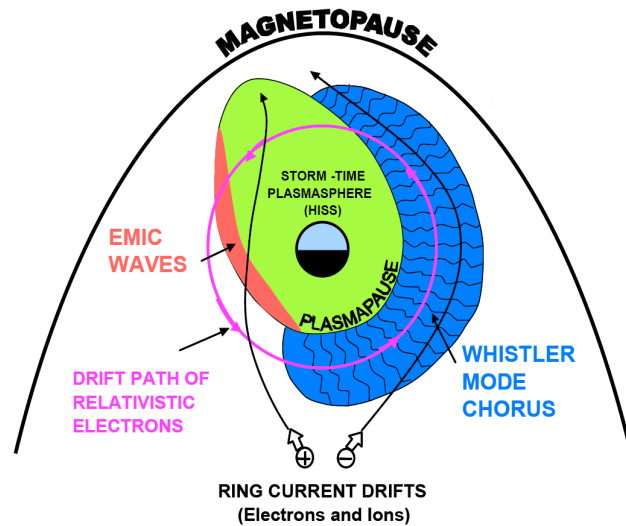


Figure 1.4: Cartoon showing the locations where various inner magnetospheric plasma waves are possible. Figure and from *Summers et al.* (1998).

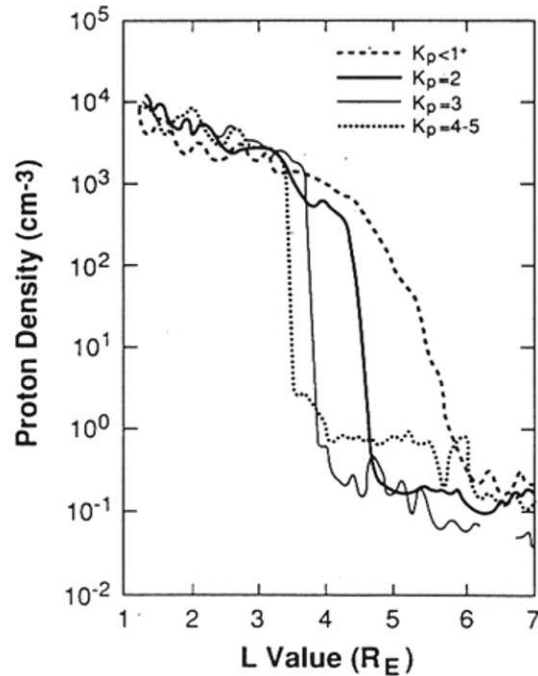


Figure 1.5: The plasmapause H^+ concentration, based on groups of observations from the OGO-5 satellite in the range 0000-0400 LT at different levels of magnetic activity. Figure from *Chappell et al.* (1970b).

The plasmasphere is located in the region of overlap between the radially inward corotation and the dawn-dusk convection electric fields. The electric fields are described in detail later in this chapter. The plasmaspheric plasma reacts to the local $\mathbf{E} \times \mathbf{B}$ force set up by the superposition of the two fields. The overlap of these fields creates two types of drift paths; open and closed. On the closed drift paths the plasma is trapped, and in the open drift path the plasma convects sunward and is lost at the magnetopause. Figure 1.6 shows the simplest model of the inner magnetosphere $\mathbf{E} \times \mathbf{B}$ streamlines, while Figure 1.7 shows a more complicated and realistic model obtained by adding in effects such as inner magnetospheric shielding.

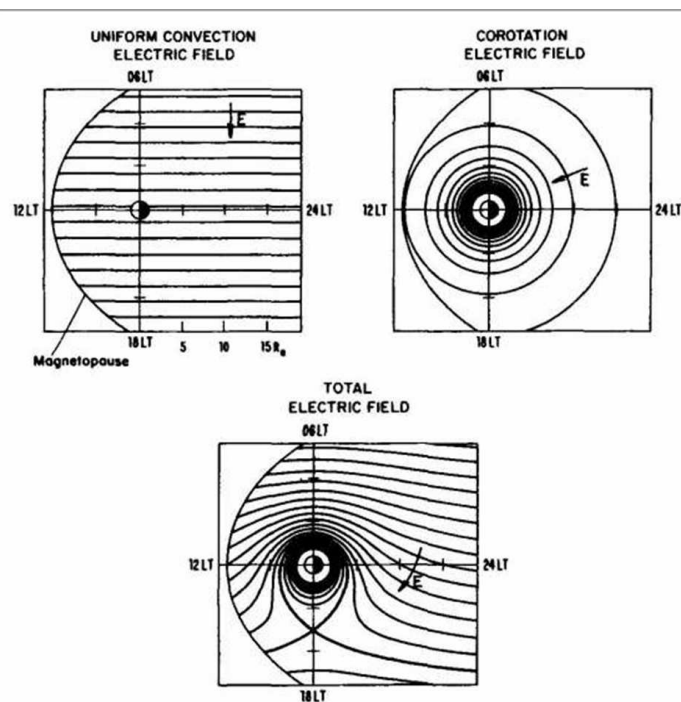


Figure 1.6: Equipotential contours for the magnetospheric electric field in the equatorial plane. Upper left: First-order approximation for the convection electric field as uniform. Upper right: The co-rotation electric field. Lower: Sum of convection and co-rotation electric fields. Figure from *Nishida* (1966).

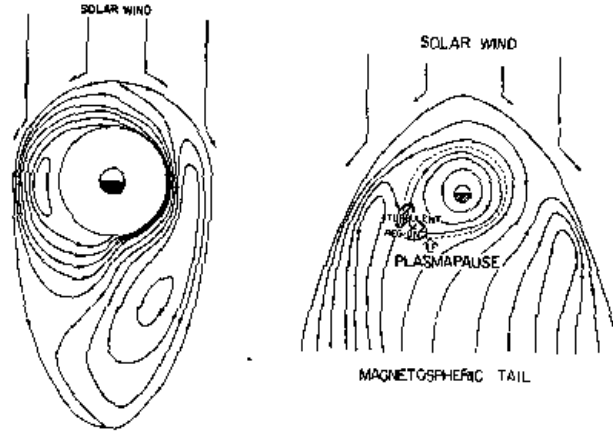


Figure 1.7: Streamlines of the solar wind-induced convection on the equatorial plane for open and closed magnetospheric models. Figure from *Axford and Hines (1961)*; *Nishida (1966)*.

Inner Magnetosphere Streamline Derivation In order to illustrate the overall behavior of the cold plasma inner magnetosphere, it is instructive to derive the streamlines in Figure 1.6. This derivation closely follows that of *Parks (2004)* but is limited to the equatorial plane (also see *Lyons and Williams (1984)*). The electric field in the stationary frame of the corotating plasma in the presence of the Earth's dipole field is

$$\mathbf{E}_c = -(\boldsymbol{\omega} \times \mathbf{r}) \times \mathbf{B} \quad (1.1)$$

where $\boldsymbol{\omega}$ is the Earth's angular velocity. The magnetic field of the Earth on the equatorial plane is given in Appendix A Equation A.2 as

$$\mathbf{B} = \hat{\mathbf{z}} \frac{B_0}{(r/r_0)^3} = \hat{\mathbf{z}} \frac{B_0}{L^3} \quad (1.2)$$

where B_0 is the surface magnetic field and $L = r/r_0$. Aligning the dipole axis with the spin axis sets $\boldsymbol{\omega} = \omega \hat{\mathbf{z}}$ and noting that $\mathbf{r} = r \hat{\mathbf{r}}$ allows for the calculation of

$$\boldsymbol{\omega} \times \mathbf{r} = \omega r (\hat{\mathbf{z}} \times \hat{\mathbf{r}}) \quad (1.3)$$

Substituting equations 1.2 and 1.3 into 1.1 yields the corotation electric field

$$\begin{aligned} \mathbf{E}_c &= -\omega r \frac{B_0}{L^3} (\hat{\mathbf{z}} \times \hat{\mathbf{r}}) \times \hat{\mathbf{z}} \\ &= -\hat{\mathbf{r}} \omega r \frac{B_0}{L^3} \end{aligned} \quad (1.4)$$

which falls off as $1/r^2$ and points radially inward. Assuming that \mathbf{E}_c is a potential field ($\nabla \times \mathbf{B} = 0$, $\mathbf{E}_c = -\nabla\psi$) the scalar potential can be written as

$$\psi_c = -\frac{\omega B_0 R_E^2}{L} \quad (1.5)$$

where $r = R_E L$. Particles of zero thermal energy follow equipotential lines as their streamlines and produce the upper right frame in Figure 1.6.

The other field in the derivation is the cross tail or convection electric field which is driven by the solar wind motion past the magnetosphere. To estimate this field we assume that the solar wind drags flux tubes from noon to dusk across the the polar caps, which produces a $\mathbf{v} \times \mathbf{B}$ electric field. Assuming force balance ($\sum \mathbf{F} = 0$), which then implies frozen in flux and using a dipole magnetic field the convection electric field can be stated as

$$\mathbf{E}_{conv} = -\eta \mathbf{v}_{sw} \times \frac{\mathbf{M}}{R_E^3} \quad (1.6)$$

where \mathbf{v}_{sw} is the solar wind velocity, \mathbf{M} is the planetary dipole moment, and η is a dimensionless coupling efficiency of the solar wind into the magnetosphere (*Selesnick and Richardson, 1986*). The convection field in equation 1.6 assuming a radial outward solar wind and a southward pointing dipole moment gives rise to a dawn-dusk convection

field which to first order is constant in the whole inner magnetosphere at about $E_{sw} = 2.5 \times 10^{-4} \text{ V m}^{-1}$. This constant field

$$\mathbf{E}_{sw} = -E_{sw}\hat{\mathbf{y}} \quad (1.7)$$

then can be written as a scalar potential as

$$\begin{aligned} \Psi_{sw} &= E_{sw}y \\ &= E_{sw}LR_E \sin \phi \end{aligned} \quad (1.8)$$

The 0eV streamlines from equation 1.8 are shown in the upper left frame of figure 1.6.

The final frame in figure 1.6 is derived by the superposition of these two potentials

$$\begin{aligned} \Psi &= \Psi_c + \Psi_{sw} \\ &= \frac{-\omega B_0 R_E^2}{L} + E_{sw}LR_E \sin \phi \end{aligned} \quad (1.9)$$

The equation of the contours of constant ψ are found by solving equation 1.9 for L as

$$L = \frac{-\psi \pm \sqrt{\psi^2 + 4B_0 R_E^3 E_{sw} \omega \sin \phi}}{2R_E E_{sw} \sin \phi} \quad (1.10)$$

where E_{sw} is a free parameter of the system. As the strength of the convection electric field increases (equation 1.7) closed drift paths will change to open drift paths, losing plasma in those flux tubes to the magnetopause (see Figure 1.6). The plasma reacts at drift speeds which are much slower than the Alfvén speed at which the drift paths change, requiring a distinction be made between the open/closed boundary and the plasmopause. The open/closed boundary is a function only of the fields present while the plasmopause is a

density feature, an important distinction that is often forgotten. It should also be noted that this simple derivation does not allow for the direction of the convection field to vary, or for there to be localized regions of different field strengths and directions. Both are known to occur, and affect the plasmasphere, especially during impulsive events.

Magnetospheric currents play a crucial role in the evolution of the plasmasphere. Examples are the phenomena of shielding, overshielding, and undershielding of the inner magnetosphere (see *Schild et al.*, 1969; *Vasyliunas*, 1970; *Wolf*, 1974; *Peymirat et al.*, 2000; *Goldstein et al.*, 2002a, 2003b). To illustrate these phenomena we will follow a standard activity cycle in the inner magnetosphere. Assume that a steady northward interplanetary magnetic field (IMF) has a southward turning and remains southward for a long stretch of time. This increases convection in the magnetosphere (seen as an increase in the convection field from equation 1.8) causing the plasmasphere to shrink. Adding magnetospheric currents to this simple model sets limits on the plasmasphere response. In response to the increased convection the plasmasheet forms a partial ring current which, closing in the finite conductivity ionosphere, sets up electric fields that act to shield the inner magnetosphere from the convection field. This shielding is found to take about an hour to become complete (*Kelley et al.*, 1979). Since the shielding takes time to become effective, the period before the shielding is complete is described as undershielding. If the IMF turns back northward the shielding is now too large causing plasma to flow anti-sunward until the system can reorganize itself to the correct amount of shielding. The above scenario is discussed with data and simulation results by *Goldstein et al.* (2002a).

Plasmasphere: IMAGE Mission

In the late 1990s the detailed understanding of the plasmaspheric response to external drivers and the plasmasphere interaction with the rest of the inner magnetosphere became

a timely and interesting topic. It became apparent that to make the next step in our understanding of the dynamics of the inner magnetosphere would require global imaging capability with sufficient time resolution to observe the changes and interactions taking place. This was sufficient to warrant NASA's support of the Imager for Magnetopause-to-Aurora Global Exploration (IMAGE) mission. IMAGE was to perform global imaging of the plasmasphere, ring current, and aurora.

IMAGE Description

The IMAGE satellite (*Burch, 2000*) was launched in March 2000 into an polar elliptical orbit with axes $0.15 \times 7.2 R_E$ with a 14.2h orbital period. The spacecraft has a 2 min spin period that sets the temporal resolution of most measurements. The highly elliptical orbit provides long stretches of time with favorable observing geometry, with lines of sight nearly perpendicular to the geomagnetic equatorial plane. The orbit precesses in time so that apogee moves from over the North pole to the equatorial plane to over the South pole in about eight years. This dissertation utilizes data from the IMAGE mission which provides the first opportunity to use global data in the study of the inner magnetosphere.

The Extreme Ultraviolet Imager The Extreme Ultraviolet Imager (EUV) instrument aboard IMAGE (*Sandel et al., 2000*) measures the brightness of the He^+ 30.4 nm resonantly scattered emission from the plasmasphere. It has a spatial resolution of 0.6 deg (about $0.1 R_E$) at apogee and a time resolution of ~ 10 min (5 satellite revolutions). The measured brightness is directly proportional to the column abundance of the optically thin He^+ along the lines of sight corresponding to each pixel. As the He^+ is optically thin (see page 17) the photons that reach the detector come from the entire column of plasma within the field of view of each detector pixel. He^+ accounts for approximately 15% of the electron density the rest is made up by H^+ and trace amounts of O^+ (*Carpenter and Lemaire, 1997*). It is

still debated about whether the He^+ can serve as a correct proxy for the e^- density (*Jaggi and Wolk, 1973; Waite et al., 1984; Newberry et al., 1989*).

EUV is a scanning instrument with three sensor heads, each with a 30 deg field of view that overlaps 3 deg with the neighboring head. Each detector is a spherically curved microchannel plate (MCP) with stack and wedge and strip readout. Each MCP is scanned to obtain three measurements that are 52×600 with a two pixel overlap (*Sandel et al., 2000*).

Shown in table 1.1 are the EUV design parameters. EUV is a wideband instrument

Table 1.1: EUV instrument design parameters. From *Sandel et al. (2000)*.

Property	Value
Mass	15.5 kg
Power	9.0 W
Size	$49.7(h) \times 23.3(w) \times 49.5(d)$ cm
Field of view	$84^\circ \times 360^\circ$
Optical design	Prime focus, $f/0.8$ Spherical mirror and focal surface
Angular resolution	0.6°
Spatial resolution	630 km
Time resolution	10 min
Sensitivity	$1.9 \text{ count s}^{-1} \text{ R}^{-1}$
Aperture area	21.8 cm^{-2}
Aperture diameter (outer)	8.2 cm
Aperture diameter (inner)	6.0 cm
Mirror diameter	12.3 cm
Mirror radius of curvature	13.5 cm
Detector active diameter	4.0 cm
Radius of curvature of focal surface	7.0 cm

designed in such a way to allow high transmission of the He^+ 30.4 nm line while having low transmission of the other lines, such as He-I 58.4 nm and O^+ 53.9 nm. The instrument obtains a long wavelength cutoff using an Al filter and a multilayer coated mirror to reflect 30.4 nm and not reflect 58.4 nm (*Sandel et al., 2000*). This design is optimized for plasma-spheric imaging in that it has high peak transmission and low transmission for the specific

lines known to exist in the region, there is no continuum radiation in this wavelength region unless the instrument views the Sun. Figure 1.8 shows a cutaway view of the instrument and a sensor head.

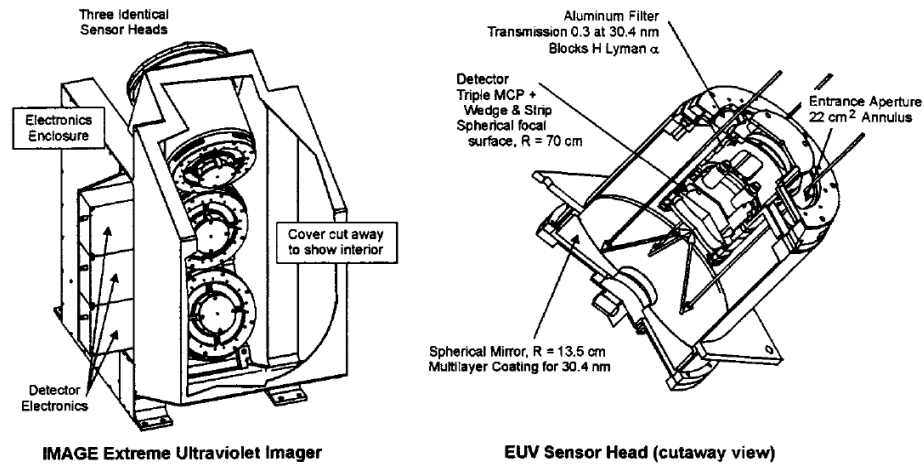


Figure 1.8: (Left) Left-front view of the EUV, with a portion of the main light baffle cut away to show the location of the sensor heads. The high-voltage power supply is mounted on the far side, hidden in this view. (Right) Cutaway drawing of a sensor head. Detector signal and bias cables are not shown here. Figure and caption from *Sandel et al.* (2000).

This instrument allowed the entire plasmasphere to be imaged at once for the first time. This revealed more features and dynamics than were imagined from *in-situ* data, including plasmopause features such as undulations, shoulders, sub-corotation, troughs, and bite-outs (*Burch et al.*, 2001). Figure 1.9 shows a representative time series of images taken on 18Jun2001. Each image is a 360° by 84° (phase by elevation) scan with only the portion containing the plasmasphere being plotted. Each plot spans 10 minutes. Plotted is the line of sight brightness for each pixel on a *log* color scale. Features that show up in every image are the airglow on the sunward side of each image (lower-right) and the faint shadow opposite the sun in each image (upper-left). The airglow is formed by the contamination from O⁺ and neutral He which is intense enough on the dayside to overcome the instrument rejection of these wavelengths. The series shows the formation of a plasmaspheric plume in

the upper-right of each image. As time progresses the plume narrows in magnetic local time (MLT) and begins to wrap around the plasmasphere due to decreased convection. These plumes were known before IMAGE but the exact progression and conditions of formation were unknown.

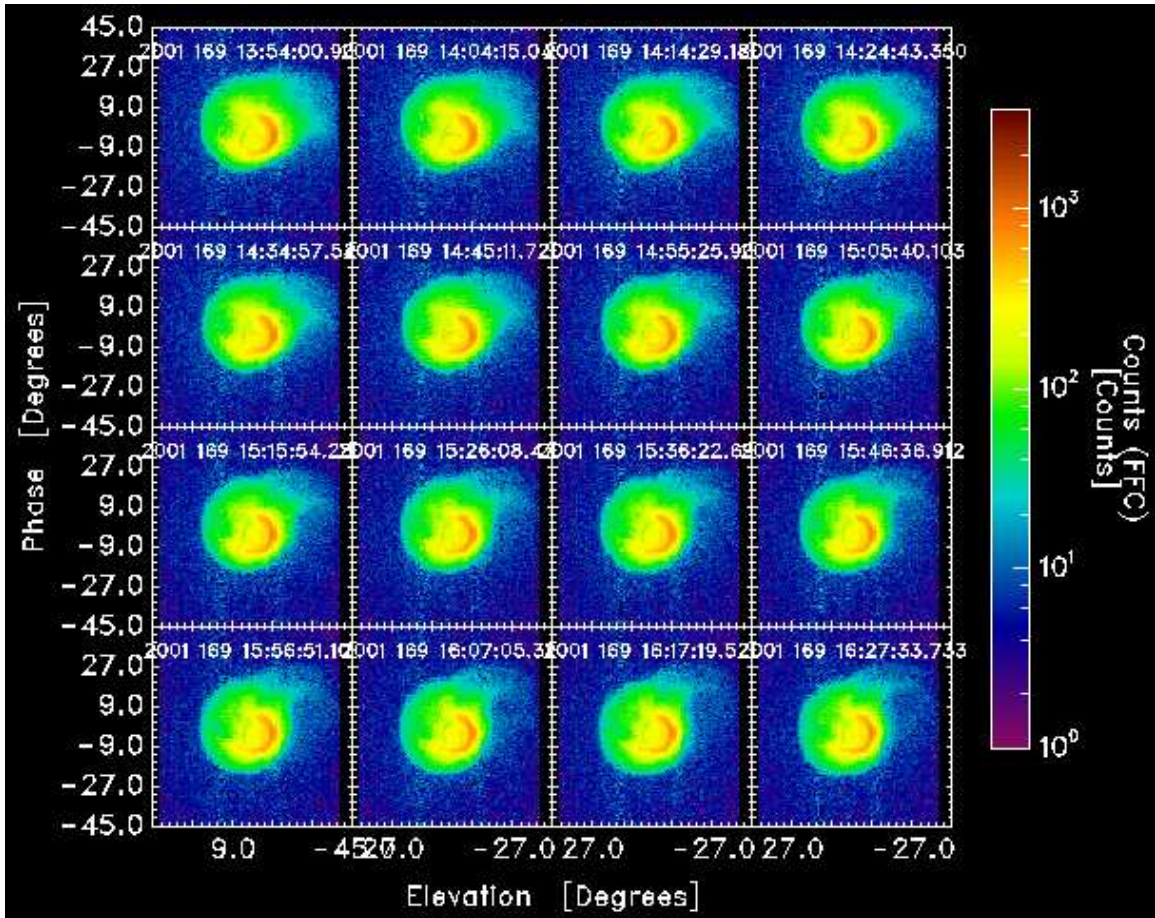


Figure 1.9: IMAGE/EUV data from 18-Jun-2001. In the images the Sun is to the lower right as seen by the day-glow contamination and the shadow to the upper left. Each image is 10 min apart.

Plasmaspheric Optical Depth

Description Optical depth of a medium, τ , is a measure of the transparency of that medium. It is defined as the fraction of radiation that is scattered between a point and the observer, which can be expressed mathematically as $\tau = N\sigma$, where N is the column density and σ is the scattering cross section. In a stellar system the photosphere is defined as the surface where the optical depth, τ , is one, implying that the transmission, $\mathcal{T} = e^{-\tau}$, is 36.8%. Imaging a system with a non-zero optical depth complicates analysis as features can be hidden behind regions of high optical depth just as one cannot see the blue sky or stars through the high optical depth clouds in the sky.

To verify that there is no effect of optical depth in the IMAGE EUV images, we derive the maximum optical depth for a plasmaspheric line of sight. This derivation is not meant to be exhaustive, but instead sets bounds on the optical depth, showing it is essentially zero for any plasmaspheric line of sight.

Beginning with a $2R_E$ path length through the plasmasphere at a He^+ density of 1000 cm^{-3} , which is a high estimate for He^+ , yields a column density of $N = 1.28 \times 10^{12}\text{ cm}^{-2}$. Assuming that the scattering cross section of He^+ is the Van der Waals radius for helium ($\sim 140\text{ pm}$), also a high estimate, the optical depth is

$$\tau = N\sigma = (1.3 \times 10^{12}\text{ cm}^{-2}) \cdot \pi(140\text{ pm})^2 = 8.0 \times 10^{-4} \quad (1.11)$$

and $\tau \ll 1$ implying that the plasmasphere is optically thin and optical depth considerations can be safely neglected. For a more detailed calculation that can be easily expanded to include optical depth see *Garrido et al. (1992)*.

The IMAGE contribution

The ability to globally image the plasmasphere is a major impact of the IMAGE mis-

sion. This allows correlative studies to be made that are impractical using multiple *in-situ* measurements and facilitates the verification of previous statistical views of the plasmasphere. This has led to major break throughs in our understanding of the plasmasphere including: how the plasmasphere as a whole responds to changes in the IMF, cavities in the plasmapause as a source of Auroral kilometric radiation¹ (AKR), the role of the plasmasphere in M-I coupling and others. Before the IMAGE mission, knowledge of the global nature of the plasmasphere was statistical, constructed from multiple ground based and *in-situ* measurements. This washes out both temporal features as well as any motion.

One result which illustrates the potential of global imaging is shown in Figure 1.10, where *Goldstein et al.* (2004c) have derived the large scale azimuthal electric fields by using motions of the plasmapause as deduced from the IMAGE EUV data.

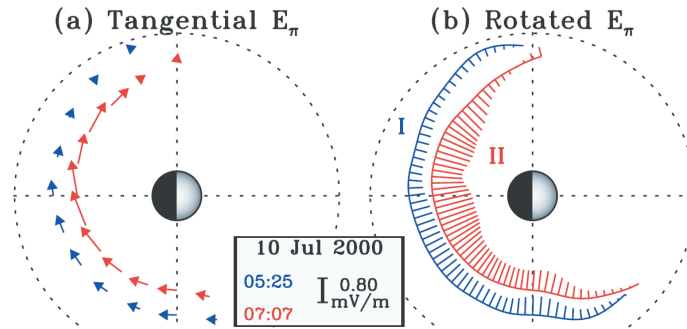


Figure 1.10: Equatorial plots showing EUV electric field tangential to the plasmapause at 5:25 UT and 7:07 UT on 10 July 2000 shown in red and blue respectively. (a) Tangential electric field vectors, scaled as $1 R_E = 0.8 \text{ mV m}^{-1}$. (b) Scaled flow-directions at the plasmapause. Figure and caption from *Goldstein et al.* (2004c).

This dissertation makes use global images of the plasmasphere in three studies. The first study shows correlations between the plasmasphere and the upstream solar wind. The second study explores how open/closed drift path boundary motion can be used to calculate the global cross tail electric field magnitude. The third explored the ionospheric influence

¹AKR is intense radio radiation emission mainly generated from cyclotron radiation. The radiation has a frequency of between 50 and 5000 kHz.

on plasmaspheric corotation and corotation lag.

CHAPTER 2

CORRELATION BETWEEN PLASMAPAUSE POSITION
AND SOLAR WIND PARAMETERS

The average plasmopause radial position is highly dependent on the electric field convection pattern in the inner magnetosphere. We present correlations relating the plasmopause position directly to interplanetary parameters. The plasmopause position is found to be strongly correlated with the interplanetary magnetic field (IMF) B_z component, IMF clock angle, and ϕ , a merging proxy. Delay in the plasmopause response to the arrival of the conditions measured by the ACE spacecraft of both IMF B_z and IMF clock angle at Earth is found to be 180 min while the delay to the arrival of ϕ is found to be 240 min. A relationship is derived between IMF B_z , ϕ , and the plasmopause position. Avoiding the use of geomagnetic indices removes any requirement for knowledge of the current state of the magnetosphere. This chapter is an expanded reproduction of the journal article *Larsen et al. (2007)*.

Introduction

The location of the plasmopause is known to vary with geomagnetic activity (*Chappell et al., 1970a; Carpenter, 1970*). Recent work by *O'Brien and Moldwin (2003)* and *Moldwin et al. (2002)* has shown correlations between *in-situ* radial plasmopause position determinations and several geomagnetic indices, including K_p , AE , D_{st} , AU , AL , ASY , and ΔD_{st} . They suggest that both convective and substorm electric fields are involved in the determination of plasmopause position due to a stronger correlation between the plasmopause position and AE than with AL or AU . The best model discovered by *O'Brien and*

Moldwin (2003) (as defined by a strong correlation) is based on the minimum D_{st} in the previous 24 hours suggesting that D_{st} is a better proxy for the maximum convection electric field strength than is K_p . They also separate out the differences between parameters responsible for fast relative motion of the plasmopause (ΔD_{st} , ASY) and for the absolute plasmopause position ($\min D_{st}$, K_p). The study shows a clear indication of the importance of geomagnetic activity in determining the state of the plasmasphere and the difference in the effectiveness of the various parameters.

Changes in the strength of the inner magnetospheric convection electric field alter the local particle drift paths which in turn determine the size of the plasmasphere and correspondingly the location of the plasmopause (*Kavanagh et al.*, 1968). Computations of the convection electric field have advanced from the simple uniform convection electric field model of *Kavanagh et al.* (1968) to the various electric field models based on the Volland-Stern electric field model (*Stern*, 1975; *Volland*, 1978). The latter allows inclusion of some shielding effects. The further addition of sub-auroral polarization streams (SAPS), over-shielding, and other localized phenomena (*Goldstein et al.*, 2002a, 2003a, 2004a) to the field structure has allowed the introduction of localized structure on the average plasmopause.

In this study we explore correlations of upstream parameters with the average plasmopause position. The parameters explored include the raw ACE measurements together with several derived parameters. The ACE spacecraft sits at the first Lagrange point, between the Earth and the Sun located at $x = 1.488499 \times 10^6$ km, $y = 151757$ km, $z = 102417$ km in the Geocentric Solar Magnetospheric (GSM) coordinate system, making near continuous measurements of the solar wind as it passes the satellite (*Stone et al.*, 1998). These include the IMF magnitude ($|B|$), x, y, z components ($B_{x,y,z}$), root-mean square rate of change (dB_{rms}), and several angles measuring the orientation (δ, λ, θ). Where δ is the angle between the B_r/B_t plane toward B_n where B is measured in the Radial/Tangential/Normal (RTN) coor-

dinate system, δ is also known as the RTN latitude. The angle λ is the RTN longitude and is measured between B_r toward B_t . Finally, the angles θ is the IMF clock angle in the $y-z$ plane $\left(\theta = \arccos \frac{B_z}{\sqrt{B_y^2 + B_z^2}}\right)$. Particle measurements include the solar wind proton velocity (V_{sw}), the x, y, z components of the velocity ($V_{x,y,z}$), proton number density (N_p), proton temperature (T_p), and the ratio of α -particles to protons (α ratio). Included for this study are several derived parameters, including the solar wind dynamic pressure ($P_{dyn} \propto N_p V_{sw}^2$), a merging proxy defined by *Kan and Lee* (1979) ($E_{kl} = VB_T \sin^2 \frac{\theta}{2}$), and a polar cap potential parameter defined by *Akasofu* (1979); *Reiff et al.* (1981), ($\phi = VB \sin^2 \frac{\theta}{2}$). Of these parameters the only ones to show a strong correlation at a particular time delay are the interplanetary magnetic field (IMF) B_z component, the IMF clock angle, θ , and the merging proxy, E_{kl} . Studying the time delay between changes in interplanetary conditions and any effect that can be seen in the plasmasphere provides information both on the response or the inertia of the magnetosphere and also possible mechanisms involved in propagating the effects inward. Response times of the plasmasphere to changes in various conditions in the upstream solar wind have been touched on by several authors (*Brandt et al.*, 2002; *Goldstein et al.*, 2002a, 2005) but never rigorously computed.

Using inversions of the EUV plasmaspheric image data we are able to monitor the entire plasmopause for extended periods providing excellent statistics. In this initial study we have used an average plasmopause position determined by averaging in magnetic local time (MLT) along the actual boundary. This effectively removes local plasmopause features such as bite-outs, shoulders, notches, and undulations which have no place in a statistical study of this nature. A study which includes MLT dependence is beyond the scope of this dissertation but is a possibility for future work. Correlations and time delays between solar wind parameters and plasmopause position (averaged in MLT) provide information both on the overall effect of different upstream parameters on the plasmasphere and how this relates to the magnetosphere as a whole.

Data

This study makes use of both the ACE interplanetary field and particle data sets as well the IMAGE EUV plasmaspheric images. The EUV instrument measures the global distribution of He^+ by imaging the resonant scattered emission at 30.4nm (*Sandel et al.*, 2000). Each image pixel provides the He^+ column density along a line of sight. The images can be inverted to give a mapping of the He^+ density in the SM equatorial plane. The inversion technique is described by *Gurgiolo et al.* (2005) and in the following section.

EUV Data Inversion

An EUV image is a two dimensional representation of the three-dimensional plasmaspheric He^+ density profile. Under the assumption that the He^+ density is constant along L , the images can be inverted to produce two-dimensional density maps of the He^+ ion population in the geomagnetic equatorial plane. The constant density along L is not a very good assumption however empirically the difference between constant and a power law dependence is negligible in the viewing of the inverted image, so the computationally simpler constant will be used. This provides the advantage of being a qualitative measure of the number density ($\#\text{cm}^{-3}$) as opposed to a line of sight integrated intensity ($\#\text{cm}^{-2}$). The EUV data inversion has been published by *Gurgiolo et al.* (2005); *Larsen et al.* (2007) and is reproduced and expanded here for convenience.

In the inversion the magnetic field is assumed to be dipolar throughout the inversion region which in the inner magnetosphere is a very good approximation and significantly simpler than a more realistic field map. Most often the plasmasphere lies within an L of 4 during geomagnetically active periods and within an L of 5 during geomagnetically quiet periods neither region show a large departure from dipole magnetic field.

Proper treatment of background and noise reduction in the measured image is paramount

in the inversion. Background increases the error in the absolute density estimate and noise is a major source of instability in the inversion. Removing the background and noise is a two-step process. First, the instrument background is removed by computing the average count rate in each column (instrument pixel) of the image for a fixed rotation angle above and below the plasmasphere and subtracting this average from each pixel in the column. The resultant image is then passed through a despeckling algorithm to remove isolated isolated pixel clusters. The cluster size is nominally set to two pixels. Figure 2.1 shows the results of a typical background and noise removal. The left image is the original EUV image cropped to show just the plasmasphere region while the right is the background and noise reduced image. The inversion begins with the cleaned image.

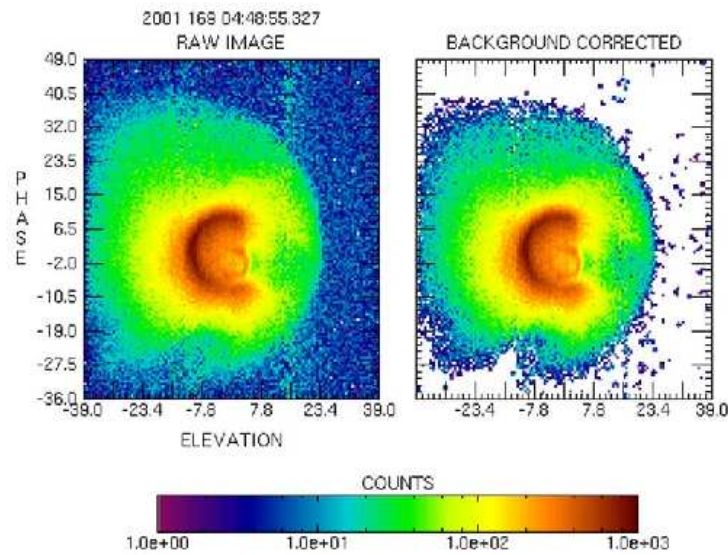


Figure 2.1: Measured EUV image (left) and the noise and background subtracted image (right). Figure from *Gurgiolo et al.* (2005).

The inversion uses an iterative approach in which an initial guess is modified repeatedly until it converges to a stable solution. The first step of the iteration is the formation of the zero solution and density matrices. Both matrices have identical order and represent a gridding of the geomagnetic equatorial plane in L -shell (L) \times geomagnetic longitude (Λ)

space. Both are over-dimensioned to give them a higher spatial resolution than the EUV measurements. This is necessary both for stability and smoothness in the final solution.

The density profile matrix holds the current density He^+ profile. The profile is initialized to a simple power law in L with no Λ dependence as

$$D = 10^{-0.715L} \quad (2.1)$$

The zero solution matrix holds a status flag for each grid in the density matrix. This flag is either zero or one, depending on whether the density of the grid is known to be zero or not. The matrix is initialized to all ones. Each EUV line of sight found to have a zero intensity is then mapped onto the zero solution matrix, and the grids it passes through are set to zero. Additionally, since the instrument measures column density, any pixel contained in a line of sight with a zero total intensity associated with it must itself have zero density.

Also set up in the initialization are the variable grids in the density matrix. These are the grids that are modified in each step in the iteration process and from which the new density matrix is built in each iteration step. There is one variable grid representing each instrument line of sight. This keeps the problem from being over constrained in the iteration phase of the inversion. The variable grids form a unique set of unknowns and are set to the grids containing the closest approach to the Earth of each line of sight.

Each iteration step begins with the construction of a synthetic image from the current density profile matrix. This is done in three steps. First, the zero solution matrix is used to mask off the zero intensity grids in the density matrix. Second, the column abundance along each of the instrument lines of sight is then computed from the modified density matrix. Any line of sight that is found to have only a single nonzero density and having zero neighbors is set to zero and the zero solution matrix is updated. Lines of sight which have only a single nonzero value are generally noise that was not caught in the initial noise

and background removal. Finally the column densities are modified by the instrument characteristics and the synthetic image is produced.

The mean square deviation between the synthetic and measured image is then computed and compared to mean square deviations computed in previous iteration steps to see if a convergence has been reached. If so, the iterations are terminated and the current density profile is returned.

When convergence has not been obtained, the measured image is divided by the synthetic image to produce a correction value for each line of sight. The density matrix is rebuilt using only the variable grid values multiplied by their corresponding correction value. All unassigned grids in the density profile matrix are filled using a 2-D linear least square fit algorithm. Last, the zero solution mask is applied to give the new density profile and a hot spot check is made. This is a search through the matrix for pixels which have intensities larger than their neighbors by some preset value. Such pixels represent solutions which are either currently, or in the process of becoming unstable. Their density is adjusted to the average value of their nearest neighbors. The iteration step then restarts with the computation of a new synthetic image. Figure 2.2 shows a sequence of inverted images for comparison against the EUV images in figure 1.9.

It should be noted that the inversion makes no special provision for either the dayglow contamination in the near-Earth sunlit portion of the EUV images, nor the dimmer plasma-sphere seen within the Earth's shadow. Both are treated in the inversion as real phenomena. This results in an anomalous density enhancement in the sunlit sectors and a density depression directly anti-sunward of the Earth, these features are visible in all inversions.

Inversion Method Base assumptions in the inversion:

- A. Density is constant along any L -shell at a specific Solar Magnetic (SM) longitude.

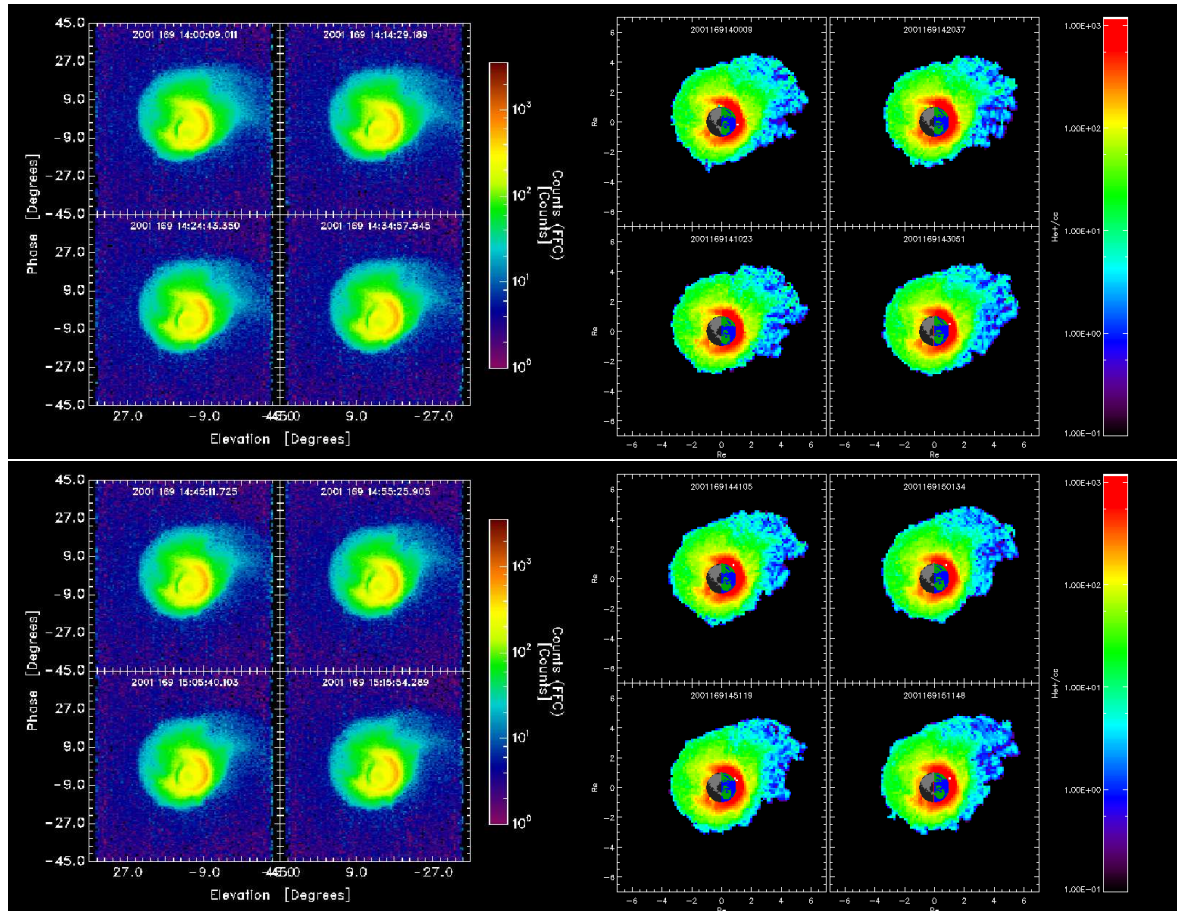


Figure 2.2: (right) EUV images between 2001-169 14:00 and 2001-169 15:15 (18Apr2001), in each the Sun is to the lower right as demonstrated by the airglow. There is a large plasmaspheric plume in the upper right of each image. (left) Inversions of the EUV images for comparison. In the inversions the Sun is to the right and the units are now $\text{He}^+ / \text{cm}^3$ and all look effects are removed.

B. The magnetic field can be approximated using a dipole formulation.

Algorithm steps:

1. Form raw EUV image from the data as a function of spacecraft phase angle and instrument elevation angle. In this image each pixel represents a line of sight of the instrument.
2. Do any noise reduction at this point. This included removing sensor noise on the pixel level and isolated active pixels.
3. Compute the lines of sight in SM coordinates for each pixel in the raw image.
4. Map the raw EUV image into matrix which is dimensioned L by SM longitude. The mapping is done by assigning an (x,y) to each line of sight which is its closed approach to the SM origin and computing L and the SM longitude at that position.
 - a) Since this is a non-linear mapping there will be empty grids in the SM matrix if the resolution was set near that of the raw matrix. These are filled using a 2D least squares algorithm.
 - b) The filled grids need to be marked since they do not contain "real" data are are not included in some steps in the inversion.
5. Build a zero solution matrix using the same matrix format as (3). This is built by
 - a) Set all matrix elements to 1.0
 - b) Find all lines of sight which have 0 intensity.

- c) Walk down those lines of sight using a step size dS . At each step compute L and the SM longitude and set the corresponding grid in the zero solution matrix to 0.0.
6. Form the unrestricted solution matrix. This has the identical order and uses the same coordinates as (3)
 7. Make initial guess at a solution. The guess that is that the helium ion density in the plasmasphere follows the formula $D = 10^{-0.715L}$. This has no longitudinal variation and no cutoff in L .
 8. Do a grid by grid multiplication of the zero solution matrix with the solution matrix to obtain the restricted solution.
 9. Do a numerical integration over each line of sight using the restricted solution matrix to obtain the helium ion density at the different L , SM longitudes. From this restricted solution matrix a synthetic raw image in the format of (1) is produced.
 10. Get the variation of the synthetic to measured image ratio to produce a variance. If the change in the variance is within some tolerance then a solution has been reached.
 11. Reform the unrestricted solution matrix adjusting each grid point which is associated with a line of sight by $V \times cDm/cDs$ where V is the current density assigned to the grid, cDm is the measured column density and cDs is the synthetic column density computed for the line of sight from the previous solution matrix.

12. Scan new solution matrix for "hot spots" and deal with them. Hot spots are grids points whose column density exceeds their neighbors by some factor. Hot spots are generally set to an average of their neighbors column densities.
13. Go back to 8 and continue.

Plasmapause Determination

The plasmapause is determined from the equatorial density maps derived in the inversion using a semi-automated procedure developed for this study. Other researchers such as *Carpenter and Anderson (1992)*; *O'Brien and Moldwin (2003)* have taken an operational definition of the plasmapause as the innermost factor of 5 drop in density in less than 0.5 Earth radii (R_E), we adopt the same definition in this study. The definition does not handle times when the plasmapause is observed as a gradual decline in density sometimes stretching to geosynchronous orbit. Generally in these cases the location of the plasmapause will be underestimated. Figure 2.3 shows an example of the global plasmapause determination from the semi-automated plasmapause locator. Each plus sign (+) in the figure marks the plasmapause and is obtained by computing the density gradient along a radial cut and setting the plasmapause at the outside location which meets the criteria stated above for a $0.5R_E$ sliding window. This removes any subjectiveness from the process of the plasmapause determination which is often present when hand selecting the locations. Each mapping can be quickly scanned for accuracy to be sure that we are not, for example, setting the plasmasphere at the outer edge of a drainage plume (*Goldstein et al., 2004b*) rather than at the edge of the bulk plasmasphere. Badly determined points are manually deleted from the plasmapause data sets prior to usage.

The base data set used in this study consists of 1365 global images with derived plasmapauses. Figure 2.3 is representative of a plasmapause determination. All of the plasma-

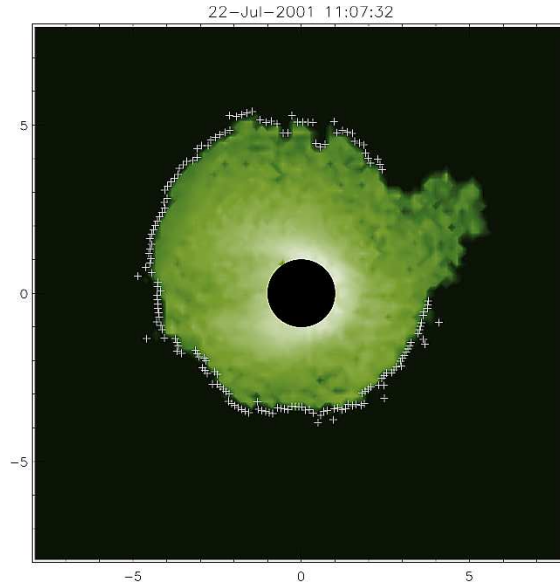


Figure 2.3: Example inverted EUV image with the semi-automated extracted plasmopause overplotted. The Sun is to the right and the “bulge” at about 1300 MLT is an anomaly in the data (light contamination) and therefore does not have plasmopause points for that region.

pauses used in this study come from images taken in 2001. While most consist of full MLT coverage, some have only partial coverage due to data dropouts and light contamination in one of the three IMAGE EUV heads. Averaging in radial distance over each plasmopause position in a given image (over all MLT) provides a single plasmopause location which is used in the analysis denoted L_{pp} . This is a rough estimator but provides a general parameter that is the overall plasmasphere size.

Data from the ACE spacecraft (*Stone et al., 1998*) are used to provide the interplanetary indices used in the correlative study. The data are binned to 10 min averages to match the IMAGE EUV accumulation time. This averaging also acts as a smoothing filter on the interplanetary data. Each 10 min ACE average is time delayed by the measured solar wind speed to the Earth before usage in the correlation analysis, this is performed as $ACE_POS_X/V_{sw,x}$ which is the GSM x -coordinate of the spacecraft divided by the x -velocity of the solar wind.

Analysis

The analysis consisted of first identifying a large number of interplanetary parameters and indices which could be either obtained directly or constructed from the ACE data sets and which might be candidates to show a correlation with average plasmopause location, L_{pp} as defined above. Initial tests showed both the ACE and plasmopause data to be free of significant autocorrelated errors which removed the need to correct for these (*Neter et al.*, 1996). Each of the identified solar wind delayed ACE generated parameters was then correlated with L_{pp} using a nonparametric, rank-order correlation analysis which make it unnecessary to have any information about the underlying distribution of the data (*Press et al.*, 1992). The Spearman rank-order correlation method was used throughout. The first correlation coefficient is generated using a delay time of -20 minutes (20 minutes into the future). Successive coefficients were generated by incrementing the delay time by five minutes at each step, stopping at a delay time of 600 minutes. Each delay represents a plasmaspheric reaction time. A parameter which is correlated with the average plasmopause location exhibits either a peak or valley in its spectrum at the most probable delay time. A negative time delay (occurrence before the fact) and a zero time delay (instantaneous reaction) are not considered physical solutions since we assume that there is a least some time delay associated with each response of the system to changes in the external parameters.

The initial set of correlations yielded only three parameters which were found to exhibit a significant correlation peak with L_{pp} . These were the IMF clock angle (θ), IMF B_z component, and the merging proxy, ϕ , defined in equation 2.3. IMF B_z is one of the directly measured ACE products, the IMF clock angle is defined in terms of IMF B_y and B_z as

$$\theta = \arccos \left(\frac{B_z}{\sqrt{B_y^2 + B_z^2}} \right) \quad (2.2)$$

and ϕ is defined as

$$\phi = vB \sin^2(\theta/2) \quad (2.3)$$

where v is the solar wind speed, B is the magnitude of the IMF, and θ is the IMF clock angle from equation 2.2.

The correlations for each of the three parameters above is shown in Figure 2.4. Also shown is the correlation derived for the solar wind pressure (P_{dyn}). The latter is included to show an example of a parameter showing no correlation peak with L_{pp} . With the exception

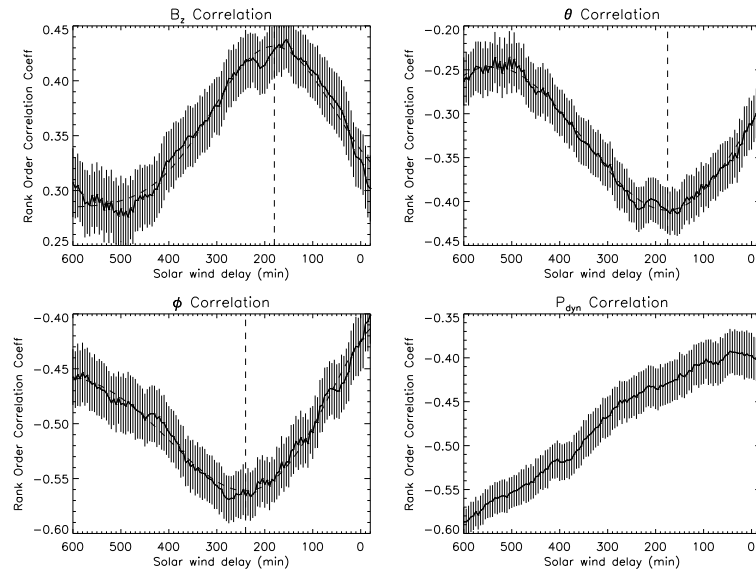


Figure 2.4: Rank order correlation coefficients as a function of solar wind delay (reaction time). The error bars denote 1σ confidence found using bootstrap resampling with replacement. The dashed vertical line denotes the strongest correlation and the dashed lines show a Gaussian fit to the curve used to find the peak.

of the P_{dyn} correlation in the lower right-hand plot, each plot shows a significant peak or valley in its correlation which occurs at the most probable delay time between the measured parameter arriving at Earth and its impact on the location of the plasmopause. The arrival

at Earth is used to avoid ambiguities in the location of the magnetopause. The absence of a peak in the P_{dyn} correlation delay plot indicates that the value of the dynamic pressure has no systematic affect on the plasmopause location. This is not to say that the arrival of interplanetary shocks, high speed streams, and other fast fluctuations of pressure have no effect. They do, but there is no effect for slow changes and near steady state values of the dynamic pressure.

The peaks in the correlated parameters have different widths and positions. The maximum correlation peak in B_z occurs at a delay of 180 min, the θ correlation peak occurs at a delay of 175 min while the ϕ delay is 240 min. The curves relating to B_z and θ are identical within the error bars. (In fact they are essentially identical but mirrored about the abscissa.) This indicates that at the level of precision shown here B_z and θ have the same effect, or more simply only one of them needs to be considered in the end analysis. This is not a surprise as $B_z = B \cos \theta$ and B does not exhibit a correlation peak.

Once the delay times are calculated the next step is to derive expressions which relate the position of the plasmopause as a function of each parameter using the indicated time delay. Using the delay times indicated above ($B_z, \theta : 180$ min, $\phi : 240$ min) the linear regression equations are shown in Table 2.1. The single regression equations yield the following maximum and minimum plasmopause locations for the indicted range of each parameter: $2.99 < L_{B_z} < 4.83$, $3.55 < L_{\theta} < 4.59$, and $2.95 < L_{\phi} < 4.53 R_E$ for B_z , θ , and ϕ respectively.

Creating one multiple regression equation for the plasmopause from all the parameters (with the appropriate delays for each) yields

$$L_{pp} = 0.050B_{z,180} + 0.108\theta_{175} - 1.110 \times 10^{-4}\phi_{240} + 4.23 \quad (2.4)$$

Table 2.1: Equations relating plasmasphere position to the three solar wind parameters studied in the paper. Parameters studied are IMF B_z , IMF clock angle, θ , and polar cap potential drop, ϕ , as defined in equation 2.3. The uncertainties are 1σ confidence found using bootstrap resampling with replacement. Note that NC^{-1} is a Newton per Coulomb.

Parameter	Slope	Intercept	Range
B_z (nT)	$0.062 \pm 0.0027 \text{ nT R}_E^{-1}$	$4.11 \pm 0.018 \text{ R}_E$	$-18.01 \rightarrow 11.48$
θ (rad)	$-0.33 \pm 0.021 \text{ rad R}_E^{-1}$	$4.59 \pm 0.040 \text{ R}_E$	$0.016 \rightarrow 3.14$
ϕ (NC^{-1})	$-1.97 \times 10^{-4} \pm 8.2 \times 10^{-6} \text{ NC}^{-1} \text{ R}_E^{-1}$	$4.53 \pm 0.022 \text{ R}_E$	$0.800 \rightarrow 8017.8$

The 1σ bootstrap uncertainties computed for the B_z , θ , ϕ slopes, and the intercept are 0.0068, 0.035, 1.59×10^{-5} , and 0.060 respectively. The subscripts on each variable is the delay associated with each parameter. Equation 2.4 states that B_z can act to both increase and decrease the average radial position of the plasmopause (B_z can be positive or negative), θ acts to increase the radial location and then only by a small amount, and ϕ acts to decrease the average radial position. The total change in the plasmopause radial location available from each parameter is 1.47, 0.34, and 0.89 R_E for B_z , θ , and ϕ respectively showing that the important parameters are B_z and ϕ . A statistical t -test verifies that the θ coefficient is not statistically different from zero.

Omitting the clock angle in the multiple regression analysis yields the equation for the plasmopause location below which as might be expected is almost identical to equation 2.4.

$$L_{pp} = 0.0374B_{z,155} - 1.05 \times 10^{-4}\phi_{275} + 4.38 \quad (2.5)$$

Figure 2.5 is a graphical representation of the data used to derive equation 2.5 with B_z and ϕ varying along the abscissa and ordinate respectively and the average radial plasmopause position shown a color. It is easy to see that a large plasmasphere occurs when ϕ is at its lower range with a higher probability when B_z is positive than when it is negative (as might be expected in quiet time conditions).

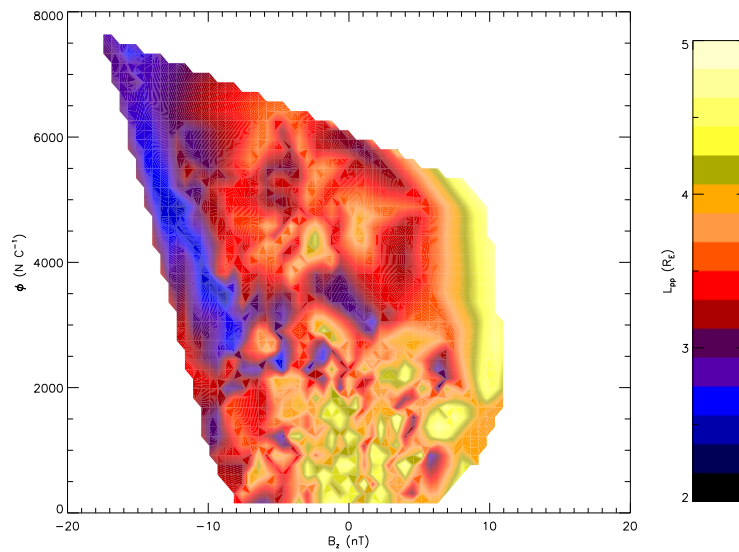


Figure 2.5: Contour plot showing the plasmopause reaction to different observed combinations of IMF B_z and the merging proxy, ϕ .

Other Tested Parameters

The list of parameters that were tested for a correlation peak include every measurement from the ACE spacecraft as well as several derived quantities from those parameters. Table 2.2 shows the parameters tested for a definite correlation peak and the results of the analysis. Notice that few of the parameters exhibit a definite peak, however, there were several that had weak peaks that were not statistically significant (peak shorter than the error bars).

Table 2.2: Tested correlation parameters

Parameter	Peak	Comment
$ B $	yes	See figures 2.6, 2.4. Very weak (not statistically significant)
B_x	yes	very weak (not statistically significant)
B_y	yes	very weak (not statistically significant)
B_z	yes	
$\min(B_z, 10 \text{ min})$	yes	
$V_{sw} (V_p)$	yes	See figure 2.6. Very weak (not statistically significant)
V_x	no	
V_y	no	
V_z	no	
$E_{kl} = VB_T \sin^2 \frac{\theta}{2}$	yes	very weak (not statistically significant)
$\phi = VB \sin^2 \frac{\theta}{2}$	yes	See figure 2.4.
$\theta = \arccos \frac{B_z}{B_T}$	yes	
dB_{rms}	no	
λ	no	
N_p	no	
T_p	no	
α ratio	no	
δ	yes	very weak (not statistically significant)

There are physical arguments for believing that the solar wind velocity and the magnitude of the IMF might play an important role as they are both fundamental in the formation and dynamics of the magnetosphere. Taking a closer look at these parameters however, shows that the correlation delay $|B|$, shown in Figure 2.6, is a weak peak and arguably not statistically significant, as it is not larger than its error bars. The peak is probably a result of the B_z inclusion in the parameter. We believe that IMF $|B|$ does not play a role in plasma-pause location, as the magnetosphere sets up shielding for the inner magnetosphere and plasmasphere, so IMF magnitude is not important only its z -component and for impulsive events not studied here its rate of change.

Also shown in Figure 2.6 is the correlation delay curve for solar wind proton velocity V_{sw} . There is no significant correlation peak for this parameter. This parameter is ignored as the error bars allow one to draw a straight line through the plot. It is interesting that the

correlation for V_{sw} doesn't show a peak, as this implies that the dynamics controlling the plasmopause position are influences more magnetic forces than pressure forces.

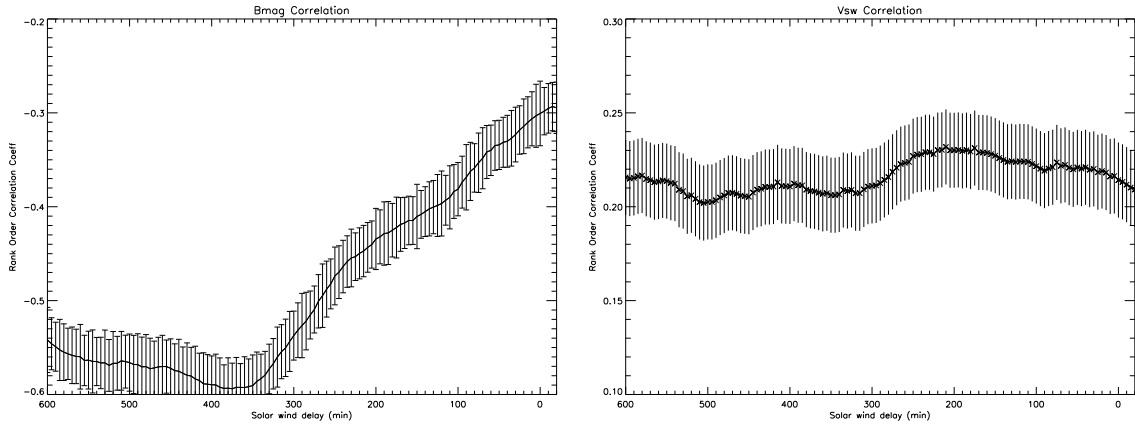


Figure 2.6: Plots of the correlation as a function of delay for IMF magnitude, $|B|$ and solar wind proton velocity, V_{sw} .

Discussion

Correlation provides a simple means to test for the dependency of one variable on another. In this case, because the correlations are made against time, they also can be used as a predictive tool that allows knowledge of the upstream conditions to be translated with some degree of confidence to conditions at the plasmopause. The large response time in the correlations coupled with the propagation time of the observations at ACE to the Earth allows for L_{pp} to be estimated 3 to 4h in the future from the real time solar wind measurements.

It is important to remember that the delay times given in a correlation analysis are valid for the 10 min smoothed interplanetary parameters, impulsive events including shocks and IMF turnings are not covered in this analysis. We studied the relaxation times of the magnetosphere to a changing input. The system will respond to impulses in any parameter on time scales faster than that produced in the correlations but the time required for the system

to reach its final state will be on the time scales similar to those derived in the correlations. As an example, *Goldstein et al.* (2003a) have reported response times of 32 min from the southward turning of B_z to the start of the erosion of the plasmasphere which is considerably more rapid than the 180 min response time predicted in the correlation for B_z . These quick changes in plasmopause position are seen in the statistical study as only starting and ending points of the erosion.

Both B_z and ϕ represent proxies for either conditions or mechanisms in the inner magnetosphere that establish the average radial location of the plasmopause. There is no known direct relationship between the interplanetary conditions and L_{pp} . As such they do not, in themselves, detail how the changes in the L_{pp} occur and must be associated with processes which set up the convection electric field. The key is then to identify the conditions or mechanisms which each proxy represents.

The average plasmopause location is controlled by the combination of the co-rotational and convection electric fields with the convection electric field forming the variable part of the system. It is reasonable to expect then that both B_z and ϕ are proxies for some aspect in the setting up or regulation of the convection field.

It is not surprising that B_z is strongly correlated with L_{pp} . When B_z turns southward, subsolar reconnection becomes possible, increasing the convection electric field. The correlation puts the delay between the arrival of B_z and the new plasmopause position at about 2.5 h.

The correlation of ϕ with L_{pp} is not as obvious as that of B_z . While it contains a dependence on B_z and appears as it should be a reasonable proxy for the interplanetary electric field, it has a significantly longer delay time than associated with B_z which suggests coupling to an additional process. It is reasonable to assume that 3 h of the 4 h response time seen in the correlation is derived from the B_z dependence in the parameter. The source of the remaining hour has yet to be identified but may derive from processes associated with

the reconnection of the draped solar wind fields lines in the tail. The four hour delay time indicated in the correlation is in agreement with the decay times associated with shielding affects mentioned by *De Zeeuw et al. (2004)*; *Peymirat et al. (2000)*; *Goldstein et al. (2002a)*.

The simple picture provided by equation 2.5 and including the known plasmaspheric response to impulsive changes in B_z goes as thus. There is a southward turning of the interplanetary field after which the field remains constant. After approximately 30 min of the interplanetary field turning southward the plasmasphere begins to erode in response to changes in the overall convection field. As the interplanetary conditions steady, the delay between the plasmasphere response to the external changes lengthens to about 3 h. This can be viewed as the continuation of the response to the initial turning proceeding at an overall slower pace. Shielding, overshielding, and SAPS which may have been initially set up now begin to decay modifying the convection field and driving the plasmopause further inward to reach its minimum extent at about 4 h from the initial onset. The process reverses when B_z returns northward.

Conclusion

The ability to predict the plasmopause location based solely on upstream parameters is a first step in a predictive model. Using an upstream monitor such as ACE we can predict the position of the plasmopause at a time in the future determined by equation 2.5 plus the propagation time of the solar wind.

Future work will provide the plasmopause location as a function of MLT. Correlations will then show whether the plasmasphere responds as a whole to the changes in the interplanetary conditions or whether different regions respond differently. These future studies, in turn, can be used to provide estimates of the convection electric field which is the ulti-

mate driver of the plasmopause location.

CHAPTER 3

CROSS-TAIL ELECTRIC FIELD MAGNITUDE DERIVED FROM
PLASMASPHERIC ALFVÉN LAYER MOTIONSIntroduction

The plasmapause is a highly dynamic boundary, whose location and shape is controlled by the local magnetic and electric fields. *Carpenter* (1963) found the plasmasphere became depleted in density with increasing magnetospheric convection, as represented by the Kp index. Using ground-based whistler measurements, *Carpenter* (1966) statistically mapped out the 2D geomagnetic equatorial plasmapause location showing the characteristic duskside bulge. The influence of geomagnetic activity on plasmapause location was demonstrated by *Chappell et al.* (1970a) who found its location in L ordered by Kp. There is considerable variation both in the thickness and appearance of the boundary between inbound and outbound crossings within a single satellite orbit (*Harris et al.*, 1970). This suggests that the plasmapause is anything but a simple boundary, having significant structure, both radially and azimuthally.

A complete explanation of the mechanism(s) responsible of the morphology of the plasmasphere especially the morphology of small scale features has yet to be found. The macrodynamics are easily explained by a convective plasmasphere model, which is based on the superposition of the cross-tail convection electric field and the Earth's corotation electric field. $\mathbf{E} \times \mathbf{B}$ drift of the local plasma is responsible for the general plasmasphere shape including the dusk-side bulge (*Grebowsky*, 1970; *Mayr et al.*, 1970; *Maynard and Chen*, 1975; *Volland*, 1978; *Stern*, 1981; *Doe et al.*, 1992; *Toffoletto et al.*, 2003). In a convec-

tive plasmasphere model the steady state plasmopause is identified as the location of the last closed streamline, known as the plasmaspheric Alfvén layer. Near 1800 MLT there is a single position where the corotation and convection fields cancel each other exactly. In general because of the difference in the response times of the plasmopause and Alfvén layer to changes in the intensity of the cross-tail electric field the two only coincide during extended quiet periods.

As the Alfvén layer moves inward due to increased convection, plasma once on closed drift paths finds itself on open drift paths allowing it to drain from the flux tube (*Carpenter, 1970; Carpenter et al., 1993*). As the convection field weakens, the Alfvén layer moves outward allowing open drift paths to close and then refill with plasma from the ionosphere. Changes in field strength propagate at the local Alfvén speed while the bulk plasma takes significantly more time to react. The bulk plasma can only move at $\mathbf{E} \times \mathbf{B}$ drift speeds which are orders of magnitude smaller. This reaction time difference enables the formation of macro-features such as plasmaspheric drainage plumes and wrapping plumes, as postulated by *Grebowsky (1970); Maynard and Chen (1975)* and as observed using IMAGE-EUV data by *Goldstein et al. (2003a)*. The difference in reaction times allows for observations of the Alfvén layer position interior to the plasmopause, thus allowing the calculation of the convection electric field.

The Alfvén layer as the boundary of open and closed drift paths observationally is identified by a local shear with plasma on the Earthward side dominated by the corotational forces and the far side by the convection electric field. Using IMAGE-EUV images the Alfvén layer is readily observed within the plasmasphere by tracing a feature. Tracing a feature in a time series of EUV images noting the L -value and MLT where its motion changes from corotation to either subcorotation or supercorotation allows for the derivation of the convection electric field. There has been recent work by *Burch et al. (2001); Goldstein et al. (2003); Sandel et al. (2003); Goldstein et al. (2004c); Gallagher and Adrian*

(2007) focusing on plasmaspheric erosion and the electric fields involved in the erosion in localized regions and their affects on the plasmasphere. These previous methods have succeeded only in deriving the electric fields for events where discernible plasmopause motions are visible. This dissertation extends IMAGE-EUV electric field derivations to time periods where motions are visible within the plasmasphere as well as focusing on the global convection electric field, providing for the first time, observational verification of the Alfvén layer motion.

This chapter extends the Alfvén layer theory by incorporating observational data, which allows for the derivation of the convection electric field. The derived Alfvén layer position and global convection electric field will be presented. Presented is a method by which the Alfvén layer boundary can be tracked in time within the plasmasphere during a plasmaspheric erosion event. From Alfvén layer motion the cross-tail convection electric field can be derived assuming a convective plasmasphere field pattern. In order to observe the Alfvén layer, plasmaspheric features must be seen to change from closed to open drift paths (i.e. from corotation to sunward convection). This change is most evident in the dusk sector where the convection and corotation fields are anti-parallel, causing the plasma drift direction to change drastically as the influence changes.

EUV Derived Convection Field for 8 April 2001

Data

The main data set used in this study are images from the Extreme Ultraviolet (EUV) imager flown on the IMAGE satellite. The EUV data are described in detail in Chapter 1. The images are inverted using the method in Chapter 2. Using the inverted images a set of UT-MLT stackplots are created which allow motions within the plasmasphere to be

observed and tracked.

UT-MLT Stackplot Each UT-MLT stackplot displays the inverted density from within a fixed Earth centered annulus as a function of UT which runs up the ordinate and MLT which runs along the abscissa. An annulus is selected in an image then “cut” at 0000 MLT and laid on the plot. The same annulus from the next image is then laid above the first making time progression of features more obvious than in individual images or movies of images. Figure 3.1 shows an example stackplot and an inverted image. In a stackplot, a single inversion is represented by a horizontal band of data centered on the inversion time. Each horizontal band represents a 10 minute accumulation time for the image. The color bar used in the stackplots is a *linear* scale as opposed to the inverted images which are typically shown with a log scale. Lines of corotation are overplotted on the stackplots to assist in feature tracking. The radial distance across the annulus can be any size, this study uses a distance of $0.5 R_E$ which was found to optimize the visibility of the Alfvén layer.

The plot format is optimized for detecting the azimuthal motion of features in the plasmasphere as a function of both time and radial position. Rotations are represented in the plot by the slopes of the various features, such as the density depletion centered at 1800 MLT. Features which have a slope less than the corotation lines are super-corotating and those with a slope greater than the lines are sub-corotating. Features stationary in MLT will appear vertical in the plot and features which slant in the opposite direction are moving opposite the corotation direction. It should be noted that tracking features does not depend on absolute density but relative density. This removes any need to worry about cross calibrating the inversion technique with *in-situ* He^+ measurements.

Stackplots Viewing the time evolution of a feature with a set of stackplots allows the location of the Alfvén layer to be determined from its motion. Figure 3.2 shows three

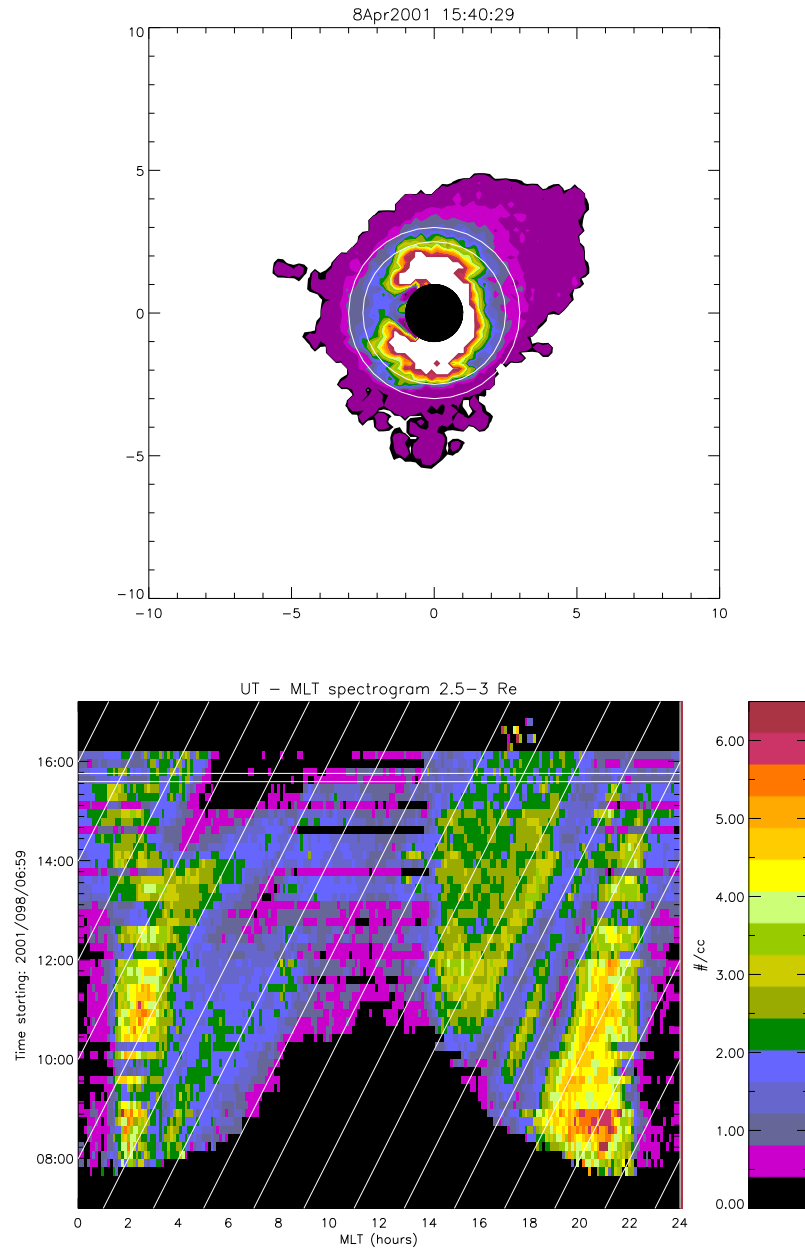


Figure 3.1: (Top) Inverted EUV image from 8Apr2001 15:40:29 highlighting the $2.5 - 3 R_E$ annulus used to create the stackplot, the sun is to the right. (Bottom) UT-MLT stackplot for the annulus from $2.5 - 3 R_E$ for each image in the orbit. Time of the image is plotted on the abscissa and MLT along the ordinate with He^+ density shown linear with color. The over plotted diagonal lines are corotation while the horizontal lines show the 10 minute duration of one image in the plot. The color bar ranges in each plot have been set equal, washing out the inverted image Earthward of the desired annulus.

stackplots from a sequence of images from 06:59 UT to 17:12 UT on 8Apr2001 (day 98). Each stackplot represents a different annulus of the plasmasphere. Shown are stackplots for $2 - 2.5$, $2.5 - 3$, and $3 - 3.5 R_E$. Each stackplot traces the evolution of the density depression along in the dusk sector. The plots show the stagnation of the feature begins earlier for more inner L-shells, just as would be expected for an external influence penetrating into the plasmasphere. Stagnation points occur where the plasma changes from closed to open drift path and back again. They are represented in the stackplots by a change of slope of the feature being tracked. The thick white line displaced 2 hours in MLT to the left of the feature has been manually added to each plot to assist in the tracking of the stagnation and corotation transitions.

Alfvén layer motion through an annulus is seen as a change in slope of the depletion. The positions and time of these slope changes yield the position of the Alfvén layer at a given time. Following the stagnated depression until it begins to corotate once again indicates that the Alfvén layer has moved out beyond the annulus, returning the plasma to corotation. Using this method beginning with the $3 - 3.5 R_E$ stackplot tracing the feature centered on the corotation guide line that begins at 1500 MLT there are three slope changes found at 10:59 UT, 12:31 UT, and 13:46 UT. Based on the slope transition, the Alfvén layer motion can be deduced to be inward or outward. Changes in slopes away from corotation are inward motions and changes toward corotation are outward motions. This is evident from considering the dominant field in each case.

The resolution of this technique is highly dependent on the shape and sharpness of the feature being tracked. The $2.5 - 3 R_E$ stackplot shows a very similar progression, showing stagnations at 11:14 UT, 11:36 UT, 13:59 UT, and 14:34 UT. Moving further inward the $2 - 2.5 R_E$ stackplot shows stagnations at 11:07 UT, 11:27 UT, 13:56 UT, and 14:25 UT. The resolution of the technique is set by the 10 minute time resolution of the EUV images. The actual resolution is probably a little larger. The transitions from corotation to stagnation,

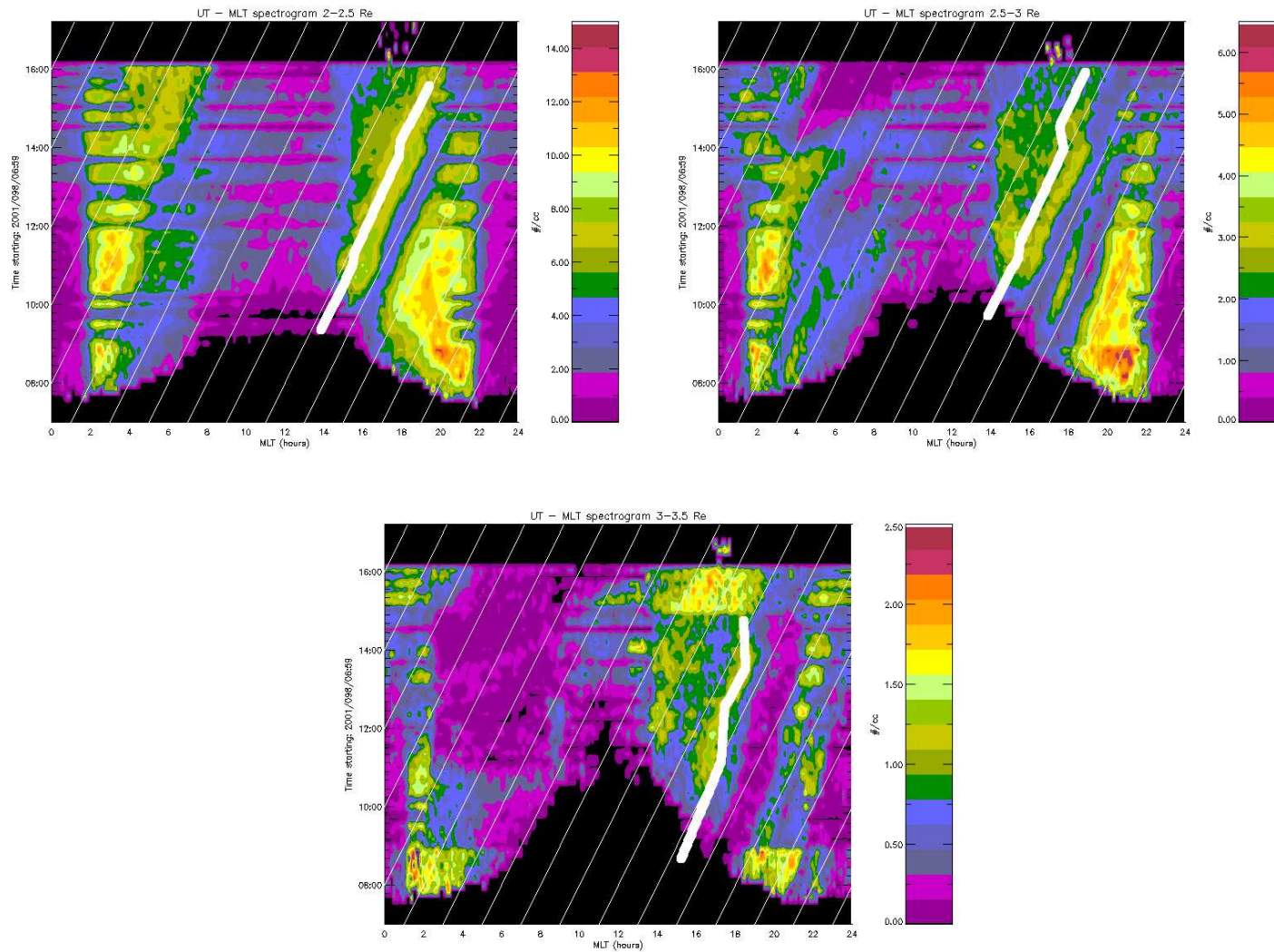


Figure 3.2: Stackplots from 8Apr2001 for the annuli from 2 – 2.5, 2.5 – 3, and 3 – 3.5 R_E . Overlaid on each plot is the shape of the depression feature that will be used to determine the Alfvén layer offset to the left of the feature. Plot format in each is the same as in Figure 3.1.

and stagnation to corotation are given in Table 3.1.

Table 3.1: Stackplot derived Alfvén layer position for 8Apr2001.

Stackplot	Time	MLT
2 – 2.5	11:07	17.4
2 – 2.5	11:27	17.4
2 – 2.5	13:56	19.8
2 – 2.5	14:25	19.8
2.5 – 3	11:14	17.4
2.5 – 3	11:36	17.4
2.5 – 3	13:59	19.7
2.5 – 3	14:34	19.5
3 – 3.5	10:59	19.2
3 – 3.5	12:31	19.5
3 – 3.5	13:46	20.7

Using data in Table 3.1 the motion of the Alfvén layer during the event is shown graphically in Figure 3.3. The blocks that touch the top and bottom of the plot can be considered to extend to infinity in each direction as there is no usable data for larger or smaller radii. It is clear that there are two distinct movements of the Alfvén layer. The Alfvén layer begins outside of $3.5 R_E$, then at 10:59 UT begins a rapid inward motion and within 15 minutes moves to within $2.5 R_E$. Then the Alfvén layer makes a slow (~ 1 hour) recovery to beyond $3.5 R_E$. This is followed by another rapid inward motion beginning at 13:46 UT. Over the next 30 minutes the Alfvén layer moves inward settling inward of $2.5 R_E$ and stays there for another 30 minutes, then retracts to $3 R_E$ where the orbit’s imaging sequence ends. In the next orbit the depression feature is corotating. In the following sections these motions will be put into a global context by examining the solar wind conditions and the convection electric field as derived from cross polar cap potential.

Interplanetary Data The analysis by *Goldstein et al.* (2003) of an event on 10July2000 shows that the arrival of a small interplanetary shock and a southward turning of the IMF

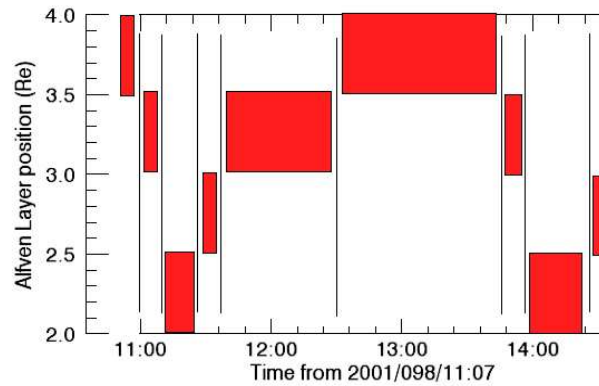


Figure 3.3: Alfvén layer position during the event, the red blocks show the position of the Alfvén layer during the time period.

is enough to start a major plasmaspheric erosion, triggering, a motion of the Alfvén Layer. However, study of this event does not show clear Alfvén layer motion due to lack of a traceable interior feature. For the 8Apr2001 event the interplanetary data are shown in Figure 3.4. The onset of a shock at 10:32 UT (left vertical line in Figure 3.4) set up the first Alfvén Layer motion (erosion) when it arrived at Earth 31 minutes later at 10:59 UT. The next Alfvén layer motion is not associated with a shock arrival but instead a sign change of the IMF-y component and a maximum in the clock angle. The dependence on the clock angle may derive from the long-standing relation between the IMF clock angle and the shape of the polar cap convection pattern which is directly related to the strength of the convection electric field (*Reiff et al.*, 1981; *Weimer and Gurnett*, 1993; *Weimer*, 1995; *Burke et al.*, 1999). The correlation of the upstream signatures with the Alfvén layer motion is a verification of the technique used to follow the plasmaspheric Alfvén layer motion.

Chappell et al. (1970a) has shown that the plasmasphere is ordered by Kp. We show both the Kp and Dst indices for the event in Figure 3.5. The indices show a relatively quiet period leading up to the sudden commencement reported in the NOAA Solar Geophysical Data records at 11:01 UT corresponding to the shock arrival (thin black line). The standard

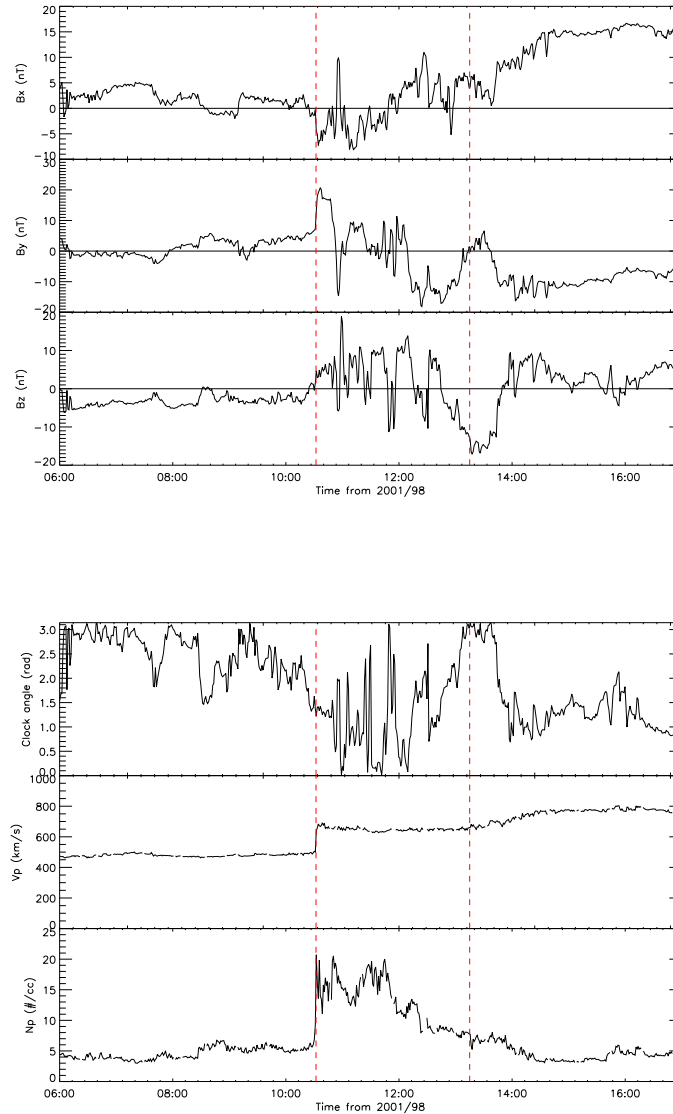


Figure 3.4: Interplanetary data from ACE for 8Apr2001. (top) IMF x, y, z components (bottom) IMF clock angle, Proton velocity (V_p), and number density (N_p). The first red vertical dashed line at 10:32 UT marks the time of the interplanetary shock at ACE located $233.6R_E$ upstream of the Earth. The second vertical line at 13:15 UT marks the seconds Alfvén layer motion at 13:56 UT from Figure 3.3 propagated back to ACE. Note the ACE data is not time-delayed to Earth, the delay is about 30 minutes at these solar wind speeds.

Dst 1-hour time resolution is too coarse to show a signature of the Alfvén layer motions, but, as marked by the vertical red lines, the two motions occur at the time of the sudden commencement and at the peak intensity of the storm. The standard 3-hour Kp index shows the expected increase but is too coarse to be useful predicting or understanding Alfvén layer motions.

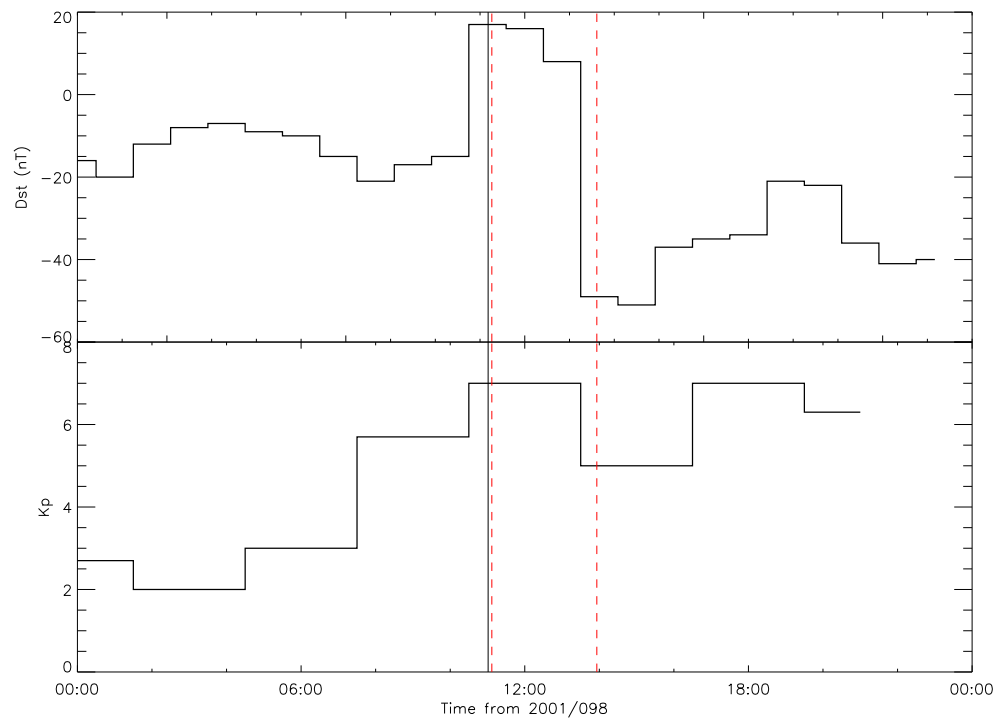


Figure 3.5: Dst and Kp indices for the time during and before 8Apr2001. The thin black vertical line on the plot is the sudden commencement. The red dashed lines are the minimum Alfvén layer positions from Figure 3.3.

Convection Field Strength

The coarse convection electric field strength can be derived from the understanding of

the behavior of the Alfvén layer motion expected on the basis of a convective plasmasphere model. The radial extent of the plasmasphere is a function of convection and corotation electric fields. Assuming the convection field strength is uniform, and oriented dawn-dusk, the convection field strength can be calculated from the Alfvén layer position. Although these assumptions are simplistic, having only a single point of Alfvén layer position makes using any more complex model an overstepping of the limitations of the available data. It is possible to derive an explicit relation between the convection electric field and the location of the Alfvén layer.

Following the derivation of *Lyons and Williams* (1984), beginning with the equations for the convection (1.4) and corotation (1.7) electric fields from Chapter 1, the boundary between open and closed drift paths occurs when the two fields are equal and opposite in the equatorial plane:

$$\hat{r}\omega\frac{R_E B_0}{L^2} = E_{sw} (\sin\phi\hat{r} + \cos\phi\hat{\phi}) \quad (3.1)$$

which occurs at 1800MLT ($\phi = \pi/2$) in steady state. Solving for L yields

$$L = \sqrt{\frac{\omega B_0 R_E}{E_{sw}}} \quad (3.2)$$

Using the general formulation for the total potential in the inner magnetosphere (equation 1.9)

$$\psi = \frac{-\omega B_0 R_E^2}{L} + E_{sw} L R_E \sin\phi \quad (3.3)$$

and substituting in equation 3.2, and setting $\phi = \pi/2$ gives the potential of the dusk (1800 MLT) Alfvén layer

$$\psi_{AL} = 2\sqrt{\omega B_0 R_E^3 E_{sw}} \quad (3.4)$$

where the subscript AL refers to Alfvén layer quantities. When the Alfvén layer potential (equation 3.4) is substituted back into the total potential (equation 3.3) the Alfvén layer radial distance for a given azimuthal angle and convection electric field is given by

$$L_{AL} = \sqrt{\frac{\omega B_0 R_E}{E_{sw}}} \left[\frac{\sqrt{1 + \sin \phi} - 1}{\sin \phi} \right] \quad (3.5)$$

For a given value of the convection electric field, E_{sw} this yields the shape and size of the plasmasphere. Using the standard values of $3.1514 \times 10^{-5} \text{ T}$, $6.37121 \times 10^6 \text{ m}$, $7.27221 \times 10^{-5} \text{ rad/s}$ for B_0 , R_E , and ω respectively and solving 3.5 for E_{sw} gives:

$$E_{sw} = \frac{1.44 \times 10^{-2}}{L_{AL}^2} \left[\frac{\sqrt{1 + \sin \phi} - 1}{\sin \phi} \right]^2 \quad (3.6)$$

or in terms of MLT

$$E_{sw} = \frac{1.44 \times 10^{-2}}{L_{AL}^2} \left[\frac{\sqrt{1 + \sin \frac{(MLT-12)\pi}{12}} - 1}{\sin \frac{(MLT-12)\pi}{12}} \right]^2 \quad (3.7)$$

where where $MLT = \frac{12\phi}{\pi} + 12$.

Using equation 3.7 and the data from Table 3.1 the derived convection fields values are given in table 3.2.

Comparison With *in-situ* Data The previous sections have shown the Alfvén layer motion correlates with changes in parameters in the solar wind, and the local geomagnetic indices. Here we attempt to verify this relationship for the 8Apr2001 event, however, there are no suitably instrumented spacecraft in the proper orbit to directly measure the convection field. This makes validation of the derived convection electric field strength more difficult but also makes the ability to derive the convection electric field more important as

Table 3.2: Derived Convection electric field for 8Apr2001. The min and max are calculated from the inside and outside of the L region.

Time range	$\min(E_{sw})$ (mV/m)	$\max(E_{sw})$ (mV/m)
<10:59	<0.20	<0.28
10:59-11:07	0.40	0.62
11:07-11:27	0.40	0.62
11:27-11:36	0.28	0.40
11:36-12:31	0.21	0.28
12:31-13:46	0.22	0.30
13:46-13:56	0.41	0.64
13:56-14:25	0.41	0.64
14:25-14:37	0.28	0.40

an axillary data set. Validation can still be done in two alternate ways: by mapping low altitude *in-situ* polar cap potential values out to the convection field region, or by using a previously validated model of the polar cap potential driven by interplanetary inputs and then mapping that polar cap potential to the convection field region.

in-situ Polar Cap Potential The Special Sensor for Ions, Electrons, and Scintillation (SSIIES) instrument on the Defense Meteorological Satellite Program (DMSP) satellites provides the first method for deriving the convection electric field strength (*Cornelius and Mazzella, 1994*). DMSP satellites are a series of low altitude (840km) sun-synchronous polar orbiting satellites each measuring specific local time sectors. While the DMSP satellites carry no direct electric field instruments the field is derived using the measured cross track ion drift under the frozen in flux assumption. Using knowledge of the Earth's magnetic field, the electric field is derived from the particle motion using $\mathbf{E} = -(\mathbf{v} \times \mathbf{B})$. By integration over the field the potential at each point along the spacecraft track is obtained. The total polar cap potential is the difference between the highest and lowest potential measured by the spacecraft. These calculations are performed in the William B. Hanson Center for Space Sciences at the University of Texas, Dallas (UTD) and delivered to the

community via their website.

The different orbits of the various DMSP satellites favor the F13 spacecraft for this measurement as its 05:45-17:45 MLT orbit has the highest probability of intersecting the true maximum and minimum of the polar cap potential. Figure 3.6 shows a standard polar cap potential two-cell pattern (Weimer, 2001), overlaid with the DMSP F13 and F15 orbital tracks. F13 is the closer of the two to the location of the potential maximum and minimum values. Since one can't be sure that a satellite actually passes through the maximum and minimum potential regions the polar cap potential as derived by DMSP must be considered as a lower limit of the true value.

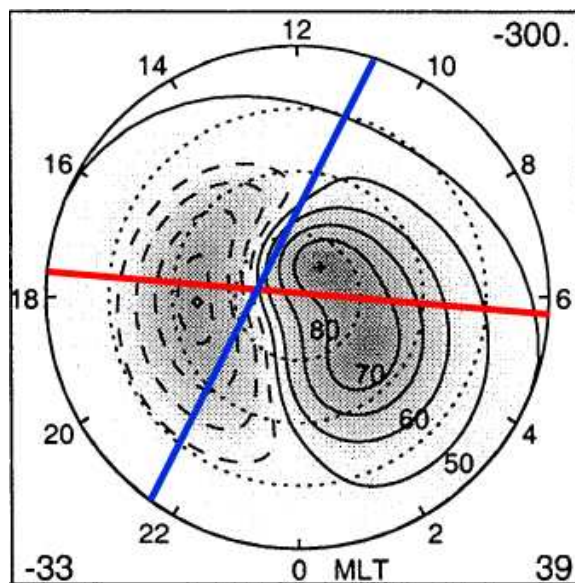


Figure 3.6: Standard two-cell polar cap potential overlaid with schematic DMSP passes for two satellites F13 (red) and F15 (blue). (Image courtesy Center for Space Sciences, University of Texas, Dallas)

The DMSP polar cap crossing beginning at 8Apr2001 07:52 UT, shown in Figure 3.7, derives a maximum potential of 38.57 kV and a minimum potential of -36.84 kV noting an offset potential of -2.87 kV. Physically, the potential is zero on both sides of the two-cell convection pattern, however integrating along the flight path rarely yields zero. The offset

potential is the difference between the end value and the correct value of zero¹.

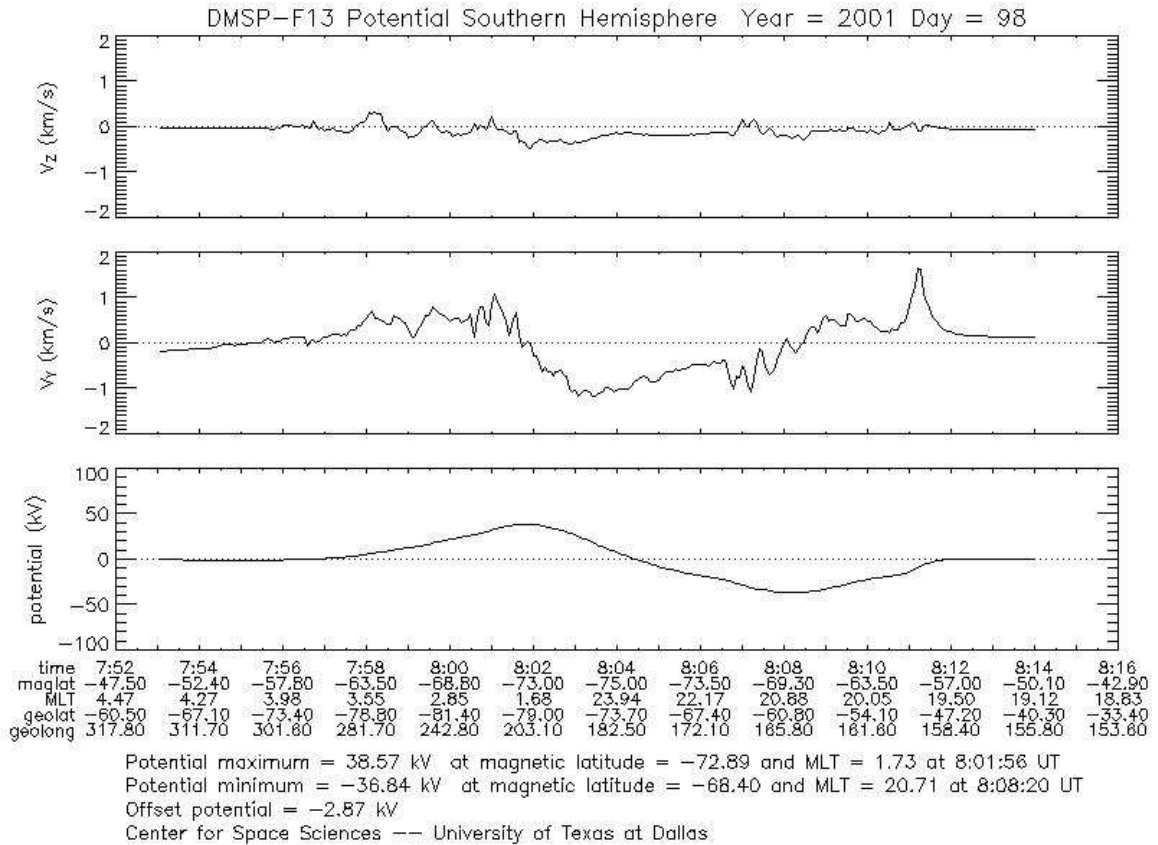


Figure 3.7: DMSP F13 polar cap plots showing the southern hemisphere polar cap pass beginning 8Apr2001 7:52. Shown are the measured cross path ion drifts and the derived potential from these measurements given in the GSM coordinate system. (Plot courtesy Center for Space Sciences, University of Texas, Dallas)

Mapping the polar cap potential into the magnetotail provides the calculation of the convection electric field across the magnetosphere. It is assumed that there is no potential drop along the field lines and the magnetotail is a cylinder of radius $40R_E$ (Lyons and Williams, 1984). The latter assumption is justified as the greatest interest in this data is the time evolution of the convection field, not necessarily the absolute value of the polar cap potential. The true tail width is at worst only slightly different for each measurement. As-

¹The UTD frequently asked questions accompanying the derived polar cap potential data, suggests that there is high confidence in the data if the offset value is less than 25% of the polar cap potential value.

suming that the convection field is purely dawn-dusk, the convection field is $E_{sw} = -\nabla\phi_{pc}$ which then reduces to $E_{sw} = \phi_{pc}/(2 \cdot 40R_E)$. There are only six polar cap passes of DMSP F13 during the 8Apr2001 time period that yield high confidence polar cap potential values. The polar cap potential and convection electric field derived for each of these passes are shown in Figure 3.8. These data are too sparse to be used as a validation of the EUV derived convection field strength, although there is clearly an increase in the convection associated with this event. The rise begins between 10:00 UT and 12:00 UT and is maximum around 14:00 UT for the second inward Alfvén layer motion. This DMSP discussion is presented as an order of magnitude validation and as a method that could be used for other events containing more complete DMSP coverage.

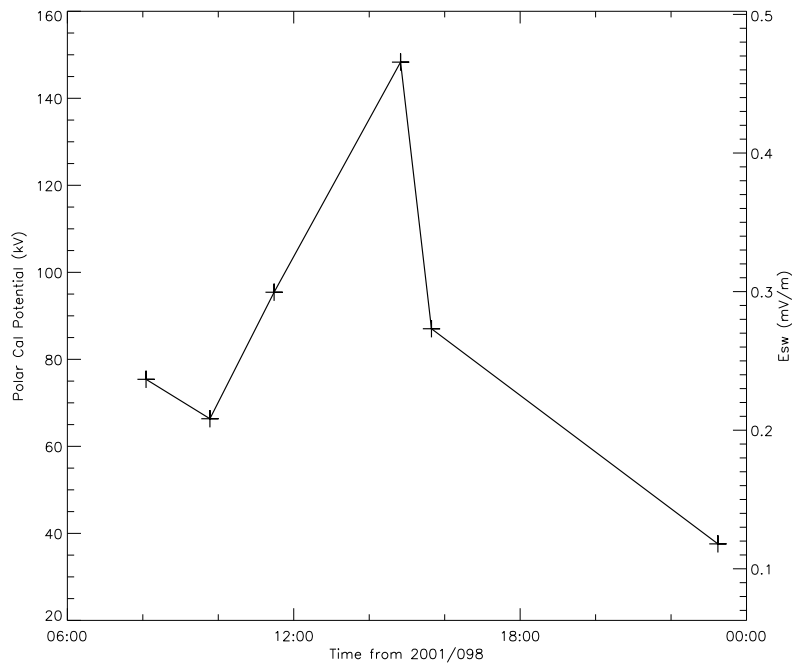


Figure 3.8: Derived convection electric field from the six DMSP-F13 high confidence passes on 8Apr2001.

Comparison To Polar Cap Potential Model An empirical method of estimating the polar cap potential has been described by *Weimer* (2001). This is a solar wind based relationship given by:

$$\phi_{pc} = 25.5 + 7.2B^{0.6}V \sin^2(\theta/2) \quad (3.8)$$

where B is the magnitude of the IMF, V is the solar wind velocity, and θ is the IMF clock angle from *Sonnerup* (1974). At L1 the ACE data has to be time delayed to its arrival at Earth before equation 3.8 is valid. Equation 3.8 is found to account for 98% of the observed variation of the polar cap potential over a range of ϕ_{pc} from 20 – 100kV based on measurements from the DE-2, IMP-8, and ISEE-3 satellites (*Weimer*, 2001). This method of validation has the advantage of being based on the nearly continuous measurements of the required solar wind parameters and IMF from the ACE spacecraft. The ACE data is binned into 10 minute bins to match that of the EUV images, each bin is then time delayed to arrival at Earth using the average earthward component of the solar wind velocity. Using the binned and delayed data together with equation 3.8 the convection electric field shown in Figure 3.9 is obtained. Figure 3.9 shows two peaks in the convection electric field at about 11:00 and 14:00 corresponding well with the derived motion of the Alfvén layer. Overplotted with a dashed line are the minimum and maximum values of the EUV derived convection electric field strength from Table 3.2. The alignment of the peaks is very good showing the validity of the technique of deriving the convection electric field from observed motion of the Alfvén layer.

Results

Mapping polar cap potential values for the 8Apr2001 event from both DMSP and the *Weimer* (2001) model to the magnetotail compare well with the convection electric field

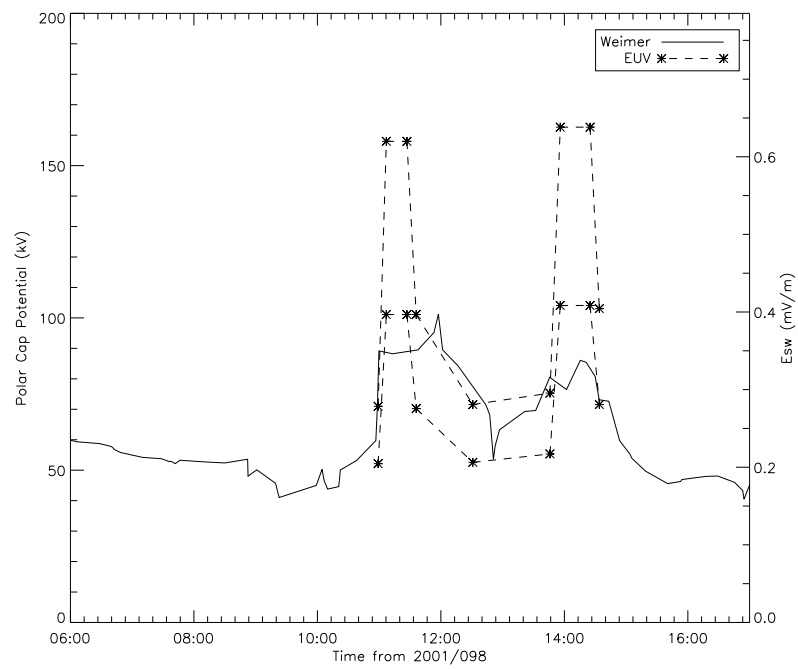


Figure 3.9: Derived convection electric field (right ordinate) and polar cap potential (left ordinate) using the *Weimer* (2001) polar cap potential model for 8Apr2001 plotted in solid. The dashed line is the EUV derived convection electric field.

strength derived from observation of the motion of the Alfvén layer. This result observationally verifies the overarching theory of plasmasphere dynamics as being driven by the overlap of the convection and cross-tail electric fields. This provides a mechanism to derive electric fields not currently directly measured.

The convection electric field values derived through observations of motion of the Alfvén layer are larger than the *Weimer* (2001) derived values, this is not entirely unexpected. This event is reaching the limit of the validity of the *Weimer* (2001) model. Events where the Alfvén layer can be tracked are rare making this event something special. Other events cannot be tracked because of a lack of features to track or a convection field strength too small to make for obvious stagnations. One possibility as to why this event can be tracked is that inner magnetosphere shielding was setup prior to the event in a way that allowed the penetration of the convection fields to be very efficient, giving the illusion of a stronger convection field (*Jaggi and Wolk, 1973*). Another possibility is the addition of other effects such as sub-auroral polarization streams (SAPS) (*Foster and Burke, 2002*) which serve to enhance the convection field in a narrow region of MLT in the dusk region. This SAPS electric field is the result of a separation between the electron and proton plasmashet, causing a current closing in the night side ionosphere which sets up a large electric field due to low conductivity. These SAPS fields have already been shown to affect the plasmasphere by *Goldstein et al. (2003a)* who find that the addition of a simple SAPS field tightens features in the dusk plasmasphere into a long channel between the plasmasphere proper and a highly wrapped tail, that type of effect could also help describe the density depletion that was tracked in this study.

EUV Derived Convection Field for 17 April 2001

Another identified event where the convection electric field can be derived from the

EUV images occurs 17-18Apr2001. It starts with a medium sized plasmasphere formed during a slightly elevated polar cap potential that has been largely steady for about 48 hours (see Figure 3.10). This is followed by a large ($Dst < -100$ nT) storm that results in a severe plasmaspheric erosion. Using EUV data it is possible to derive the convection field strength for the beginning of the storm which is a time period where there are no satellites directly measuring the convection field.

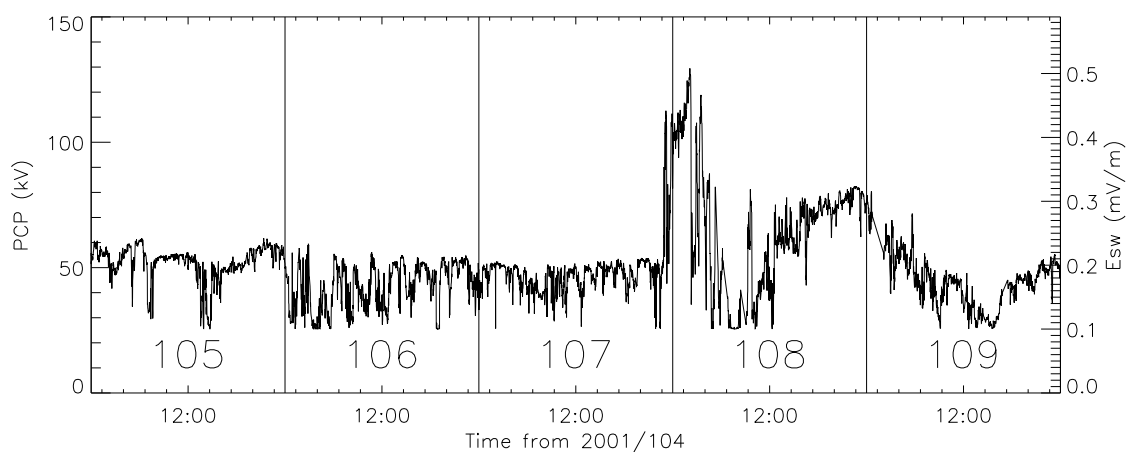


Figure 3.10: Running plots of the *Weimer* (2001) derived polar cap potential from 15Apr2001 through 19Apr2001. The vertical lines in the plots separate days, the large numbers indicate the day of year for each day. The right hand ordinate is the convection electric field derived by mapping the polar cap potential out to a magnetotail of diameter $40R_E$.

Data

The steady polar cap potential conditions are, not surprisingly, mirrored in the *Dst* and *Kp* indices for this period. A sudden commencement is then reported in the NOAA Solar Geophysical Data records at 18Apr2001 00:45 UT (day 108) where a large storm begins, and the characteristic the rise and fall in the *Dst* index and the rise in *Kp* (Figure 3.11). These magnetospheric indices are shown to add the global context to the event.

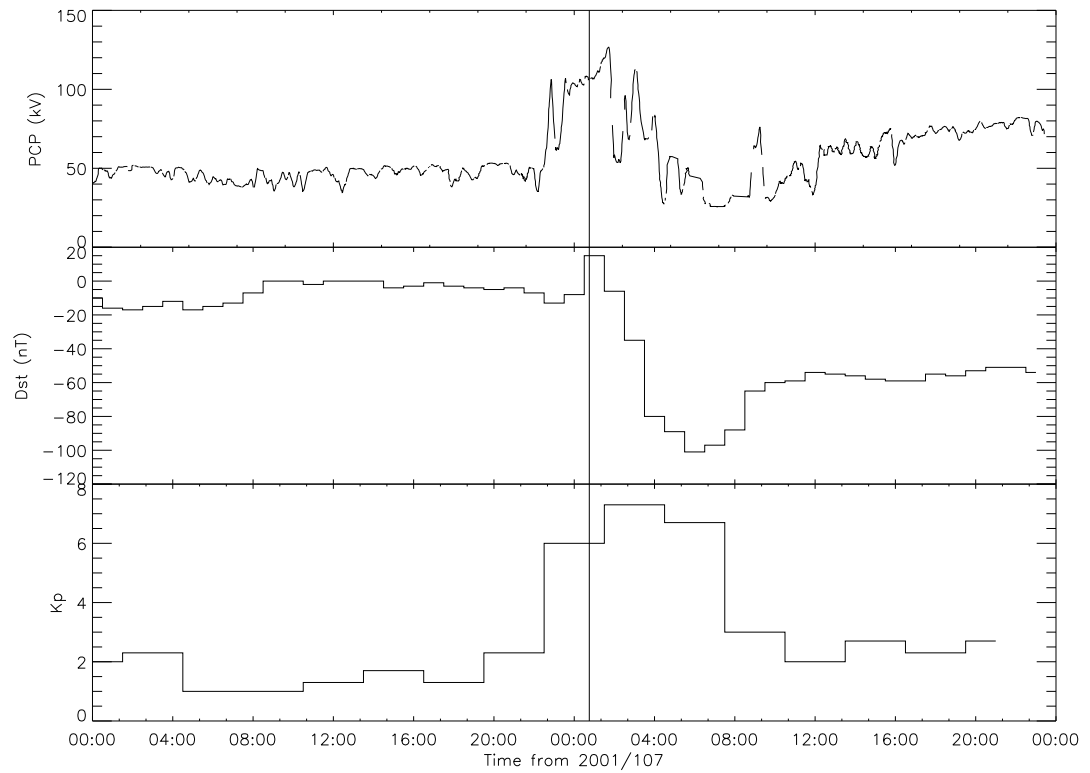


Figure 3.11: Dst and Kp indices for the 17Apr2001 period. The vertical line at 18Apr2001 00:45 UT corresponds to the occurrence of a sudden commencement.

The interplanetary data in Figure 3.12 shows a shock arrival at ACE occurring at 00:00 UT highlighted by the vertical line. Jumps in both the number density (N_p) and velocity (V_p) correspond to the sudden commencement at 00:45 UT after its arrival at Earth. There is also a significant southward IMF turning, followed by a consistently southward IMF, thus increasing the geoeffectiveness of the event.

The two-day-long steady magnetospheric conditions leading up to this event allow the plasmasphere to refill to beyond $4R_E$. However, there are unexplained, significant small scale variations creating a very irregular plasmopause. This irregular boundary provides features to track in the stackplots thus allowing for EUV derived electric fields to be computed (Figure 3.13).

There are two common occurrences in the EUV data illustrated in Figure 3.13. The first is the sensor head cutout in the 2001 107 23:48:49 image (middle top of second panel) this occurs whenever the head field of view contains the sun. In this case the shutdown includes the dusk sector of the plasmasphere. The final image at 2001 108 01:00:22 demonstrates the EUV response to energetic particle penetration. The instrument becomes saturated, which raises the noise threshold as observed in the left and center thirds of the image, and total saturation occurs in the right third. In this instance the noise is probably the arrival of solar protons associated with the sudden commencement. The images remain noisy and of poor quality for the rest of this event as is evident in the stackplots (Figure 3.14). This rise in the noise level and saturation is a feature that cannot be overcome in the study of EUV images during times of high energetic particle fluxes. The increased noise creates hot-spots in the inverted images, as explained in Chapter 2, resulting in poor inversion integrity and quality. The sensor head cutout causes few problems for the inversion process as a two head image is a valid, albeit odd, plasmasphere image.

Creating UT-MLT stackplots from all available images during this period reveals an obvious feature to track in the dusk sector. Figure 3.14 shows stackplots from the 2 – 2.5,

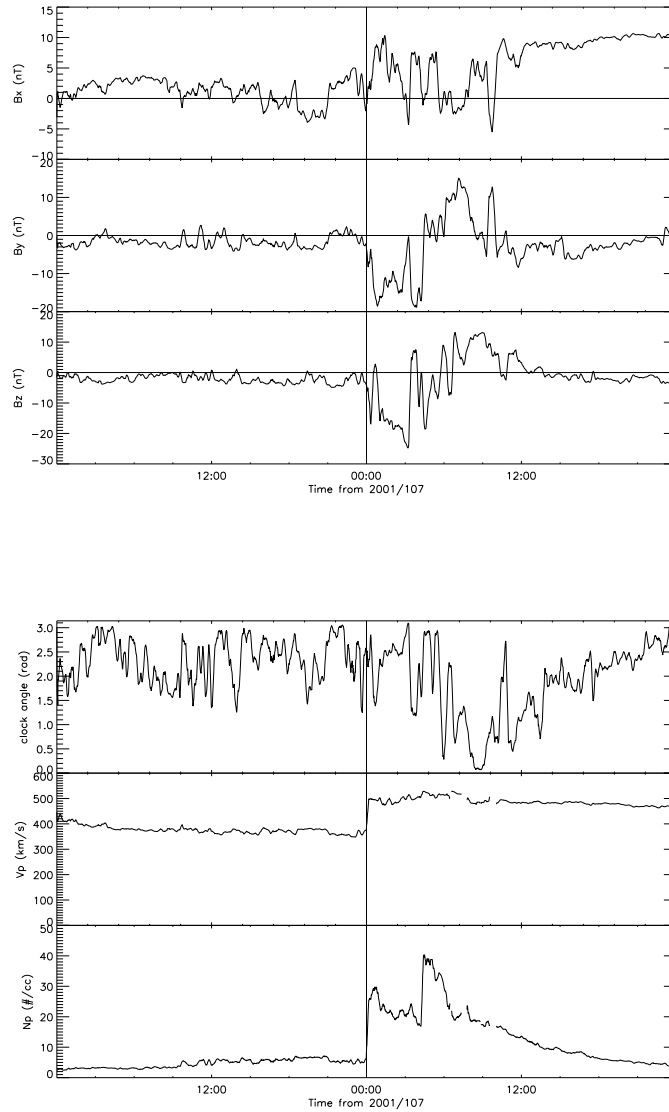


Figure 3.12: Interplanetary data from ACE for 17Apr2001-18Apr2001. (top) IMF x, y, z components (bottom) IMF clock angle, Proton velocity (V_p), and number density (N_p). The vertical line at 18Apr2001 00:00 UT corresponds to the interplanetary shock passing the ACE spacecraft. Note the ACE data is not time delayed to Earth, the delay is about 40 minutes at these solar wind speeds.

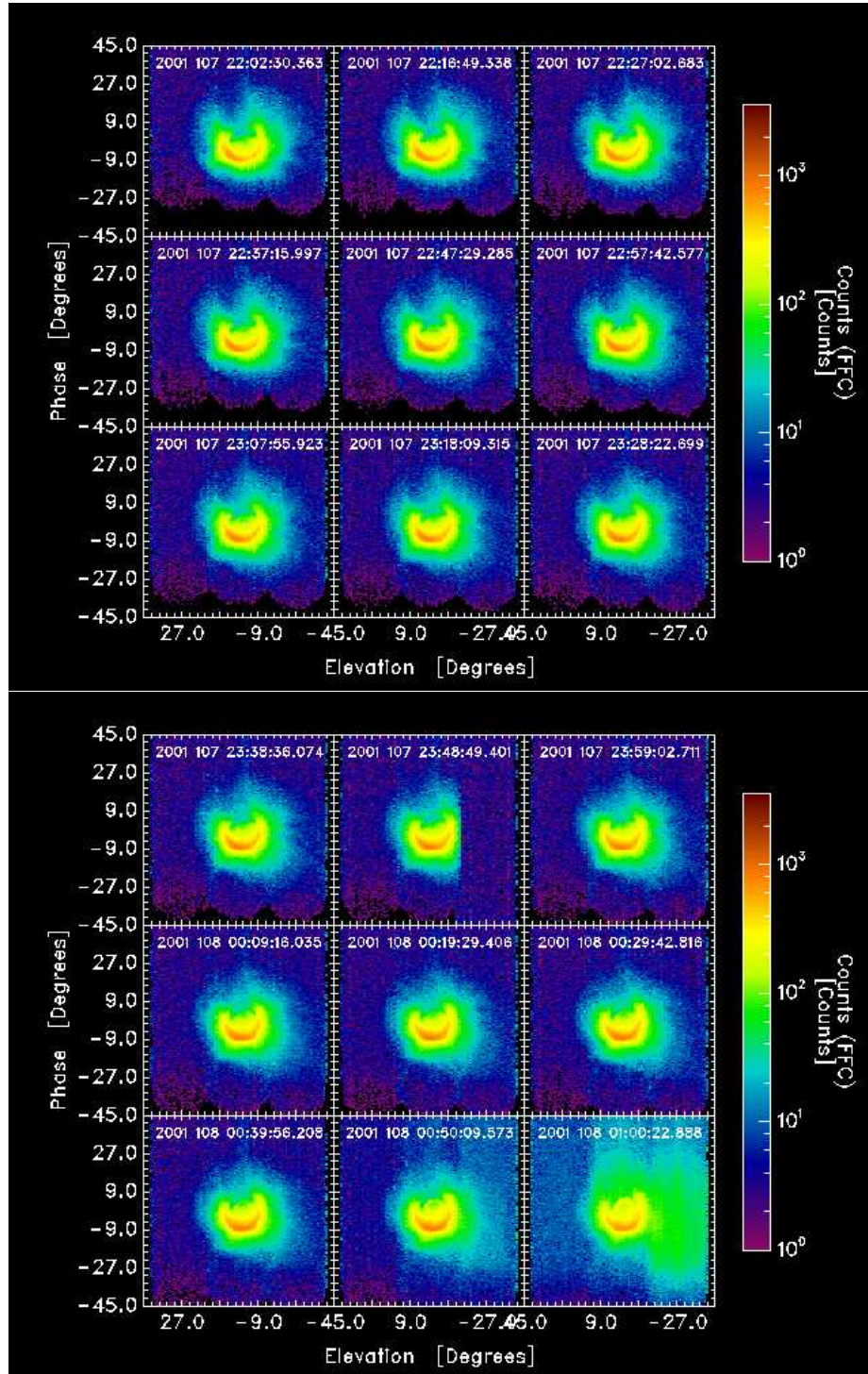


Figure 3.13: Time series of EUV images during the Alfvén layer motion centered at 17Apr2001 22:47:29 UT. The sun is almost straight down and each image is 10minutes apart.

2.5 – 3, and 3 – 3.5 R_E annuli. The identified transitions from open to closed drift paths (stagnations) with each stackplot are marked by the red crosses. In tracking a stagnation, it is important to look for *small scale* changes in slope. The feature over the course of the stackplot remains close to the corotation reference line, the stagnation points are identified as slope changes in the feature. Beginning with the 3 – 3.5 R_E annulus, the stagnations are most obvious. Moving inward, the stagnations are present but less obvious. An automated selection process to eliminate subjectivity in the selection of points is certainly desirable, but due the scarcity of stagnation events identifiable by eye, the ability to develop an algorithm seems an extremely difficult and probably fruitless endeavor, with the current data set.

Results

Using the stagnation points from Figure 3.14 and Equation 3.7 the electric field is derived and shown in Figure 3.15 plotted over the *Weimer* (2001) derived polar cap potential. The convection field strength is derived by mapping the polar cap potential to a cylindrical magnetotail of radius 40 R_E . The fit between the EUV derived convection field and the *Weimer* (2001) derived field is excellent for the first peak centered at 22:45UT and the following valley, the EUV data quality, however, degrades rapidly after that not allowing for the extraction of any further stagnation points for this event.

Event Comparison

Comparison of the 8Apr2001 and 17Apr2001 events shows a fundamental difference in the fit between the EUV and *Weimer* (2001) derived convection electric field. While the 8Apr2001 values are consistently higher than the the 17Apr2001 values are within error bars of being correct. There is a fundamental difference in the events driving the

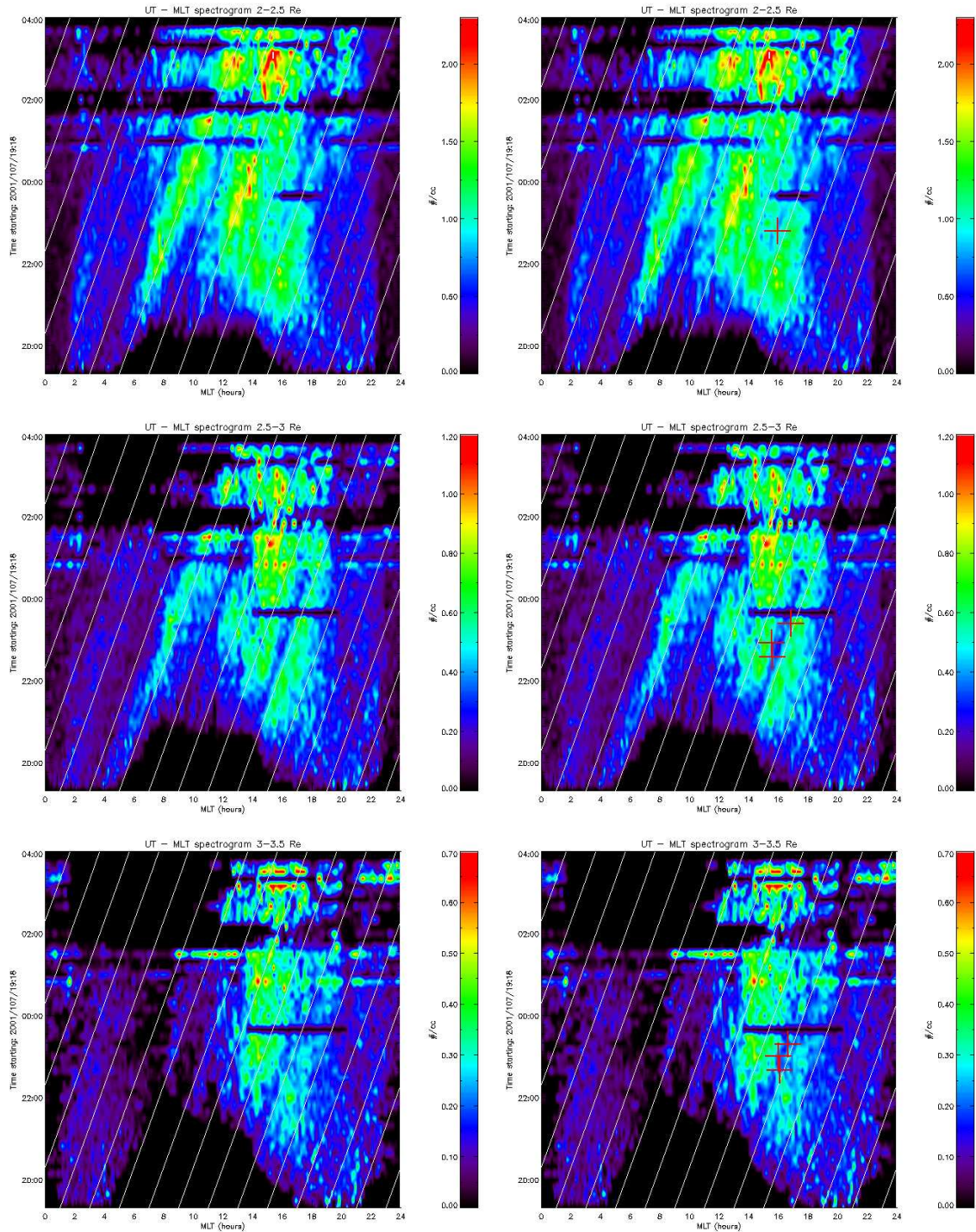


Figure 3.14: (Left) UT-MLT stackplots from 17Apr2001 showing the 2 – 2.5, 2.5 – 3, 3 – 3.5 R_E annuli from top to bottom. (Right) Identical stackplot with the extracted stagnation transition points marked with red crosses. Note in all plots the colorbar is *linear*.

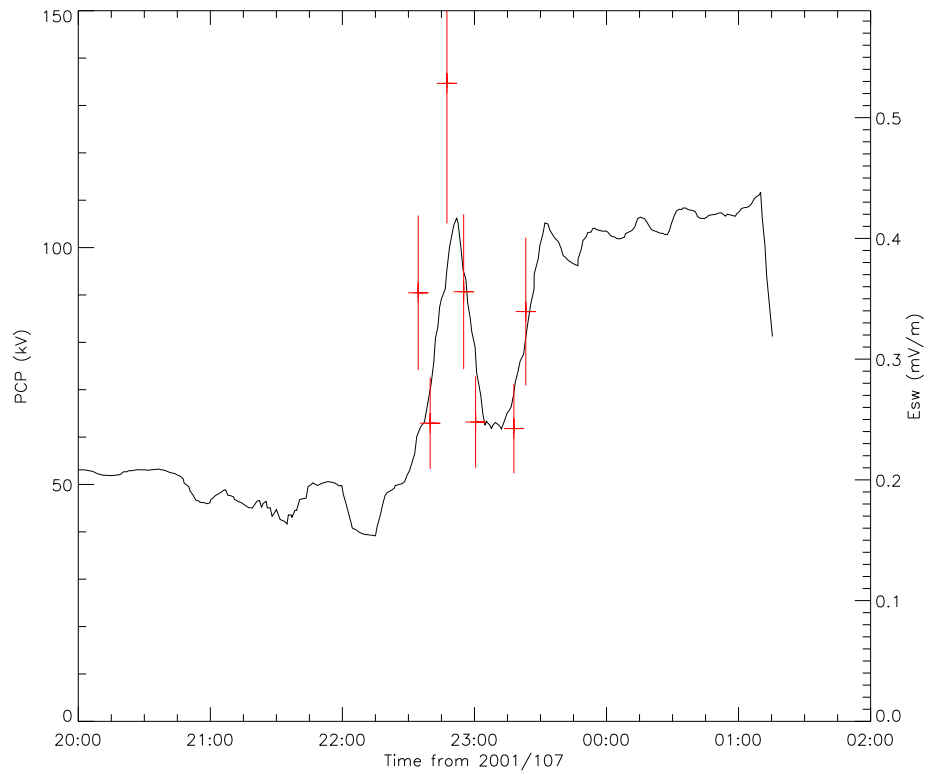


Figure 3.15: *Weimer* (2001) derived polar cap potential (PCP) for 17Apr2001 with the EUV derived electric field (Esw) calculated from the stagnation points in Figure 3.14. The error bar shows the maximum and minimum values from the $0.5 R_E$ radial range of each annulus.

discrepancy. The 8Apr2001 event is a small geomagnetic storm ($Dst > -60\text{ nT}$) versus a large storm ($Dst > -100\text{ nT}$) which implies mainly a ring current difference between the events. The consistently southward IMF in the 17Apr2001 event certainly increases the geoeffectiveness of the event, making the storm large while leaving the *Weimer* (2001) derived polar cap potential about the same. Given the similarities in the *Weimer* (2001) derived polar cap potential and the differences in the EUV derived convection field strength for these events the event has either reached the limits of the *Weimer* (2001) model as it incorporates no saturation of the polar cap potential (*Shepherd*, 2007) or we have neglected the presence of other electric fields such as SAPS in the 8Apr2001 event. While there are still too few events studied to draw any strong conclusions, this work does strongly suggest that significant information is available from the convection electric field derived from observations of the motion of the Alfvén layer.

Discussion

The ability to derive the convection electric field strength provides a key piece of data when it comes to understanding the magnetospheric storm time dynamics. This technique is useful for deriving the overall strength of the convection electric field from a series of inverted EUV images of the plasmasphere providing a backdrop for understanding of other *in-situ* data. While beyond the scope of this work, side-by-side comparisons to global convection models (*Toffoletto et al.*, 2003; *De Zeeuw et al.*, 2004) would provide interesting insights into the coupling between the open field line magnetotail and the largely dipolar plasmaspheric region of the inner magnetosphere that have been largely observationally unexplored.

Global imaging has certainly demonstrated its usefulness and its role in advancing our understanding of the dynamics of large scale systems as have single *in-situ* measurements,

and multi-spacecraft missions such as CLUSTER. Each has a unique role to play and each supports the other to provide a richer picture of the underlying physics. The December 2005 failure of the IMAGE spacecraft has however left a hole in the overall data coverage. The promise of obtaining global electric field values is one of the major accomplishments of this work, future studies and instruments should help this technique mature to the point where imagers can provide the kinds of data that until now has been the sole realm of the *in-situ* measurements. The ability to obtain a global map of electric fields from a series of images from a single spacecraft is more cost effective and adds value to any mission in addition to any detailed studies performed using the images. The next chapter will explore the state of global magnetospheric imaging, the issues associated with the current data, and provide suggestions for future improvements to the current EUV imaging.

CHAPTER 4

PLASMASPHERE DERIVED ELECTRIC FIELDS:
CURRENT LIMITATIONS AND FUTURE POSSIBILITIES

The previous chapter demonstrates a method to use plasmaspheric images to derive the convection electric field strength. This chapter will highlight areas where improvements can be made with current data, areas where improvements can be made with instrumentation, and areas that are not possible or practical to improve.

Introduction

From the convective plasmasphere model of plasmopause formation, tracking of the boundary between closed and open drift paths should be possible whenever electric field changes occur more rapidly than the plasma can react. Why then is this technique hard to use in practice, and what improvements are necessary to make this a more reliable technique? Presented here will be a description of the experiential requirements for this technique to yield valid results, why this technique does not work for all events, and a brief mission concept based around the EUV convection electric field measurement.

In order for the technique to be useful as a long term diagnostic tool for the electric field structure in the inner magnetosphere it must be possible to determine the convection field strength for most geomagnetic events and preferably to be able to derive separate localized structures of the electric field, such as differentiating between the Sub-Auroral Polarization Stream (SAPS) field (*Foster and Burke, 2002; Goldstein et al., 2003a*) as described in the previous chapter, from the overall crosstail convection field.

EUV Derived Convection Field Limitations and Possibilities

Based on observations described in Chapter 3, it would seem easy to identify other examples where global plasmaspheric images can be used to derive the convection field strength. However, since the technique relies on the identification of stagnation points in the temporal evolution of plasmaspheric density features there are several associated caveats. It is trivial to identify time periods using the *Weimer* (2001) derived polar cap potential where it should be possible to derive the convection electric field from the EUV data, as all that is required is a large change in the convection electric field as parametrized by the polar cap potential. However there are other necessary conditions. Figure 4.1 shows 25 days of running polar cap potential beginning 11Apr2001 (day 101). Each day's polar cap potential are separated by vertical lines and the large number below the curve in each block is the day of year. The ability to use the *Weimer* (2001) model is dependent upon the availability of ACE solar wind data. While deriving the convection electric field from plasmaspheric EUV images does not require any external data.

EUV Derived Convection Field Requirements

Based on experience, events where the convection field can be derived from EUV data have the following requirements: 1) unless the value of the polar cap potential reaches about 60kV, no signature has been observed; 2) physical arguments require that the plasmasphere be large enough for the Alfvén layer motion to be within the plasmasphere; 3) there must be high quality EUV data; 4) there must be a feature to track within the plasmasphere.

60kV Polar Cap Potential The requirement for the 60kV polar cap potential can be understood in terms of the potential required to observe the Alfvén layer crossing a certain *L*-shell. Figure 4.2 shows plots of Equation 3.7 at varying values of MLT. These plots

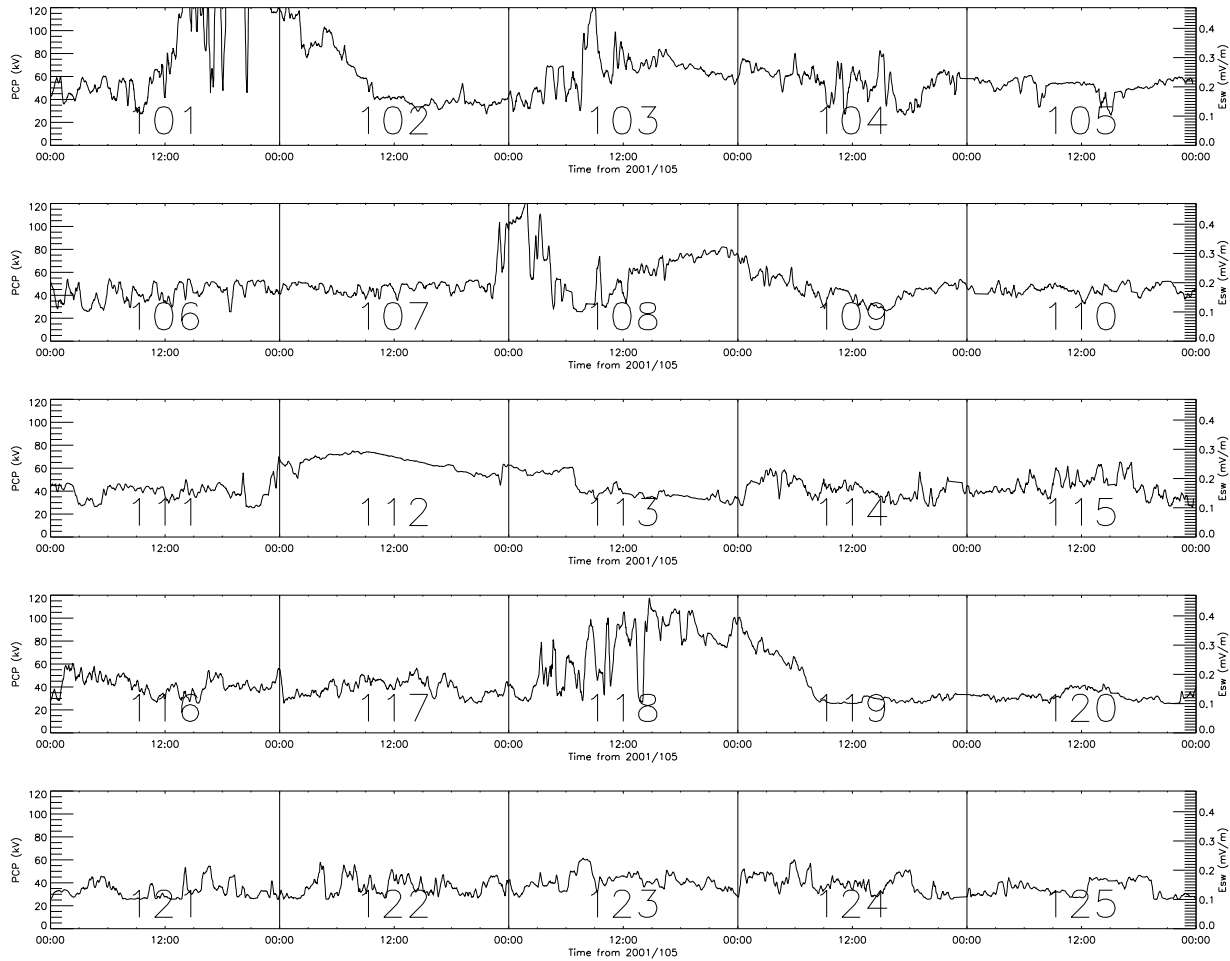


Figure 4.1: Running plot of the *Weimer* (2001) derived polar cap potential from 11 April 2001 through 5 May 2001. The vertical lines separate days, the large numbers indicate the day of year for each day. The right hand ordinate is the convection electric field derived by mapping the polar cap potential out to a magnetotail of diameter $40R_E$. The mapping method from *Lyons and Williams* (1984).

demonstrate the relationship between the L -shell where the Alfvén layer crossing is observed and the minimum polar cap potential required to move the Alfvén layer into that L -shell. The shape of the curves in Figure 4.2 are such that a small change in polar cap potential can easily be seen over a wide range of large L values. This is especially true in the evening sector.

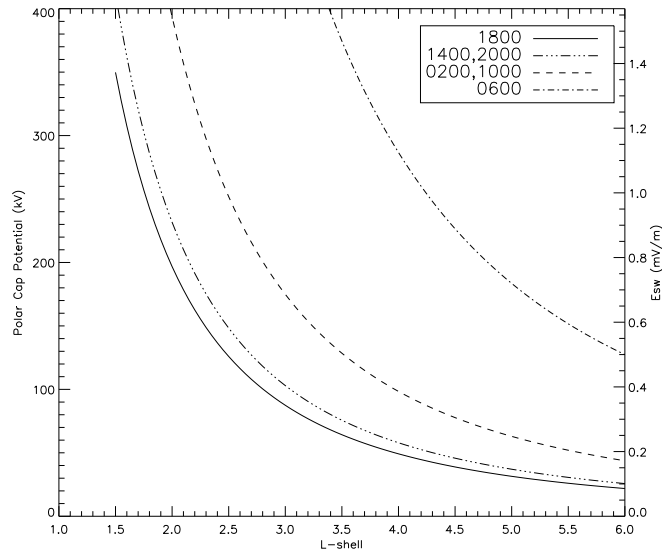


Figure 4.2: Relationship between L -value of observed Alfvén layer crossings and the required polar cap potential for different values of MLT. In this model the Alfvén layer is symmetric yielding the dual MLT valued curves in the plot.

In order to observe the smaller convection electric field values the inverted data would need to have a significantly higher resolution so that stackplots could be made with annuli bins significantly smaller than the current $0.5R_E$. Smaller bins would enable a change from 40 to 60kV to be resolved as the Alfvén layer crosses from 4.4 to $3.6R_E$ as a change of more than one bin. The range of polar cap potential values for a $4 - 4.5R_E$ bin and a $3.5 - 4R_E$ bin are 10kV and 15kV respectively as found from equation 3.7. The derived values are indistinguishable from one another due to the large range. In order to raise the

resolution of the inverted data, the EUV images could either have higher resolution or the inversion could be improved to yield smaller bins. Improvements to the inversion cannot go beyond the fundamental spatial resolution of the original images, $0.1 R_E$, as averaging data together in the creation of stackplots is crucial to making them stable and understandable. The best solution would be to image with higher resolution.

Large Plasmasphere Typical values of the cross polar cap potential range between 20 and 60 kV (Weimer, 1995). These typical values require the observation of the Alfvén layer between 4.4 and $6.5 R_E$ in the dusk sector. Since the Alfvén layer must be interior to the plasmopause to make the measurement, this sets the plasmasphere size threshold. Using the statistical plasmopause data from Larsen *et al.* (2007) the EUV extracted plasmopause is found to be larger than $4.5 R_E$ only 30% of the time. Slow refilling rates require that the inner magnetosphere must be quiet for extended periods to refill to distances beyond $4.5 R_E$ (Rasmussen *et al.*, 1993). Observing features when the polar cap potential is 100 kV corresponds to an Alfvén layer crossing of $3.5 R_E$ which can be observed 76% of the time. Both percentages are derived from the plasmopause L -value histogram shown in Figure 4.3.

There is no way to remove the large plasmopause condition for a given event, the plasmasphere is where it is. One improvement would be temporal coverage of the plasmasphere removing the probability of observing a storm onset and subsequent erosion due to “no data.” The easier way to accomplish this is with a multi-spacecraft mission which has the additional advantage of allowing tomographic inversions of the images.

High Quality EUV Data In addition to having satellites in positions to give near continual coverage, the experiment itself must be capable of continuous or near continuous operation. Figure 4.4 displays five days of polar cap potential overplotted in grey with the

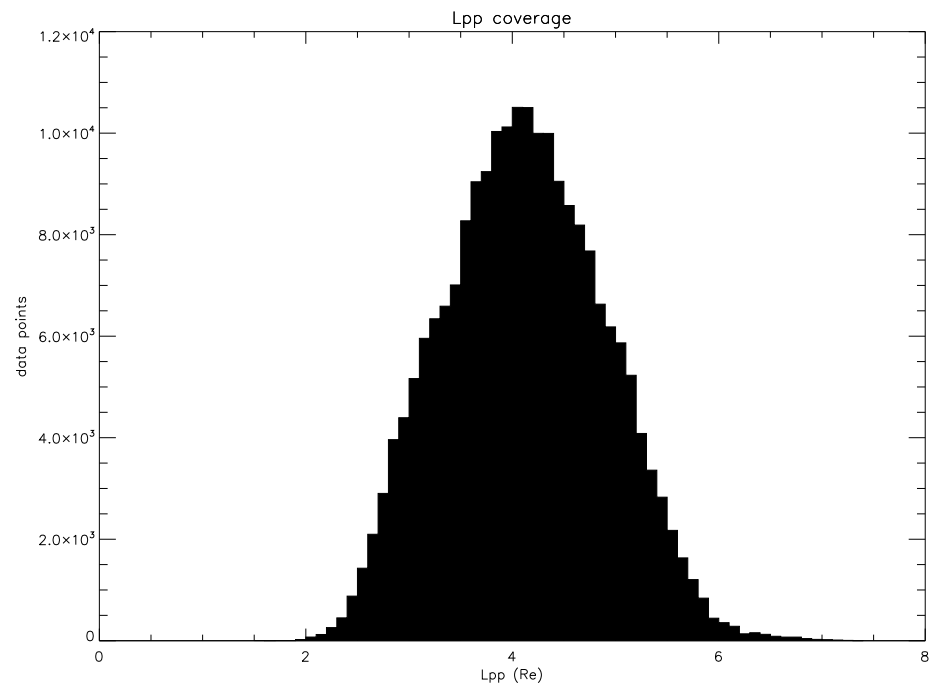


Figure 4.3: Plasmopause location histogram of the plasmopause points used in the statistical study of *Larsen et al.* (2007).

availability of EUV images, which is typical for most periods of similar orbital geometry. There are large time periods with data, but there are also large gaps in coverage.

Some of the gaps are due to satellite position, some are due to the sun being in the field of view, and others when the experiment is within high radiation environments. Even in the coverage periods, there will be sensor heads dropped because of sunlight contamination. Improvements in shielding from both radiation and sunlight will go a long way toward meeting a goal of continuous instrument operation. Operating from a despun platform rather than a spinning satellite will greatly improve time resolution and registration, both of which improve plasmaspheric studies.

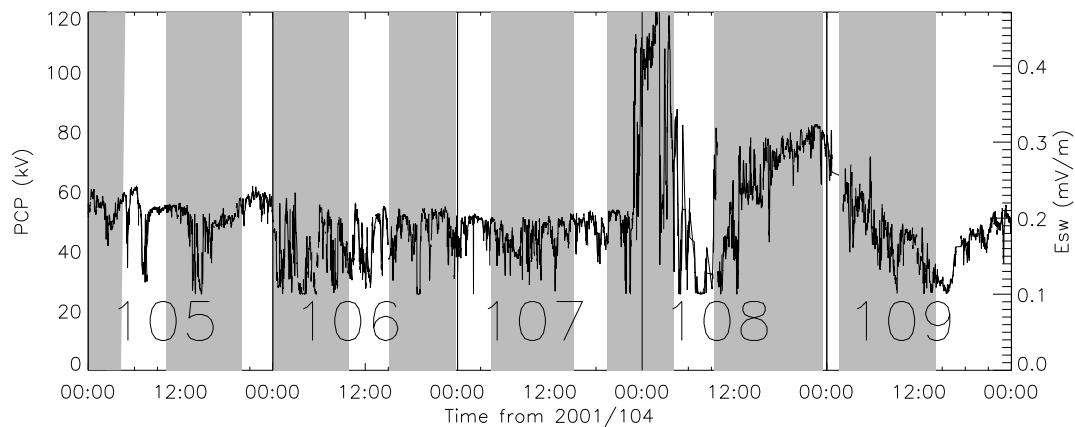


Figure 4.4: IMAGE-EUV data coverage for 15Apr2001 to 20Apr2001. The grey regions denote regions of high EUV data quality.

Feature To Track It is still unclear what creates the features that are tracked to derive the convection electric field. On some occasions the features are related to the wrapping of a plume around the plasmasphere as in the 8Apr2001 event. In others the features are related to plasmaspheric notches present in the image as with the 17Apr2001 event. The puzzling part of the features is how rarely there is a clear feature to track even when one would be expected from EUV images. Figure 4.5 presents two stackplots that illustrate the difficulty in tracking a feature. The left plot contains no distinct feature while the right plot contains a sharp boundary with a few broad slope changes but no ability to pinpoint the change in slope, making tracking difficult. These are both common occurrences in stackplots. The lack of features and lack of understanding of when there should be a feature highlights a shortcoming in the detailed understanding of small scale plasmaspheric features. These small scale features, especially deep within the plasmasphere, need more study and explanation. Are they the result of localized penetrating electric fields? Field aligned currents dumping plasmaspheric plasma into the ionosphere? Or something else entirely?

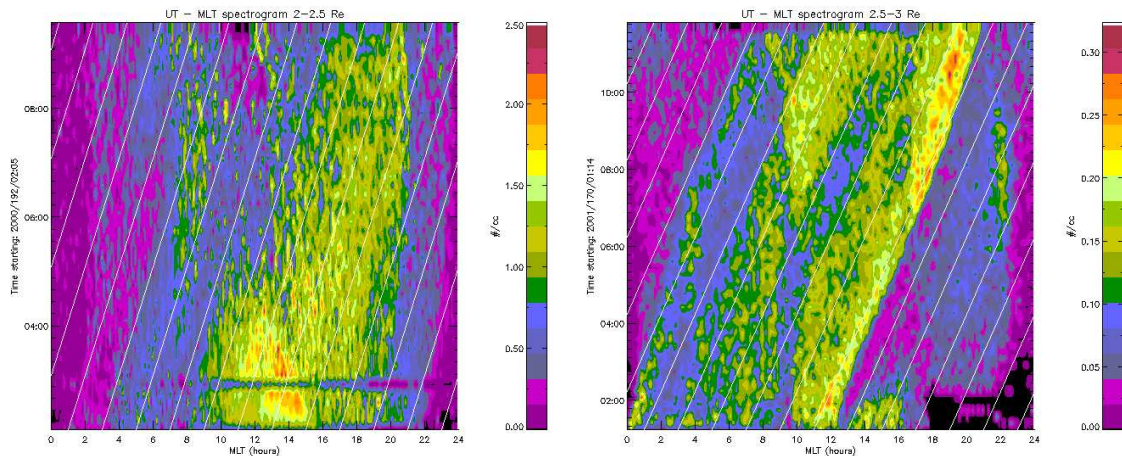


Figure 4.5: (left) UT-MLT stackplot for 10Jul2000 (day 192) 02:05-10:00UT for the annulus 2 – 2.5 R_E . (right) UT-MLT stackplot for 19Jun2001 (day 170) 01:14-12:00UT for the annulus 2.5 – 3 R_E .

Discussion

The results from the IMAGE mission have provided an intriguing first look into the utility of global magnetospheric imaging. The real challenge is to move beyond the qualitative imaging studies to the quantitative aspects of magnetospheric physics that can be derived from the global images. The ability to derive the convection electric field strength is one such ability. Being able to provide a context with which to understand other measurements is a very successful aspect of the IMAGE mission and could be significantly improved in future missions (*Borg et al.*, 2005; *Darrouzet et al.*, 2006).

Future Imaging Concept Mission

Briefly, this chapter provides a mission concept that is the next step in global magnetospheric imaging. The basic mission and EUV instrument requirements are found in Table 4.1. The basic premise is that multiple spacecraft imaging the plasmasphere at a < 10 minute time resolution in both 30.4 nm He^+ and 53.9 nm O^+ . These measurements allow tomographic reconstruction of the three-dimensional plasmasphere in both He^+ and O^+ . The O^+ component of the plasmasphere has not been studied in depth, providing the ability to compare densities and dynamics of the different ion species.

Table 4.1: Requirements of a future plasmaspheric EUV imaging mission.

Property	Value
Time resolution	$< 10\text{ min}$
Near continual viewing	ability to image from any apogee latitude
Multiple spacecraft	≥ 2 spacecraft
Field of view	$\geq 6R_E \times 6R_E$ from apogee
Spatial resolution	$\leq 0.01 R_E$ from apogee
Sensitivity	image less than $30\text{ He}^+ \text{ cm}^{-3}$
Spacecraft attitude	despun platform
Sun shielding	$\pm 3^\circ$
Particle shielding	ability to operate into $L \sim 4$

CHAPTER 5

PLASMASPHERIC COROTATION - IONOSPHERIC SIGNATURE

Introduction

Previous chapters have dealt with the reaction of the plasmopause to external influences, such as the convection electric field. This chapter will examine the influence of the underlying ionosphere on the plasmasphere. In a convective plasmasphere model as used in previous chapters all plasmaspheric dynamics are driven from external fields. In a more complete treatment of the full system there are also possible effects from beneath the plasmasphere. These ionospheric effects are currently not well understood but contain interesting implications for the dynamics of the system as a whole.

The question asked here is how corotation in the plasmasphere is affected by the ionosphere. The ionosphere is the uppermost region of the atmosphere. The ionosphere and magnetosphere are typically studied independently of one another. This is based on the fundamental differences in measurement techniques, the plasma environment, and driving factors. The ionosphere is created by photoionization and impact ionization of the neutral upper atmosphere. It extends from ~ 50 to ~ 400 km although there is no distinct boundary between the upper ionosphere and the lower plasmasphere. Typical electron densities in the ionosphere range from 10^4 to 10^7 cm^{-3} making it a collisional plasma (*Goel et al.*, 1976). Two major differences between the dynamics of the plasmasphere and ionosphere are the collisional nature of the ionosphere and the neutral wind motions affect on the ionosphere.

One study of the connection of ionospheric phenomenon to the plasmasphere is the study by *Burch et al.* (2004). They take the approach that plasmaspheric sub-corotation is

caused by the ionospheric disturbance dynamo (explained in next section). They argue that when the disturbance dynamo is active it causes a subcorotation of the ionosphere. If the plasmasphere is rigidly connected to the ionosphere, then the plasmasphere must also show this subcorotation during these periods. This chapter looks at those results with the added information of inverted EUV images and UT-MLT stackplots.

Ionospheric Disturbance Dynamo

The ionospheric disturbance dynamo is a corotation lag caused by ionospheric Joule heating in the auroral zone caused by an increase in ionospheric currents. During times of increased Joule heating the ionosphere expands, and shifts southward driven by neutral winds. The Coriolis force (or equivalently conservation of angular momentum) cause a westward drift of the moving ionospheric plasma which results in a subcorotation (see *Blanc and Richmond (1980); Buonsanto (1999)* and references therein).

Sub-corotating Plasmaspheric Event (8Apr2001)

The time period studied by *Burch et al. (2004)* is the 8Apr2001 period presented in Chapter 3 of this dissertation. To put the event in context, Figure 5.1 is a time series of images beginning 8Apr2001 10:03:13UT showing the presence of a large plasmaspheric shoulder on the right side of each image. These shoulders have been studied previously by *Goldstein et al. (2002a)* who find them to be the result of overshielding. To briefly restate the description in Chapter 1, overshielding is a process wherein the inner-magnetosphere shielding from the convection field is too large due to a sudden decrease in the convection field strength. Overshielding then results in a net dawnward electric field (opposite the convection field) causing plasma to convect anti-sunward, thus forming a shoulder in the plasmasphere when the overshielding subsides.

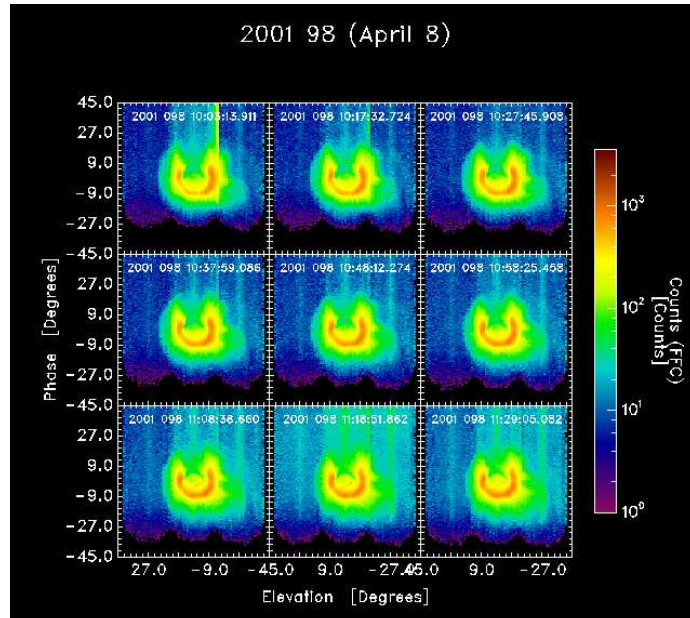


Figure 5.1: IMAGE-EUV time series from 8Apr2001 10:03UT to 8Apr2001 11:29UT showing the rotation of a large plasmaspheric shoulder. (right side of each image) Each EUV image is 10 minutes apart.

The geomagnetic indices for this period are shown in Figure 5.2. There is a rise in the Kp index and therefore in the convection field strength. Dst shows that this is a steady but slightly disturbed period with a sudden commencement at 11:01 UT followed by a moderate storm. The period of interest for this event is the steady interval through the period just after the sudden commencement where the corotation lag is seen to persist.

Burch et al. (2004) derive corotation by tracking a long lived plasmaspheric notch and computing its departure from corotation. Figure 5.3 is reproduced from *Burch et al. (2004)* displaying the notch and its time evolution. The radial red line initially bisecting the notch then moves at the corotation velocity between each image denoting the position where the notch would be if it were corotating. The actual center of the notch is marked with the yellow arrow. From Figure 5.3 and the rest of the images available for the event, *Burch et al. (2004)* find that the notch is lagging corotation by 10% over the two days they are able to track it. Figure 5.4 shows this graphically where the red line is the corotation

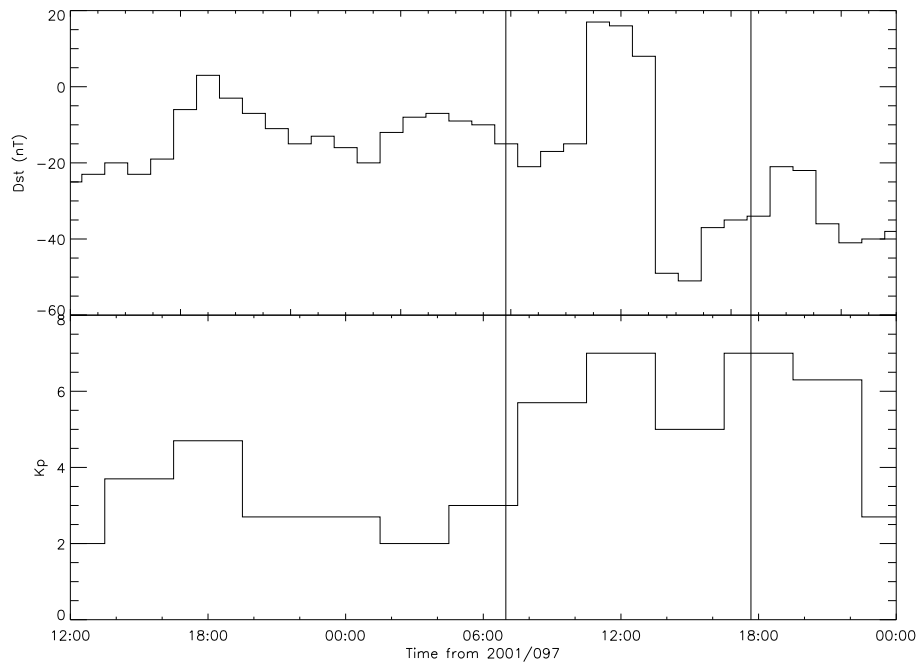


Figure 5.2: Dst and K_p indices for 7Apr2001 12:00UT (day 97) to 8Apr2001 24:00UT (day 98). The vertical lines at 8Apr2001 06:59UT and 8Apr2001 17:40UT denote the time covered in Figure 5.5.

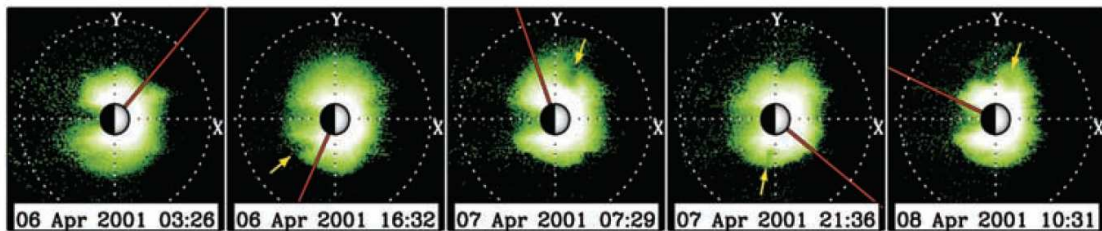


Figure 5.3: Selection of IMAGE-EUV images from 6-8Apr2001. The overplotted red beginning in the first image displays the position of the notch if it were corotating. In each subsequent image the yellow arrow marks the center of the notch. Figure from *Burch et al.* (2004).

predicted position, the black line is the EUV observed notch position. We will return to the green diamonds later in this chapter. The study was done using the raw EUV images which do not allow features within the plasmasphere to be distinguished due to look angle effects and the fact that the instrument is measuring line-of-sight quantities. The latter makes it impossible to determine which L -shell is providing the observed density which is not the case with the inverted images. Using the stackplots shown in Figure 5.5 we find that the corotation lag is present into $L = 3$ which is about $1 R_E$ inside the plasmopause. The corotation lag is seen in Figure 5.5 as features that are seen to have a slope greater than that of the overplotted corotation lines. The region from the plasmopause to $L = 3$ corresponds to magnetic latitudes between 30° to 50° . Each stackplot has the same format as in Chapter 3 except the data is repeated one image into the future on the right side of each plot, allowing features to be tracked across 00 MLT without having to wrap around the plot boundary. Studying the stackplots shows that the lag is present over a wide range of MLT values consistent with the ionospheric disturbance dynamo lag as opposed to any expected super-corotation in the dawn MLT sector and subcorotation in the dusk MLT sector based on the field geometry. In Figure 5.5 the corotation lag is observed as a slope steeper than the corotation guide lines. In both the evening and dawn MLT sectors the lag can be observed.

Ionospheric DMSP signature

In order to determine the ionospheric component of the corotation lag data from the DMSP F13 and F15 satellites is used. The ionospheric component of the corotation lag is the cross track ion drift measurement from the DMSP spacecraft. The sun-synchronous orbits of the DMSP satellites allow the same regions of the ionosphere to be observed on every orbit. F13 has a 05:45-17:45 LT orbit and F15 has a 09:28-21:28 LT orbit. In these

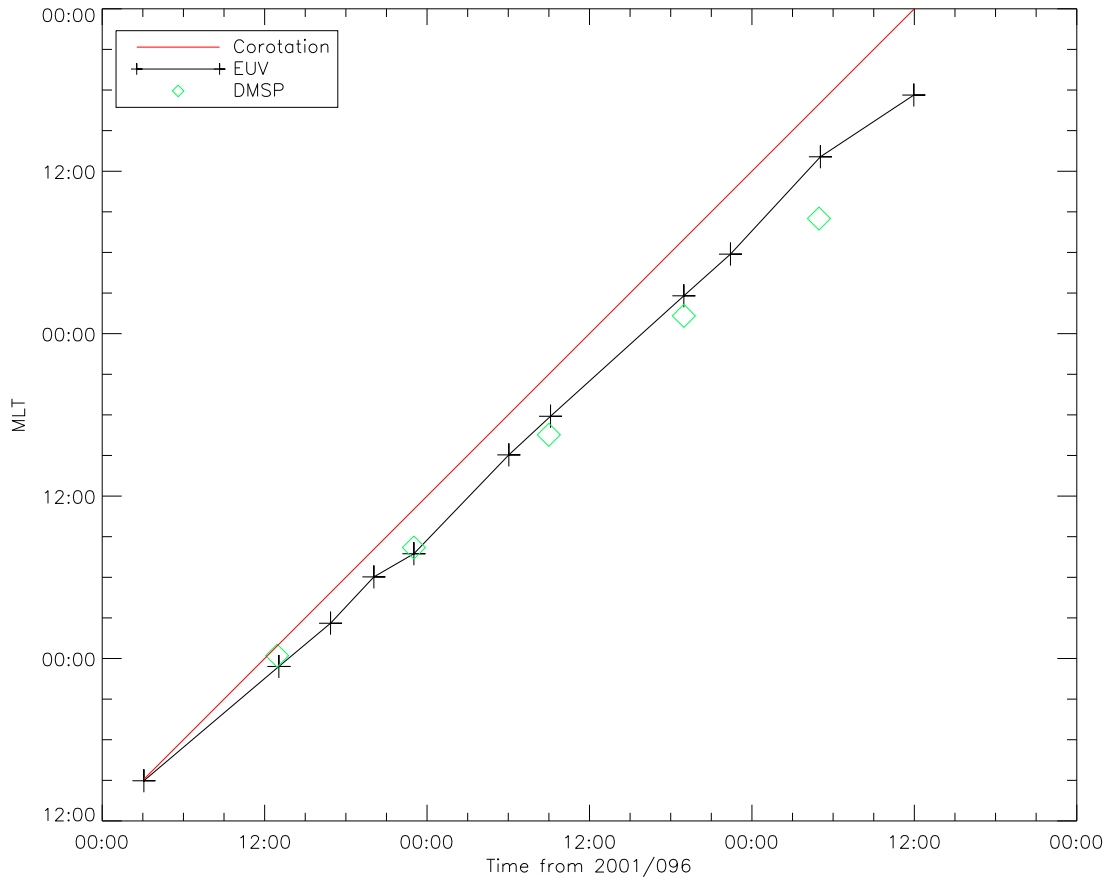


Figure 5.4: Position of the plasmaspheric notch in MLT as a function of UT during its observation 6Apr2001 03:05UT to 8Apr2001 12:03UT shown by the black line. The green diamonds represent the notch location as predicted by the DMSP measured eastward drift. The solid red line shows the position as predicted by perfect corotation. Figure adapted from *Burch et al. (2004)*.

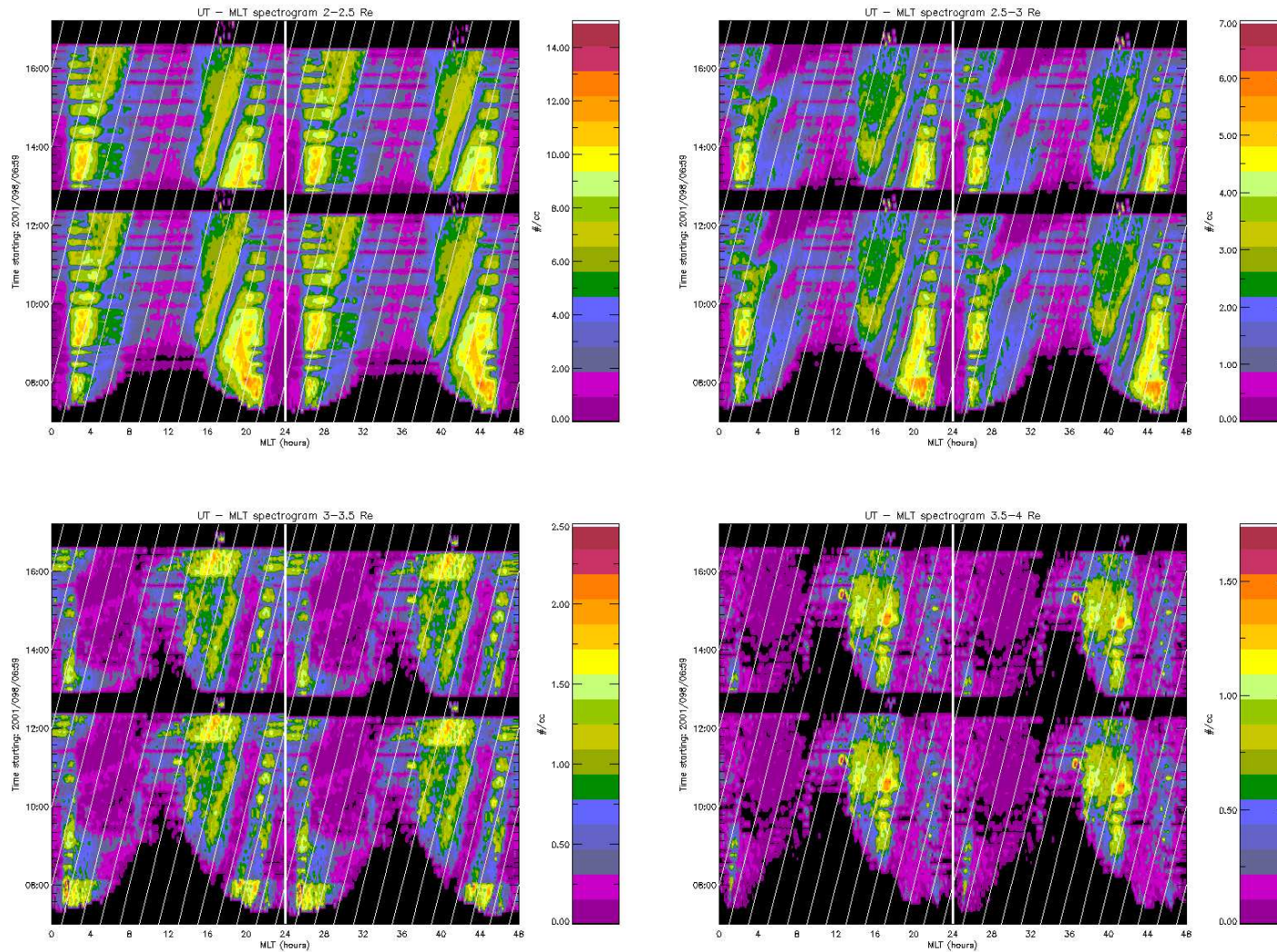


Figure 5.5: UT-MLT stackplots for 8Apr2001, shown are the 2 – 2.5, 2.5 – 3, 3 – 3.5, and 3.5 – 4 R_E annuli. MLT is seen to run from 00 to 48 as the stackplot is reproduced one image ahead to avoid having to wrap around the plot while following features.

data the ionospheric drift is measured for nearly all magnetic latitudes at the four local times traversed by the satellites. Shown in Figure 5.6 is the DMSP measured Eastward ion drift as it differs from corotation, as a function of magnetic latitude. The ion drift data are broken up into MLT quadrants centered at Noon (12 MLT), Midnight (00 MLT), Dawn (06 MLT), and Dusk (18 MLT) to match the local times of the DMSP satellites. In the auroral zone (magnetic latitude poleward of $\sim 60^\circ$) the drift is highly variable due to penetrating auroral fields and currents. Near the equator drifts follow a pattern of westward (subcorotation) in the dawn and noon MLT sectors and eastward (super-corotation) in the dusk and midnight sectors. This pattern is a result of ionospheric heating and intensification due to photoionization. The dusk sector follows more closely resembles the midnight sector because the ionosphere reaches a steady state temperature and density after enough time in the sun. This pattern shows that over the range of interest, from 30° to 50° magnetic latitude, there are great differences between each of the sectors. In the Noon sector, nearly all drifts are westward while at midnight there is a transition in drift direction as one moves poleward. The dawn drifts are also westward over the region of interest while the dusk drifts are nearer zero and westward over the region.

Using the data from Figure 5.6 it is straightforward to calculate the mean westward drift of the ionosphere in different magnetic latitude regions as a function of time over the 8Apr2001 event time period. The results of the calculation are shown in Figure 5.7 as well as in the green diamonds in Figure 5.4. Shown in Figure 5.7 is the mean eastward drift as a function of UT for different magnetic latitude regions, $30^\circ - 35^\circ$, $35^\circ - 40^\circ$, $40^\circ - 45^\circ$, and $45^\circ - 50^\circ$. The points are the mean westward drift plotted with 1σ error bars, while the solid line is a moving average of the drift. There exists a clear westward drift at all magnetic latitude regions over the whole 8Apr2001 period. This is a surprising result as there are major changes in the geomagnetic activity beginning at 11:00 UT on 8Apr2001 as a sudden commencement occurs followed by a moderate storm which would serve to input

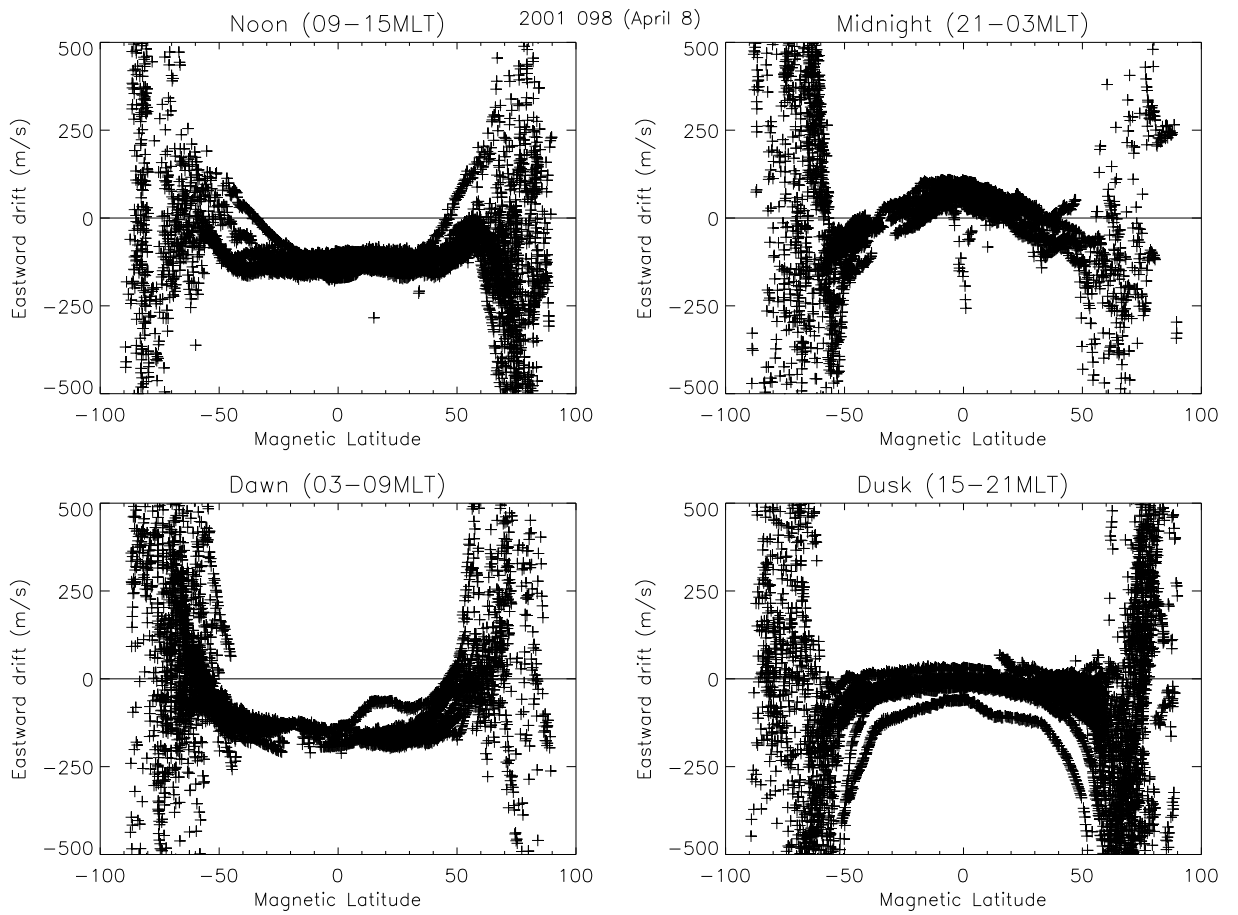


Figure 5.6: DMSP measured eastward drift as a function of magnetic latitude for 8Apr2001 in four MLT sectors centered at 12, 00, 06, 18 MLT.

additional energy into the ionosphere. Yet there is no signature of these occurrences in the ionosphere.

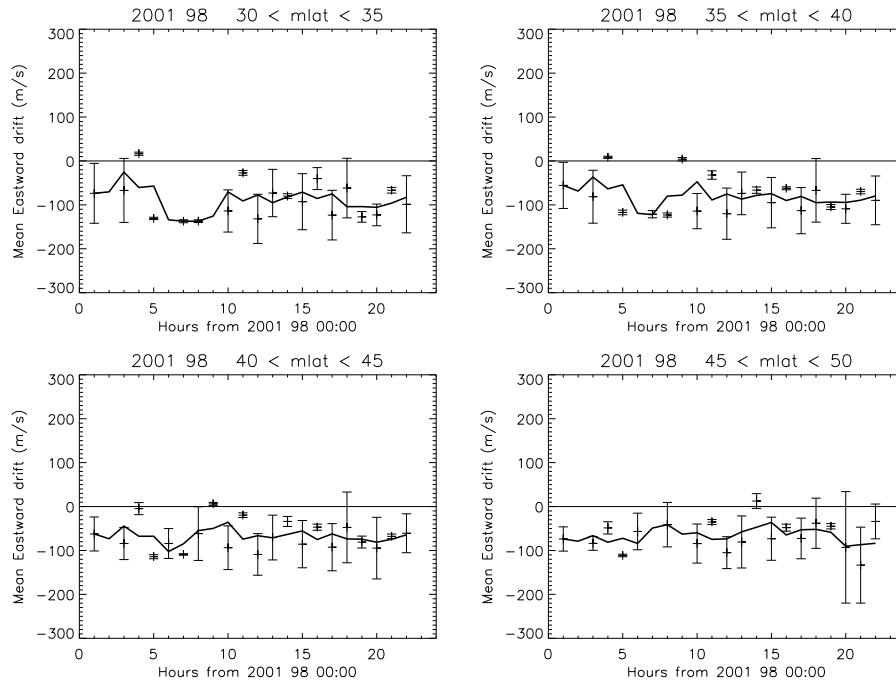


Figure 5.7: DMSP measured average Eastward drift for 8Apr2001 as a function of UT for different magnetic latitude ranges, $30^{\circ} - 35^{\circ}$, $35^{\circ} - 40^{\circ}$, $40^{\circ} - 45^{\circ}$, $45^{\circ} - 50^{\circ}$. The dark line overplotted is a moving average meant to bring out trends in the data.

Event Conclusions

Assuming that the ionosphere and plasmasphere rigidly rotate together, the signature of the ionospheric drift is clear that there is an ionospheric subcorotation occurring. The disturbance dynamo theory used by *Burch et al. (2004)* is supported by the uniformity of the drift across all MLT regions. There is however one troubling signature missing, that of the geomagnetic storm, while the ionospheric response to geomagnetic storm is debated (*Baron*

and Wand, 1983; Yeh *et al.*, 1994; Foster and Rich, 1997, and many others), a signature is expected. One expected signature is changes in the drift velocities as auroral fields and currents move equatorward causing the drift velocities to be anything but uniform.

Corotating Plasmaspheric Event (18Jun2001)

Here we focus on another event, 18Jun2001, which has a very different plasmaspheric response. We might expect the DMSP response to also be different. Figure 5.8 shows a series of EUV images starting at 18Jun2001 13:49:54UT. In this event the plasmasphere began to erode in response to a sudden commencement and increase in the convection electric field forming a large plasmaspheric drainage plume (upper right of each image). A subsequent decrease in the convection field strength then moves the Alfvén layer outside the plume. The plume plasma once again on closed drift paths begins corotating, which has the effect of wrapping the plume around the plasmasphere. Figure 5.9 shows the Kp and

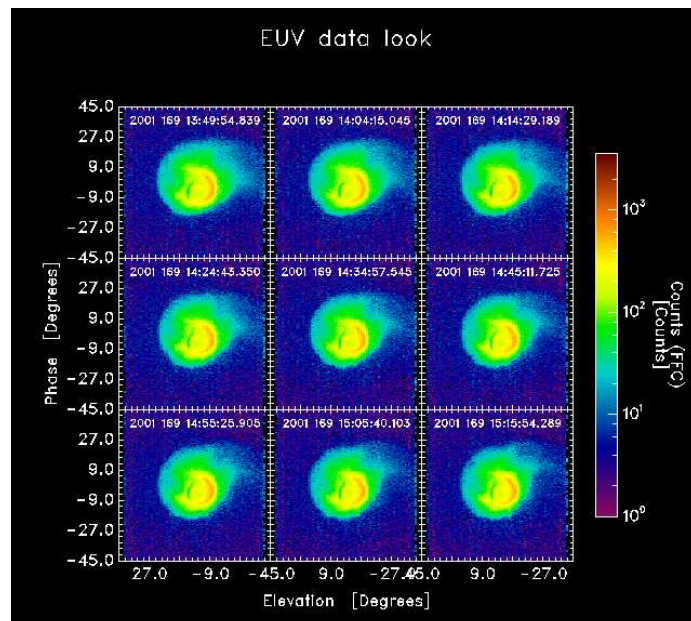


Figure 5.8: Selection of IMAGE-EUV images from 18Jun2001 demonstrating the wrapping of a large plasmaspheric plume.

Dst indices for the time period.

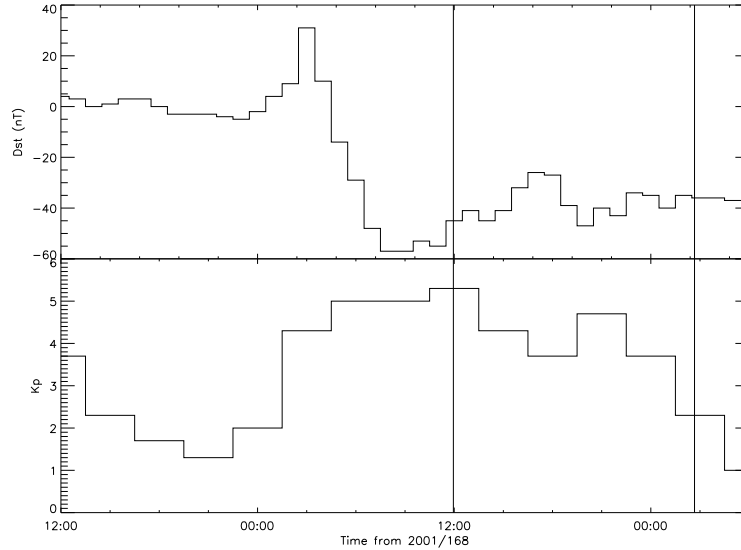


Figure 5.9: Dst and K_p indices for 17Jun2001 12:00UT (day 168) to 19Jun2001 06:00UT (day 170). The vertical lines at 18Jun2001 11:57UT and 19Jun2001 02:40UT denote the time covered in Figure 5.10.

The stackplots shown in Figure 5.10 demonstrate that this event is a corotation event. The corotation can be observed in the plasmaspheric images as well since the eroded plasmopause is steep allowing for easy tracking from image to image. Looking inside the plasmasphere there are many features that show the expected corotation signature. There is rigid corotation in the noon MLT sector, a lag pre-midnight, as expected from penetration of outer magnetospheric electric fields, and super-corotation in the dawn MLT sector, caused by the superposition of the convection and corotation electric fields. The features demonstrate this behavior throughout most of the plasmasphere all the way out to the plasmopause especially after 19Jun2001 00:00UT indicating that the Alfvén layer is outside the plasmopause. This signature implies that the ionospheric disturbance dynamo is not acting, thus providing an opportunity to study the DMSP signature for an event without an active dis-

turbance dynamo.

Ionospheric DMSP signature

Again using data from the DMSP F13 (0545-1745 LT) and F15 (0928-2128 LT) satellites the ionospheric drift can be found. Figure 5.11 displays the eastward drift as a function of magnetic latitude broken into the MLT bins centered at 12, 00, 06, and 18 MLT. The DMSP data quality is not as good for this event as for the 8Apr2001 event but the data should be sufficient. Surprisingly the drift signatures are extremely similar between Figures 5.6 and 5.11 implying that there may be a problem with the interpretation of the 8Apr2001 event.

Shown in Figure 5.12 is the average eastward drift as a function of time for 18Jun2001. The magnetic latitude bins are the same as in Figure 5.7, $30^{\circ} - 35^{\circ}$, $35^{\circ} - 40^{\circ}$, $40^{\circ} - 45^{\circ}$, and $45^{\circ} - 50^{\circ}$. While the lower quality DMSP data has increased the size of the error bars the trend is still clear that there is an westward drift for all times in each magnetic latitude bin.

Event Conclusions

The DMSP signature for 18Jun2001 shows the ionosphere lagging corotation for an event where the plasmasphere is clearly corotating. One possible interpretation is that there is a slip between the ionosphere and the plasmasphere, implying a disconnect between the low altitude ionospheric plasma motions and the high altitude plasmaspheric plasma. Another possible interpretation is that there is unfortunate coverage of the ionosphere with the four DMSP sampled local time sectors, implying that there are significant variations in the ion drift motion between the DSMP sampled local times, as indeed is often the case (*Heelis*, private communication). This result demonstrates the difficulties with associating

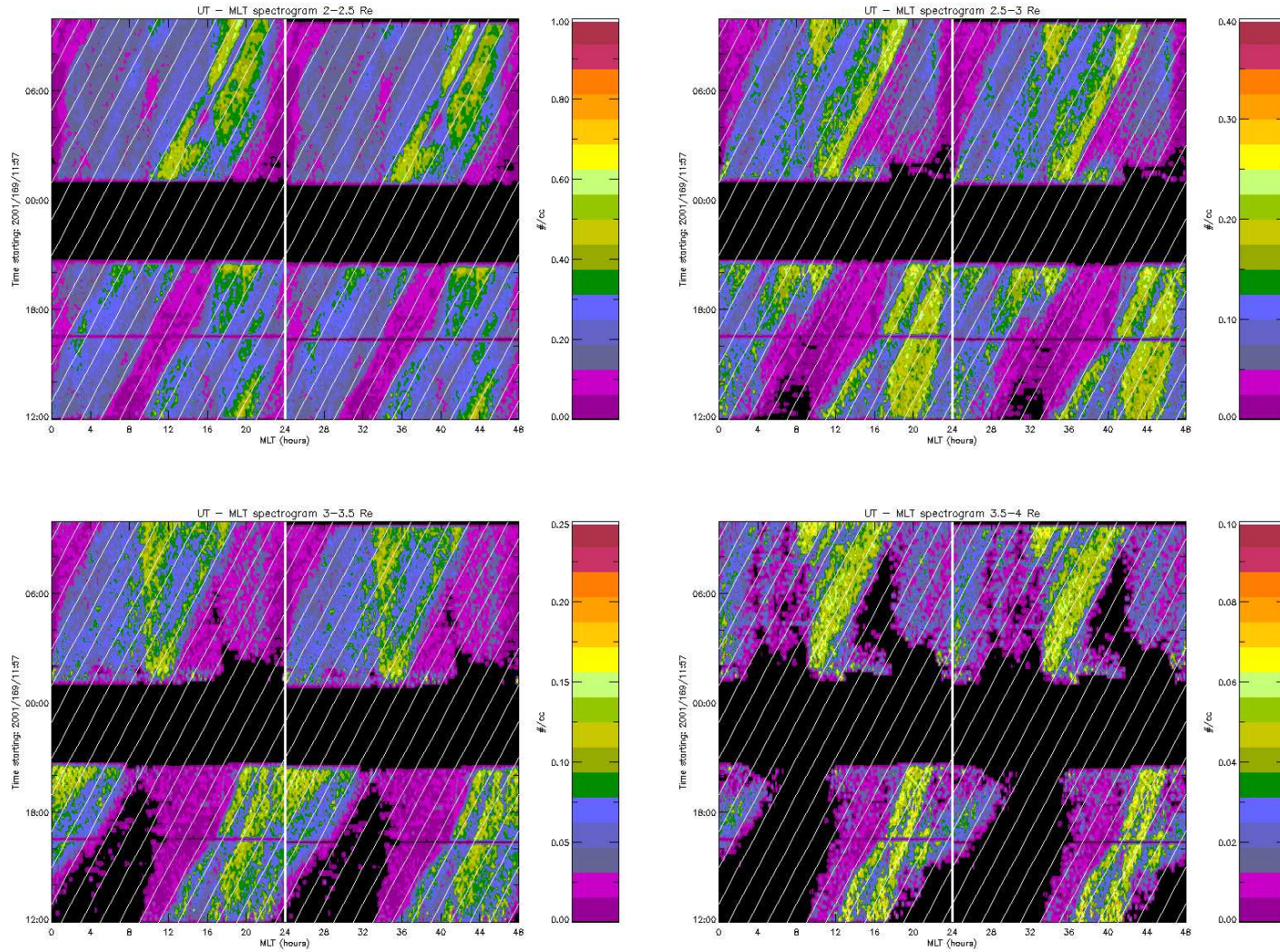


Figure 5.10: UT-MLT stackplots for 18Jun2001, shown are the 2 – 2.5, 2.5 – 3, 3 – 3.5, and 3.5 – 4 R_E annuli.

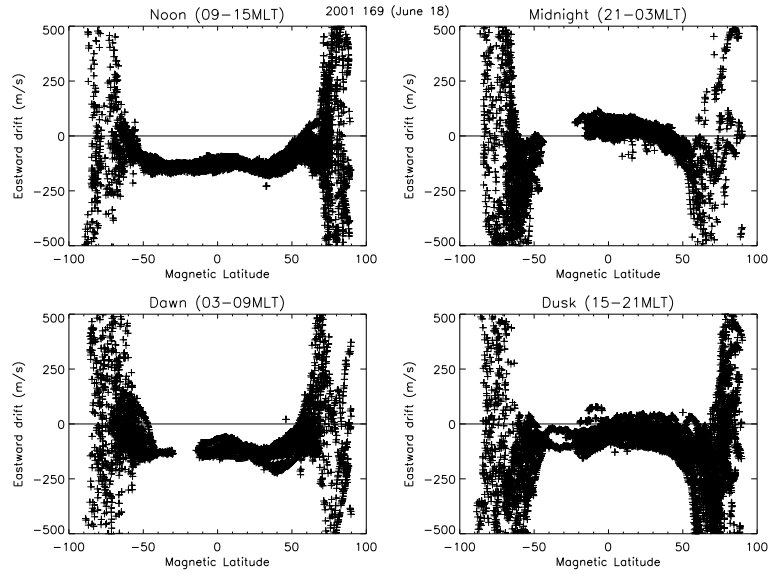


Figure 5.11: DMSP measured eastward drift as a function of magnetic latitude for 18Jun2001 in four MLT sectors centered at 12, 00, 06, 18 MLT.

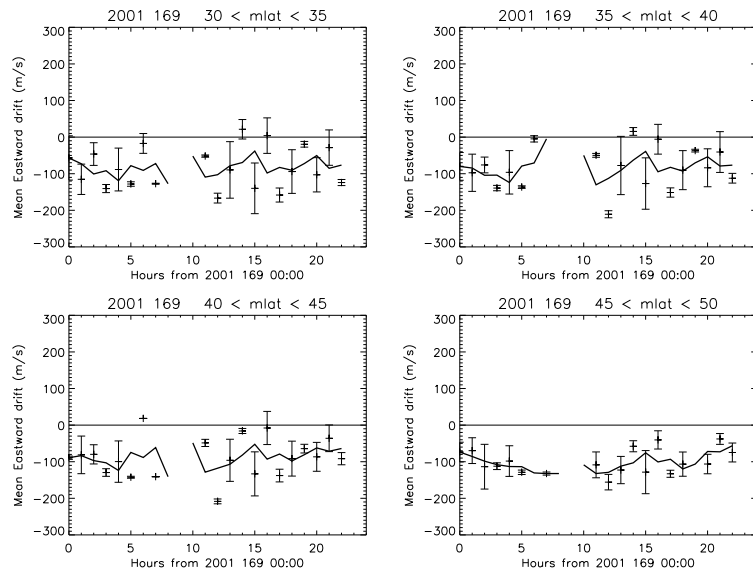


Figure 5.12: DMSP measured average Eastward drift for 18Jun2001 as a function of UT for different magnetic latitude ranges, $30^\circ - 35^\circ$, $35^\circ - 40^\circ$, $40^\circ - 45^\circ$, $45^\circ - 50^\circ$.

local *in-situ* data with global images. The highly localized measurements gather very detailed data along the track of the spacecraft but extrapolation to the global response is often quite difficult.

Discussion

As the ionospheric drift signature is remarkable similar for the corotating and lagging plasmasphere events. We believe that the issue is primarily a function of the equal weighting of the DMSP drift measurements and the implied interpolation between them. Using the DMSP drift measurements from 0545, 0928, 1745, and 2128 MLT places a measurement in each of the dawn, dusk, noon, and midnight MLT bins, but the measurements are certainly not in the center of these bins and are not evenly spaced around the the Earth. The grouping of measurements serves to bias the measurements to the dawn-post-dawn (0545-0928 MLT) region and the dusk-post-dusk (1745-2128 MLT) region. This neglect of the large regions between 2128-0545 MLT and 0928-1745 MLT may well hold the the missing dynamics.

There are certainly connections between ionospheric dynamics and plasmaspheric dynamics, however those relations will have to go undiscovered through the current work. While beyond the scope of this dissertation, other studies that could possibly lead to relation between ionospheric drift and plasmaspheric corotation could take the form of a statistical study of long term plasmaspheric corotation and/or corotation lag and long term ionospheric drift signatures. Another possible study would be detailed studies tracking features in the plasmasphere and the associated underlying ionospheric drift over a much finer time resolution. The problem with this study is the fundamental differences in resolution between the ionospheric measurements and the EUV images that only allow feature tracking at the plasmopause or the inverted EUV images allowing internal feature tracking at the

cost of more resolution.

CHAPTER 6

SUMMARY OF RESULTS

This dissertation presents three studies that represent a different data product that global imaging enables. The first two studies produce quantitative testable results demonstrating that analysis from global imaging can provide quantitative testable results. Global imaging allows the scientist to make extrapolations and comparisons that are not possible with local data alone. This enables comparison to other data sets on a continuous basis in methods not previous explored.

The observation of the previously unobserved theoretical boundary between the open and closed particle drift paths enables the extrapolation from the inner magnetosphere to the outer magnetosphere. In addition through the tracking of plasmaspheric features noting their rotation speed enables the comparison to the underlying ionosphere without the need to average data or use a statistical description of the dynamics.

Plasmapause Statistics

Chapter 2 presents a correlative statistical study of the plasmapause radial extent versus multiple solar wind and interplanetary magnetic field (IMF) parameters. The results of the study showed the plasmapause position depends on the IMF B_z component and a merging proxy, ϕ . The merging proxy is defined as $\phi = vB \sin^2(\theta/2)$, where v is the solar wind proton velocity, B is the IMF magnitude, and θ is the IMF clock angle. The derived relation between the plasmapause position, L_{pp} , and these parameter is given by

$$L_{pp} = 0.0374B_{z,155} - 1.05 \times 10^{-4}\phi_{275} + 4.38 \quad (6.1)$$

where $B_{z,155}$ is the IMF B_z component delayed 155 minutes from its arrival at Earth and ϕ_{275} is the merging proxy delayed 275 minutes from its arrival at Earth. The study finds that there are two distinctly different time scales involved in the evolution of the plasmasphere, one related to the coupling of the solar wind to the magnetosphere and the other with reconnection at the magnetopause.

This is an example of a study made easier through global imaging, an *in-situ* study of the same magnitude would be a massive undertaking. Global imaging allowed for the calculation of the plasmopause at a large range of MLT values simultaneously. This allows 1365 global images to provide the *in-situ* equivalent of 210762 satellite passes through the plasmopause determined by counting the total observed plasmopause positions. The plasmopause correlation studies of *O'Brien and Moldwin (2003)* provide the largest plasmopause catalog previously available of only 900 plasmopause crossings.

Convection Electric Field Derived From Global Imaging

Chapter 3 presents methods and examples of deriving the cross tail convection electric field from the measured motion of the Alfvén Layer within the plasmasphere. Tracking features within the plasmasphere from inverted EUV images allows global magnetospheric parameters to be derived from inner magnetospheric measurements.

Observational Verification of the Plasmaspheric Alfvén Layer

Chapter 3 presents the first observational verification of the boundary between open and closed drift paths in the inner magnetosphere, known as the plasmaspheric Alfvén layer. The study serves as an important observational verification of the convective plasmasphere model as postulated by *Nishida (1966)*.

EUV Derived Convection Electric Field Magnitude

Using the convective plasmasphere model, the position of the Alfvén layer can be used to derive the magnitude of the magnetospheric convection electric field. This result allows for imaging the inner magnetosphere to provide information about the outer magnetosphere. It is difficult to measure the convection electric field and it can not be measured globally making the EUV-derived values useful as an overall magnetospheric configuration parameter. The EUV feature tracking derivation of the convection electric field is validated through comparisons to current empirical models.

Plasmaspheric Signature in the Ionosphere

Not limited to external cause and effect studies of the plasmasphere, this dissertation looks inward at the underlying ionosphere. Chapter 5 presents the relationship between plasmaspheric corotation and subcorotation and the underlying ionospheric drift signature. By measuring the local ion drift velocity in the ionosphere the DMSP satellites provide a framework with which to identify periods where the plasmasphere may be corotating, super-corotating, or sub-corotating. It is our belief that the currently available ionospheric ion drift data is under sampling the global drift in such a way to give the consistent illusion that the plasmasphere should be sub-corotating, while images from the plasmasphere show clear corotation.

REFERENCES

- Akasofu, S.-I., A search for the interplanetary quantity controlling the development of geomagnetic storms, *Q. J. Roy. Astro. Soc.*, *20*, 119–137, 1979.
- Axford, W. I., and C. O. Hines, A unifying theory of high-latitude geophysical phenomena and geomagnetic storms, *Can. J. Phys.*, *39*, 1433–+, 1961.
- Baron, M. J., and R. H. Wand, F region ion temperature enhancements resulting from Joule heating, *J. Geophys. Res.*, *88*, 4114–4118, 1983.
- Blanc, M., and A. D. Richmond, The ionospheric disturbance dynamo, *J. Geophys. Res.*, *85*, 1669–1686, 1980.
- Borg, A. L., M. Øieroset, T. D. Phan, F. S. Mozer, A. Pedersen, C. Mouikis, J. P. McFadden, C. Twitty, A. Balogh, and H. Rème, Cluster encounter of a magnetic reconnection diffusion region in the near-Earth magnetotail on September 19, 2003, *Geophys. Res. Lett.*, *32*, 19,105–+, doi:10.1029/2005GL023794, 2005.
- Brandt, P. C. ., D. G. Mitchell, Y. Ebihara, B. R. Sandel, E. C. Roelof, J. L. Burch, and R. Demajistre, Global IMAGE/HENA observations of the ring current: Examples of rapid response to IMF and ring current-plasmasphere interaction, *J. Geophys. Res.*, *107*(A11), 12–1, doi:10.1029/2001JA000084, 2002.
- Buonsanto, M. J., Ionospheric Storms - A Review, *Space Sci. Rev.*, *88*, 563–601, doi: 10.1023/A:1005107532631, 1999.
- Burch, J. L., IMAGE mission overview, *Space Sci. Rev.*, *91*, 1–14, 2000.
- Burch, J. L., D. G. Mitchell, B. R. Sandel, P. C. Brandt, and M. Wüest, Global dynamics of the plasmasphere and ring current during magnetic storms, *Geophys. Res. Lett.*, *28*, 1159–1162, 2001.
- Burch, J. L., J. Goldstein, and B. R. Sandel, Cause of plasmasphere corotation lag, *Geophys. Res. Lett.*, *31*, 5802, 2004.
- Burke, W. J., D. R. Weimer, and N. C. Maynard, Geoeffective interplanetary scale sizes derived from regression analysis of polar cap potentials, *J. Geophys. Res.*, *104*(.13), 9989–9994, 1999.
- Carpenter, D. L., Whistler Measurements of Electron Density and Magnetic Field Strength in the Remote Magnetosphere, *J. Geophys. Res.*, *68*(.17), 3727–+, 1963.
- Carpenter, D. L., Whistler Studies of the Plasmapause in the Magnetosphere, 1, Temporal Variations in the Position of the Knee and Some Evidence on Plasma Motions near the Knee, *J. Geophys. Res.*, *71*(.10), 693–+, 1966.

- Carpenter, D. L., Whistler evidence of the dynamic behavior of the duskside bulge in the plasmasphere, *J. Geophys. Res.*, *75*, 3837–3847, 1970.
- Carpenter, D. L., and R. R. Anderson, An ISEE/Whistler model of equatorial electron density in the magnetosphere, *J. Geophys. Res.*, *97*(.16), 1097–1108, 1992.
- Carpenter, D. L., and J. Lemaire, Erosion and Recovery of the Plasmasphere in the Plasma-pause Region, *Space Sci. Rev.*, *80*, 153–179, 1997.
- Carpenter, D. L., B. L. Giles, C. R. Chappell, P. M. E. Decreau, R. R. Anderson, A. M. Persoon, A. J. Smith, Y. Corcuff, and P. Canu, Plasmasphere dynamics in the duskside bulge region: A new look at old topic, *J. Geophys. Res.*, *98*(.17), 19,243–+, 1993.
- Chappell, C. R., K. K. Harris, and G. W. Sharp, The Reaction of the Plasmopause to Varying Magnetic Activity, in *ASSL Vol. 17: Particles and Field in the Magnetosphere*, pp. 148–+, 1970a.
- Chappell, R., K. K. Harris, and G. W. Sharp, A study of the influence of magnetic activity on the location of the plasmopause as measured by ogo 5, *J. Geophys. Res.*, *75*, 50–+, 1970b.
- Cornelius, J. R., and A. J. Mazzella, Jr., The topside ionospheric plasma monitor (SSIES, SSIES-2 and SSIES-3) on the spacecraft of the Defense Meteorological Satellite Program (DMSP), user's guide. Volume 2: Programmer's guide for software at AFSFC, *Tech. rep.*, 1994.
- Darrouzet, F., J. De Keyser, P. M. E. Décreau, J. F. Lemaire, and M. W. Dunlop, Spatial gradients in the plasmasphere from Cluster, *Geophys. Res. Lett.*, *33*, 8105–+, doi:10.1029/2006GL025727, 2006.
- De Zeeuw, D. L., S. Sazykin, R. A. Wolf, T. I. Gombosi, A. J. Ridley, and G. Tóth, Coupling of a global MHD code and an inner magnetospheric model: Initial results, *J. Geophys. Res.*, *109*(A18), A12,219, doi:10.1029/2003JA010366, 2004.
- Doe, R. A., M. B. Moldwin, and M. Mendillo, Plasmopause morphology determined from an empirical ionospheric convection model, *J. Geophys. Res.*, *97*, 1151–1156, 1992.
- Dungey, L. W., *The structure of the exosphere or adventures in velocity space*, Gordon and Breach, New York, 1963.
- Foster, J. C., and W. J. Burke, Saps: A new characterization for sub-auroral electric fields, *EOS*, *83*, 393–394, 2002.
- Foster, J. C., and F. J. Rich, Prompt midlatitude electric field effects during severe geomagnetic storms, *J. Geophys. Res.*, *103*, 26,367–26,372, doi:10.1029/97JA03057, 1997.

- Gallagher, D. L., and M. L. Adrian, Two-dimensional drift velocities from the image euv plasmaspheric imager, *J. Atmos. Sol. Terr. Phys.*, 69(3), 341–350, doi:10.1016/j.jastp.2006.05.028, 2007.
- Garrido, D. E., R. W. Smith, D. W. Swift, S. Akasofu, B. M. Robinson, and Y. T. Chiu, Imaging the plasmasphere and trough regions in the extreme ultraviolet, in *Proc. SPIE Vol. 1744, p. 117-136, Instrumentation for Magnetospheric Imagery, Supriya Chakrabarti; Ed.*, pp. 117–136, 1992.
- Goel, M. K., B. C. N. Rao, S. Chandra, and E. J. Maier, Satellite measurements of ion composition and temperatures in the topside ionosphere during medium solar activity, *J. Atmos. Terr. Phys.*, 38, 389–394, 1976.
- Goldstein, J., R. W. Spiro, P. H. Reiff, R. A. Wolf, B. R. Sandel, J. W. Freeman, and R. L. Lambour, IMF-driven overshielding electric field and the origin of the plasmaspheric shoulder of May 24, 2000, *Geophys. Res. Lett.*, 29, 66–1, 2002a.
- Goldstein, J., R. A. Wolf, B. R. Sandel, W. T. Forrester, D. L. Gallagher, P. H. Reiff, and R. Spiro, Rapid response of the plasmasphere to changes in the solar wind and IMF: Global plasmopause electric field measurements by IMAGE EUV, and simulation with the Rice MSM., *AGU Spring Meeting Abstracts*, pp. B9+, 2002b.
- Goldstein, J., B. R. Sandel, W. T. Forrester, and P. H. Reiff, IMF-driven plasmasphere erosion of 10 July 2000, *Geophys. Res. Lett.*, 30, 46–1, 2003.
- Goldstein, J., B. R. Sandel, M. R. Hairston, and P. H. Reiff, Control of plasmaspheric dynamics by both convection and sub-auroral polarization stream, *Geophys. Res. Lett.*, 30, 6–1, 2003a.
- Goldstein, J., R. W. Spiro, B. R. Sandel, R. A. Wolf, S.-Y. Su, and P. H. Reiff, Overshielding event of 28-29 July 2000, *Geophys. Res. Lett.*, 30, 3–1, 2003b.
- Goldstein, J., B. R. Sandel, M. R. Hairston, and S. B. Mende, Plasmopause undulation of 17 April 2002, *Geophys. Res. Lett.*, 31, L15,801, 2004a.
- Goldstein, J., B. R. Sandel, M. F. Thomsen, M. Spasojević, and P. H. Reiff, Simultaneous remote sensing and in situ observations of plasmaspheric drainage plumes, *J. Geophys. Res.*, 109(A18), A3202, 2004b.
- Goldstein, J., R. A. Wolf, B. R. Sandel, and P. H. Reiff, Electric fields deduced from plasmopause motion in IMAGE EUV images, *Geophys. Res. Lett.*, 31, 1801–+, doi: 10.1029/2003GL018797, 2004c.
- Goldstein, J., B. R. Sandel, W. T. Forrester, M. F. Thomsen, and M. R. Hairston, Global plasmasphere evolution 22-23 April 2001, *J. Geophys. Res.*, 110(A9), A12,218, doi: 10.1029/2005JA011282, 2005.

- Grebowsky, J. M., Model study of plasmopause motion, *J. Geophys. Res.*, 75, 4329–4333, 1970.
- Gringauz, K. I., The structure of the ionized gas envelope of earth from direct measurements in the U.S.S.R. of local charged particle concentrations, *Planet. Space Sci.*, 11, 281–296, 1963.
- Gurgiolo, C., B. R. Sandel, J. D. Perez, D. G. Mitchell, C. J. Pollock, and B. A. Larsen, Overlap of the plasmasphere and ring current: Relation to subauroral ionospheric heating, *J. Geophys. Res.*, p. A12217, 2005.
- Harris, K. K., G. W. Sharp, and C. R. Chappell, Observations of the plasmopause from OGO-5, *J. Geophys. Res.*, 75, 219–+, 1970.
- Heelis, R. A., *private communication*, private communication.
- Heynderickx, D., J. Lemaire, and E. J. Daly, Historical review of the different procedures used to compute the l-parameter, *Radiation Measurements*, 26(3), 325–331, 1996.
- Horwitz, J. L., and N. Singh, Special section: Plasmasphere refilling, *J. Geophys. Res.*, 97, 1047–1048, 1992.
- Jackson, J. D., *Classical Electrodynamics, 3rd Edition*, Classical Electrodynamics, 3rd Edition, by John David Jackson, pp. 832. ISBN 0-471-30932-X. Wiley-VCH, July 1998., 1998.
- Jaggi, R. K., and R. A. Wolk, Self-consistent calculation of the motion of a sheet of ions in the magnetosphere, *J. Geophys. Res.*, 78, 2852–2866, 1973.
- Kan, J. R., and L. C. Lee, Energy coupling function and solar wind-magnetosphere dynamo, *Geophys. Res. Lett.*, 6, 577–580, 1979.
- Kavanagh, L. D., J. W. Freeman, and A. J. Chen, Plasma Flow in the Magnetosphere, *J. Geophys. Res.*, 73(12), 5511, 1968.
- Kelley, M. C., B. G. Fejer, and C. A. Gonzales, An explanation for anomalous equatorial ionospheric electric fields associated with a northward turning of the interplanetary magnetic field, *Geophys. Res. Lett.*, 6, 301–304, 1979.
- Kivelson, M. G., and C. T. Russell, *Introduction to Space Physics*, Introduction to Space Physics, Edited by Margaret G. Kivelson and Christopher T. Russell, pp. 586. ISBN 0521451043. Cambridge, UK: Cambridge University Press, April 1995., 1995.
- Larsen, B. A., D. M. Klumpar, and C. Gurgiolo, Correlation between plasmopause position and solar wind parameters, *J. Atmos. Sol. Terr. Phys.*, 69(3), 334–340, doi:10.1016/j.jastp.2006.06.017, 2007.

- Lyons, L. R., and D. J. Williams, *Quantitative aspects of magnetospheric physics*, vol. 3, Dordrecht, D. Reidel Publishing Co., 1984.
- Maynard, N. C., and A. J. Chen, Isolated cold plasma regions: Observations and their relation to possible production mechanisms, *J. Geophys. Res.*, *80*, 1009–1013, 1975.
- Mayr, H. G., J. M. Grebowsky, and H. A. Taylor, Jr., Study of the thermal plasma on closed field lines outside the plasmasphere, *Planet. Space Sci.*, *18*, 1123–+, 1970.
- McIlwain, C. E., Coordinates for Mapping the Distribution of Magnetically Trapped Particles, *J. Geophys. Res.*, *66*, 3681–+, 1961.
- Mitchell, D. G., S. E. Jaskulek, C. E. Schlemm, E. P. Keath, R. E. Thompson, B. E. Tossman, J. D. Boldt, J. R. Hayes, G. B. Andrews, N. Paschalidis, D. C. Hamilton, R. A. Lundgren, E. O. Tums, P. Wilson, H. D. Voss, D. Prentice, K. C. Hsieh, C. C. Curtis, and F. R. Powell, High energy neutral atom (hena) imager for the IMAGE mission, *Space Sci. Rev.*, *91*, 67–112, 2000.
- Moldwin, M. B., L. Downward, H. K. Rassoul, R. Amin, and R. R. Anderson, A new model of the location of the plasmopause: Crres results, *J. Geophys. Res.*, pp. 2–1, 2002.
- Neter, J., M. H. Kutner, C. J. Nachtsheim, and W. Wasserman, *Applied Linear Statistical Models*, fourth ed., Irwin, Chicago, 1996.
- Newberry, I. T., R. H. Comfort, P. G. Richards, and C. R. Chappell, Thermal He(+) in the plasmasphere - Comparison of observations with numerical calculations, *J. Geophys. Res.*, *94*, 15,265–15,276, 1989.
- Nishida, A., Formation of Plasmopause, or Magnetospheric Plasma Knee, by the Combined Action of Magnetospheric Convection and Plasma Escape from the Tail, *J. Geophys. Res.*, *71*, 5669–+, 1966.
- Northrup, T. G., *The Adiabatic Motion of Charged Particles*, John Wiley and Sons, Inc, 1963.
- O'Brien, T. P., and M. B. Moldwin, Empirical plasmopause models from magnetic indices, *Geophys. Res. Lett.*, *30*, 1–1, 2003.
- Parks, G. K., *Physics of space plasmas : an introduction*, Physics of space plasmas : an introduction / George K Parks. Boulder, Colo. : Westview Press, Advanced Book Program, c2004., 2004.
- Peymirat, C., A. D. Richmond, and A. T. Koba, Electrodynamic coupling of high and low latitudes: Simulations of shielding/overshielding effects, *J. Geophys. Res.*, *105*, 22,991–23,004, doi:10.1029/2000JA000057, 2000.

- Press, W. H., B. P. Flannery, S. A. Teukolsky, and W. T. Vetterling, *Numerical Recipes: The Art of Scientific Computing*, 2nd ed., Cambridge University Press, Cambridge (UK) and New York, 1992.
- Rasinkangas, R., K. Mursula, T. Ulich, and J. Kangas, The online space physics textbook of the university of oulu, World Wide Web, <http://www oulu.fi/ spaceweb/textbook/>, 1998.
- Rasmussen, C. E., S. M. Guiter, and S. G. Thomas, A two-dimensional model of the plasmasphere - Refilling time constants, *Planet. Space Sci.*, *41*, 35–43, 1993.
- Reiff, P. H., R. W. Spiro, and T. W. Hill, Dependence of polar cap potential drop on interplanetary parameters, *J. Geophys. Res.*, *86*(.15), 7639–7648, 1981.
- Sandel, B. R., A. L. Broadfoot, C. C. Curtis, R. A. King, T. C. Stone, R. H. Hill, J. Chen, O. H. W. Siegmund, R. Raffanti, D. D. Allred, R. S. Turley, and D. L. Gallagher, The extreme ultraviolet imager investigation for the IMAGE mission, *Space Sci. Rev.*, *91*, 197–242, 2000.
- Sandel, B. R., J. Goldstein, D. L. Gallagher, and M. Spasojevic, Extreme Ultraviolet Imager Observations of the Structure and Dynamics of the Plasmasphere, *Space Sci. Rev.*, *109*, 25–46, 2003.
- Schild, M. A., J. W. Freeman, and A. J. Dessler, A Source for Field-Aligned Currents at Auroral Latitudes, *J. Geophys. Res.*, *74*, 247–+, 1969.
- Selesnick, R. S., and J. D. Richardson, Plasmasphere formation in arbitrarily oriented magnetospheres, *Geophys. Res. Lett.*, *13*, 624–627, 1986.
- Shepherd, S. G., Polar cap potential saturation: Observations, theory, and modeling, *J. Atmos. Sol. Terr. Phys.*, *69*(3), 234–248, doi:10.1016/j.jastp.2006.07.022, 2007.
- Song, X., R. Gendrin, and G. Caudal, Refilling process in the plasmasphere and its relation to magnetic activity, *J. Atmos. Terr. Phys.*, *50*, 185–195, 1988.
- Sonnerup, B. U. O., Magnetopause reconnection rate, *J. Geophys. Res.*, *79*, 1546, 1974.
- Stern, D. P., The motion of a proton in the equatorial magnetosphere, *J. Geophys. Res.*, *80*, 595–599, 1975.
- Stern, D. P., One-dimensional models of quasi-neutral parallel electric fields, *J. Geophys. Res.*, *86*(.15), 5839–5860, 1981.
- Stone, E. C., A. M. Frandsen, R. A. Mewaldt, E. R. Christian, D. Margolies, J. F. Ormes, and F. Snow, The Advanced Composition Explorer, *Space Sci. Rev.*, *86*, 1–22, 1998.
- Summers, D., R. M. Thorne, and F. Xiao, Relativistic theory of wave-particle resonant diffusion with application to electron acceleration in the magnetosphere, *J. Geophys. Res.*, *103*, 20,487–20,500, doi:10.1029/98JA01740, 1998.

- Toffoletto, F., S. Sazykin, R. Spiro, and R. Wolf, Inner magnetospheric modeling with the Rice Convection Model, *Space Sci. Rev.*, *107*, 175–196, 2003.
- van Allen, J. A., C. E. McIlwain, and G. H. Ludwig, Radiation Observations with Satellite 1958E, *J. Geophys. Res.*, *64*(.13), 271–+, 1959.
- Vasyliunas, V. M., Mathematical models of the magnetosphere convection and its coupling to the ionosphere, in *Particles and fields in the magnetosphere*, edited by B. M. McCormac, pp. 60–71, Hingham, MA, 1970.
- Volland, H., A model of the magnetospheric electric convection field, *J. Geophys. Res.*, *83*(.12), 2695–2699, 1978.
- Waite, J. H., J. L. Horwitz, and R. H. Comfort, Diffusive equilibrium distributions of He⁺ in the plasmasphere, *Planet. Space Sci.*, *32*, 611–618, doi:10.1016/0032-0633(84)90111-9, 1984.
- Weimer, D. R., Models of high-latitude electric potentials derived with a least error fit of spherical harmonic coefficients, *J. Geophys. Res.*, *100*, 19,595–19,608, doi:10.1029/95JA01755, 1995.
- Weimer, D. R., An improved model of ionospheric electric potentials including substorm perturbations and application to the Geospace Environment Modeling November 24, 1996, event, *J. Geophys. Res.*, *106*, 407–416, doi:10.1029/2000JA000604, 2001.
- Weimer, D. R., and D. A. Gurnett, Large-amplitude auroral electric fields measured with DE 1, *J. Geophys. Res.*, *98*, 13,557–+, 1993.
- Wolf, R. A., Calculations of magnetospheric electric fields, in *Magnetospheric Physics*, edited by B. M. McCormac, pp. 167–177, Dordrecht, Netherlands, 1974.
- Yeh, K. C., S. Y. Ma, K. H. Lin, and R. O. Conkright, Global ionospheric effects of the October 1989 geomagnetic storm, *J. Geophys. Res.*, *99*, 6201–6218, 1994.

APPENDICES

APPENDIX A

MAGNETOSPHERIC COORDINATES

This useful appendix shows *properties* of the dipole coordinate system, all these parameters are derivable, shown here in the symbolism of *Rasmussen et al.* (1993).

The symbols used are:

r, θ, ϕ	radius, colatitude, azimuthal angle
ϕ, q, s	dipole coordinates (right-handed)
h_ϕ, h_q, h_s	coordinate scale factors
B	magnetic field
χ	angle of magnetic field from horizontal
V	flux tube volume per unit magnetic flux
R_E	Earth radius = 6371.21 km
L	McIlwain parameter (<i>McIlwain</i> , 1961)
B_0, r_0	equatorial value of the magnetic field at a reference altitude
Λ	Invariant latitude

The magnetic field for a dipole is:

$$B = \frac{B_0}{(r/r_0)^3} \sqrt{1 + 3 \cos^2 \theta} \quad (\text{A.2})$$

The volume of a flux tube in a dipole field is:

$$V = \frac{32r_0L^4}{35B_0} \sqrt{1 - L^{-1}} \left(1 + \frac{1}{2}L^{-1} + \frac{3}{8}L^{-2} + \frac{5}{16}L^{-3} \right) \quad (\text{A.3})$$

The orthogonal coordinates are, ϕ ,

$$q = \left(\frac{R_E}{r} \right) \sin^2(\theta) \quad (\text{A.4})$$

and

$$s = \left(\frac{R_E}{r} \right)^2 \cos(\theta) \quad (\text{A.5})$$

where s is aligned with the magnetic field and q is perpendicular to the magnetic field.

The unit vectors are:

$$\hat{\mathbf{e}}_\phi = -\sin(\phi)\hat{\mathbf{e}}_\theta + \cos(\phi)\hat{\mathbf{e}}_\phi \quad (\text{A.6})$$

$$\hat{\mathbf{e}}_q = -\cos(\chi)\hat{\mathbf{e}}_r + \sin(\chi)\hat{\mathbf{e}}_\theta \quad (\text{A.7})$$

$$\hat{\mathbf{e}}_s = -\sin(\chi)\hat{\mathbf{e}}_r - \cos(\chi)\hat{\mathbf{e}}_\theta \quad (\text{A.8})$$

where

$$\hat{\mathbf{e}}_r = \sin(\theta) [\cos(\phi)\hat{\mathbf{e}}_x + \sin(\phi)\hat{\mathbf{e}}_y] + \cos(\theta)\hat{\mathbf{e}}_z \quad (\text{A.9})$$

$$\hat{\mathbf{e}}_\theta = \cos(\theta) [\cos(\phi)\hat{\mathbf{e}}_x + \sin(\phi)\hat{\mathbf{e}}_y] - \sin(\theta)\hat{\mathbf{e}}_z \quad (\text{A.10})$$

The scale factors are:

$$h_\phi = r \sin(\theta) \quad (\text{A.11})$$

$$h_q = rL \cos(\chi) = \frac{R_E}{\sin(\theta)\sqrt{1+3\cos^2\theta}} \left(\frac{r}{R_E} \right)^3 \quad (\text{A.12})$$

$$h_s = \frac{R_E B_0}{B} = \frac{R_E}{\sqrt{1+3\cos^2\theta}} \left(\frac{r}{R_E} \right)^3 \quad (\text{A.13})$$

An small element of arc length along a flux tube is

$$ds_a = h_s ds = \frac{-1}{\sin(\chi)} dr = -R_E L \sin(\theta) \sqrt{1+3\cos^2\theta} d\theta \quad (\text{A.14})$$

where

$$\begin{aligned} ds &= -\left(\frac{R_E}{r}\right)^2 \frac{\sqrt{1+3\cos^2\theta}}{\cos(\chi)} d\theta \\ &= -\left(\frac{R_E}{r}\right)^2 \frac{\sqrt{1+3\cos^2\theta}}{R_E \sin(\chi)} dr \end{aligned} \quad (\text{A.15})$$

$$d\theta = \frac{\tan(\theta)}{2r} dr \quad (\text{A.16})$$

Some useful transformations

$$L = \frac{r}{R_E \sin^2\theta} \quad (\text{A.17})$$

$$\cos(\chi) = \frac{\sin\theta}{\sqrt{1+3\cos^2\theta}} \quad (\text{A.18})$$

$$\sin(\chi) = \frac{2\cos\theta}{\sqrt{1+3\cos^2\theta}} \quad (\text{A.19})$$

$$\tan(\chi) = 2\cot(\theta) \quad (\text{A.20})$$

$$\sqrt{1+3\cos^2\theta} = s\sqrt{1+\frac{3}{4}\sin^2\theta} = 2\sqrt{1-\frac{3r}{4R_E L}} \quad (\text{A.21})$$

$$\frac{d\theta}{dt} = \frac{-\sin(\chi)\cos(\chi)}{L} \frac{dL}{dt} \quad (\text{A.22})$$

$$\frac{dr}{dt} = \frac{r\cos^2(\chi)}{L} \frac{dL}{dt} \quad (\text{A.23})$$

$$\frac{dL}{dt} = \frac{v_{eq}}{R_E} \quad (\text{A.24})$$

$$\Lambda = \arccos(1/L)^{\frac{1}{2}} \quad (\text{A.25})$$

where v_{eq} is the magnetospheric convection velocity in the equatorial plane.

Partial derivatives are given by

$$\frac{\partial}{\partial q} = -h_q \left(\cos(\chi) \frac{\partial}{\partial r} - \frac{\sin(\chi)}{r} \frac{\partial}{\partial \theta} \right) \quad (\text{A.26})$$

$$\frac{\partial}{\partial s} = -h_s \left(\sin(\chi) \frac{\partial}{\partial r} + \frac{\cos(\chi)}{r} \frac{\partial}{\partial \theta} \right) \quad (\text{A.27})$$